Design, Synthesis and Characterization of Polymeric Films and Membranes

by

Ikilem Gocek

A dissertation submitted to the Graduate Faculty of
Auburn University
in partial fulfillment of the
requirements for the Degree of
Doctor of Philosophy

Auburn, Alabama
August 9, 2010

Keywords: High temperature PEMFC, PBI, PP, membrane, synthesis, modeling

Approved by

Sabit Adanur, Chair, Professor of Polymer and Fiber Engineering
Peter Schwartz , Professor of Polymer and Fiber Engineering
Carol Warfield, Professor of Consumer Affairs

Abstract

Solid polymer electrolyte membranes play a vital role in polymer electrolyte membrane fuel cells. Although these membranes have been used successfully, there is still a need to improve their proton conductivity, lower their cost and increase their operation temperature.

Polybenzimidazole, a high temperature resistant polymer, was synthesized and polymer electrolyte membrane was fabricated with a novel method including ultrasonic generator and ultrasonic nozzle. A computer model was developed by using COMSOL Multiphysics program.

Polypropylene (PP) films were fabricated by using single screw extruder in order to find out how the machine parameters affect the mechanical properties of the product. Nanoclay reinforced PP films were produced by using single screw extruder after compatibilizer, nanoclay and PP were mixed in a twin screw extruder. Tensile, tear and burst strength tests were performed on these films.

With the increasing temperature and winding speed, the thickness of the films decreases; however, with the increasing screw motor speed film thickness increases. With the increasing temperature tear strength becomes higher in machine direction (MD); however tear strength decreases in cross direction (CD). With the increasing screw motor speed tear strength of the films did not show any specific trend in MD; however, tear strength of the films in CD increases. With the increasing winding speed the tear strength of the films decreases in MD; however, the data did not show any specific trend in CD. When the molecular orientation increases because of lower temperatures, tensile strength should increase according to the literature. However in this

work, as the temperature increased, tensile strength increased in MD. With increasing screw motor speed tensile strength of the films increases in MD; however, tensile strength of the films decreases in CD. With increasing winding speed the tensile strength of the films increases in MD; however, tensile strength of the films decreases in CD.

Nanoclay reinforced films having only 1% nanoclay content have more homogeneous nanoclay dispersion than the films having 3% nanoclay content. The films having 5% nanoclay content have better nanoclay dispersion compared to the other films. Screw speed was increased for the films having 5% nanoclay content. Since the screw speed was increased, shear stress increased. This caused the polymer and the nanoclay mix more homogeneously. According to the differential scanning calorimetry (DSC) results the melting points of the nanoclay reinforced films slightly increase as their nanoclay contents increase from 1% to 5%. Tensile tests showed that as the nanoclay contents increase, the extension of the films decreases. Nanoclay reinforced films having only 1% nanoclay content have higher tensile strength than the films having 3% nanoclay content. No specific result could be obtained about the effect of the compatibilizer content on tensile strength of the nanoclay reinforced films. Nanoclay reinforced films having only 1% nanoclay content have higher tear strength than the films having 3% nanoclay content. Since the screw speed was increased for the films having 5% nanoclay content in order to obtain a film structure, the films, having 5% nanoclay content, gained higher tear strength. Burst strength results show that as the nanoclay content of the nanoclay reinforced films increases from 1% to 5%, the extension of the films decreases. Nanoclay reinforced films having only 1% nanoclay content have higher burst strength than the films having 3% nanoclay content.

Acknowledgments

I would like to express my gratitude to my advisor Dr. Sabit Adanur, for giving me with the opportunity to pursue my doctor of philosophy degree.

I would like to give my appreciation to my committee members, Dr. Peter Schwartz and Dr. Carol Warfield for their contribution.

I really appreciate Dr. Ram Gupta for his guidance and for being an outside reader for my dissertation.

This study would not have been possible without the help of several people that I would like to thank: Mr. William David Clark for helping me to produce my samples with twin screw and single screw extruders, Dr. Ramsis Farag for teaching how to perform tensile, tear and burst strength tests, and how to operate the testing machines, Dr. Miller for helping in SEM analysis, and Dr. Edward Davis for giving information and helping while operating the twin screw extruder and single screw extruder machines.

I also appreciate the help of Mr. Jeff Thomson, and Mr. Steve Howard in several steps of this study.

The financial support from the U.S. Department of Commerce is gratefully acknowledged.

I would also like to express my most sincere thanks to my parents, Nuket and Riza Gocek, and my sister for always supporting me.

Table of Contents

List of Tables

List of Figures

List of Abbreviations

AFC	Alkaline Fuel Cell
BP	Bipolar Plates
CL	Catalyst Layer
DSC	Differential Scanning Calorimetry
EW	Equivalent Weight
GDL	Gas Diffusion Layer
HPA	Heteropoly Acid
HTPEM	High Temperature Polymer Electrolyte Membrane
MCFC	Molten Carbonate Fuel Cell
MFI	Melt Flow Index
N	Newton
PAFC	Phosphoric Acid Fuel Cell
PBI	Polybenzimidazole
PEEK	Polyetheretherketone
PEM	Polymer Electrolyte Membrane
PEMFC	Polymer Electrolyte Membrane Fuel Cell
PES	Polyethersulfone

PFSA Perfluorinated Sulfonic Acid Membranes

PP Polypropylene

PTA Phosphotungstic Acid

PTFE Polytetraflouroethylene

PWA Phosphotungstic Acid

SEM Scanning Electron Microscope

SOFC Solid Oxide Fuel Cell

TPA Tungstophosphoric Acid

CHAPTER 1

INTRODUCTION

1.1. Fuel Cell

Fuel cell converts the chemical energy in the fuel structure into electrical energy. This production goes on as long as the fuel is supplied [1].

There are five major types of fuel cells which are differentiated from each other by their electrolytes. These fuel cell types are [1, 2]:

1) Phosphoric acid fuel cell (PAFC)

   Concentrated phosphoric acid having a weight percentage of nearly 100 is used as the electrolyte. Silicon carbide (SiC) is used as the matrix to retain phosphoric acid. For anode and cathode, platinum is used as electrocatalyst. The range for operating temperature of phosphoric acid fuel cells is 150 to 220 °C.

2) Polymer electrolyte membrane fuel cell (PEMFC)

   Polymer electrolyte membrane fuel cells are also called as proton exchange membrane fuel cells. As electrolyte, thin proton conductive polymer membranes usually having a thickness of less than 50 μm are used for this kind of fuel cells. If

perfluorosulfonated acid polymers are used as electrolyte, the operating temperature can be in the range of 60 to 80 °C. Polymer electrolyte membrane fuel cells can be used for automotive applications, small scale distributed stationary power generation and portable power applications [1,2].

3) Alkaline fuel cell (AFC)

   Concentrated potassium hydroxide (KOH) having a weight percentage of 85 is used as the electrolyte for alkaline fuel cells for high temperature applications (above 200 °C) and less concentrated KOH having a weight percentage of 35 to 50 is used as the electrolyte for lower temperature applications (below 120 °C). Asbestos is used as a matrix to retain the electrolyte. Many types of electrocatalysts can be used for this kind of fuel cells. Nickel (Ni), silver (Ag), metal oxides and noble metals are some of the electrocatalysts that can be used for AFCs [1, 2].

4) Molten carbonate fuel cell (MCFC)

   The electrolyte for molten carbonate fuel cells has the combination of alkali carbonates such as lithium (Li), sodium (Na) and potassium (K). Ceramic matrix of $LiAlO_2$ retains these alkali carbonates. These fuel cells have an operating temperature range from 600 °C to 700 °C [1, 2].

5) Solid oxide fuel cell (SOFC)

   As the electrolyte, Y_2O_3 stabilized ZrO_2, which is a solid and non-porous metal oxide, is used for solid oxide fuel cells. The operating temperature is between 800 °C and 1000 °C [1, 2].

Polymer electrolyte membrane fuel cells are the subject of this study.

As mentioned before, polymer electrolyte membrane fuel cells (PEMFCs) have thin polymer membrane as the electrolyte, which is impermeable to gases and permeable to protons. Two porous, electrically conductive electrodes, which are made of carbon cloth or carbon fiber paper, take place at both sides of the membrane. Between the membrane and the electrodes, there is a layer containing catalyst particles (platinum supported on carbon).

The surface of the catalyst is the place where the electrochemical reactions take place. Hydrogen is fed from the anode side and it splits into protons and electrons. These protons pass through the polymer membrane. The electrons pass through the electrically conductive electrodes, current collectors and outside circuit and reach to the other side of the membrane which is called as the cathode. The electrons meet with the protons and oxygen at the catalyst layer between the interface of the membrane and the cathode and forms water with electrochemical reaction. As a result of these electrochemical reactions, electron current occurs through an external circuit [1, 2]. The PEMFC configuration, components and principles of operation can be seen in Figure 1.1.

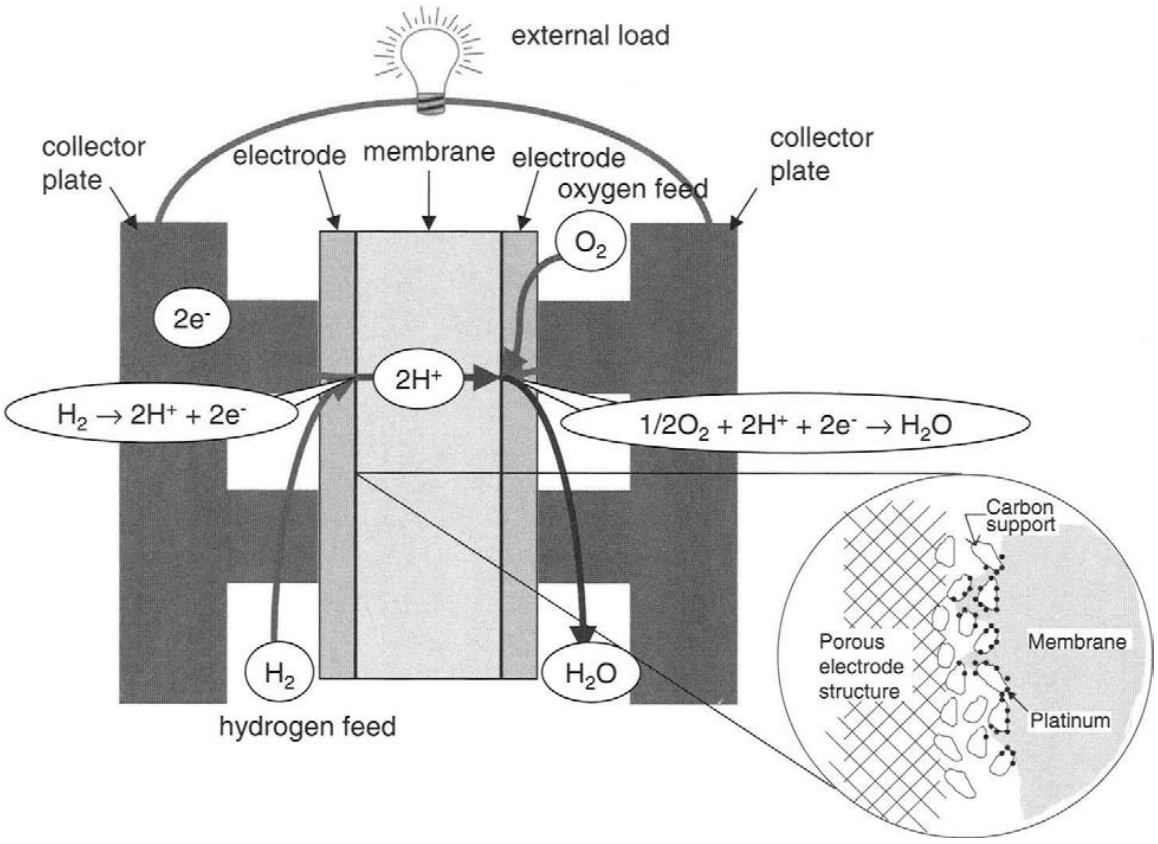

Figure 1.1 PEM fuel cell configuration and basic operation principles [2]

1.2. Fuel Cell Membranes

Among the different types of fuel cells, polymer electrolyte membrane fuel cells (PEMFC) are one of the best candidates for clean power source for various applications.

The polymer electrolyte membrane, which has the function of proton exchange, is the main part of the cell. The common membranes that are used for PEMFCs are perfluorinated polymers having sulfonic acid groups on side chains. However, at temperatures higher than 80 °C, this kind of membranes require higher water content to provide enough proton conductivity which causes the fuel cell performance to drop. Operating the fuel cell at temperatures above 100 °C provides various advantages such as improved impurities tolerance, more efficient heat

rejection and more useful waste heat [3]. Therefore, polymer electrolyte membranes that can operate at temperatures above 100 °C are the subject of current research. To increase the fuel cell performance at high temperatures, the polymer electrolyte membrane must have better water retention characteristics to allow higher proton conductivity that improves fuel cell efficiency.

In order to extend the fuel cell operation temperature range, novel membranes having different material properties such as higher thermal stability than Nafion® need to be produced.

A material that is used for high temperature polymer electrolyte fuel cells is polybenzimidazole (PBI). Polybenzimidazoles are usually used after they are doped with acids because they gain high proton conductivity with no or low humidification after doping with acids. Especially phosphoric acid is used to dope polybenzimidazoles.

Another approach to improve the proton transport and mechanical stability of perfluorinated sulfonic acid membranes (PFSA) such as Nafion® at high temperatures is to fill the membrane with inorganic materials. These inorganic materials are hygroscopic and help with water retention for operation of PEM fuel cells at higher temperatures and lower relative humidity. For this purpose, research is being done on Nafion® – Silica and Nafion – Titanya composite membranes. These inorganic materials help to develop self-humidifying polymer electrolyte membranes (PEM).

All of the research that has been done proves that improving the characteristics of the membranes for high temperature applications helps to improve the performance of PEMFCs. Therefore, the attention must be focused on producing novel membrane structures or novel materials for high temperature PEMFCs.

CHAPTER 2

LITERATURE REVIEW

2.1. Perfluorosulfonic Membranes

Commercial membranes for fuel cells are typically made of perfluorocarbon-sulfonic acid ionomer. This ionomer is a copolymer of tetrafluoroethylene and many perfluorosulfonate monomers. The most popular perfluorosulfonic membrane is Nafion™ which is made by Dupont [2]. Hydrophobic perfluorinated polyethylene backbone and highly hydrophilic sulfonic acid terminated perfluoro vinyl ether pendant develops nanoscale domains where ionic transport occur [4].

Figure 2.1 shows the chemical structure of Nafion®. Typically x has the value of 7 and y has the value of 1. Nafion ® is used as a membrane for PEMFCs because of its high proton conductivity, chemical stability and longevity; however, it has some disadvantages that need to be improved. Firstly, Nafion® is an expensive material. Secondly, it does not perform well at operation conditions having high temperatures and low relative humidity which makes it require external humidification and water management [4].

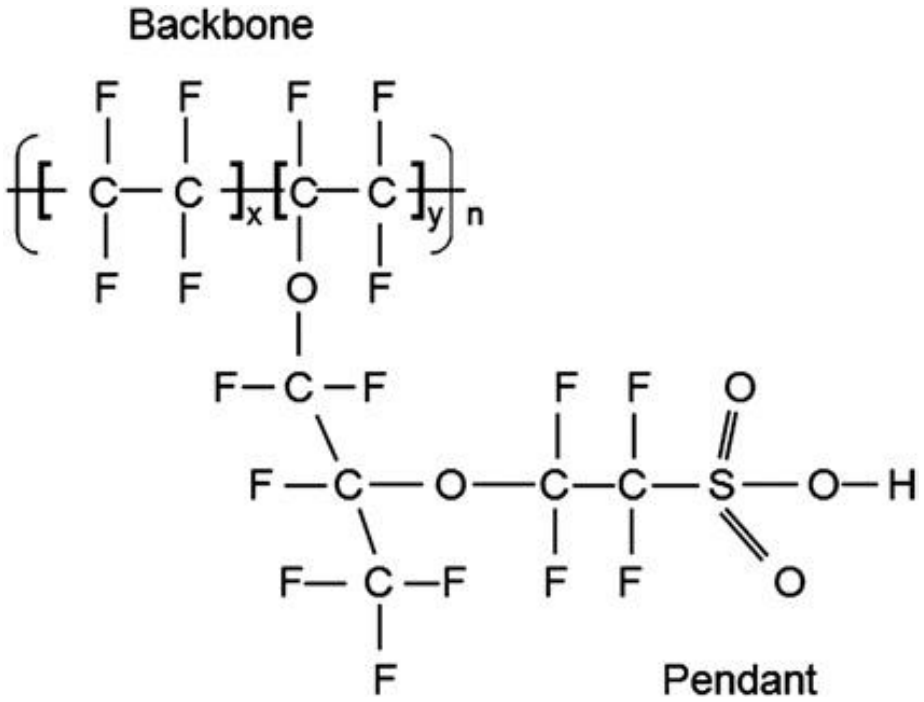

Figure 2.1 Nafion®'s chemical structure [4].

Liquid water is needed for proton dissociation from the SO_3H groups and proton transport in Nafion® since water molecules help to transfer protons. Membrane requirement for liquid water lowers the operating temperature below 80 °C. Protons that pass through the humidified membrane carry the water molecules from anode side to cathode side which is called electro-osmotic drag. Electro-osmotic drag in PEMFC can be seen in Figure 2.2. However, there is also a back flow of water molecules from cathode side to anode side which is driven by the water concentration gradient. This phenomenon is called back diffusion. If there is an imbalance between these two forward and back flows, drying of anode catalyst layer, flooding of the catalyst layer, mechanical stresses in the membrane or delamination of the catalyst layer can occur. In addition, external systems for managing water through the membrane make the volume, weight, complexity and cost of the system higher.

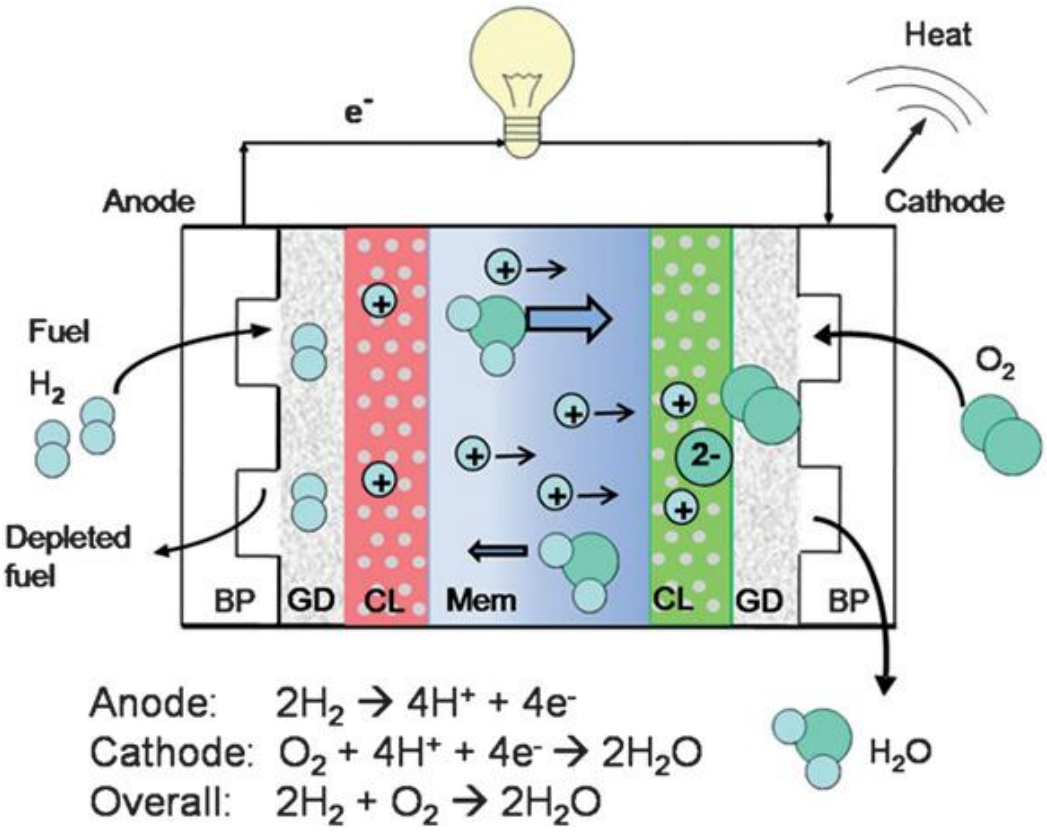

Figure 2.2 Electro-osmotic drag in a PEMFC. BP (bipolar plates), GD (gas diffusion layers), CL (catalyst layers) and Mem (membrane) [4].

Different PFSA membranes are being developed to increase the PEMFC operating temperatures over 80 °C. These membranes are modified perfluorinated or partially fluorinated and have shorter side chains as compared with Nafion®, which reduces the equivalent weight (EW) of the membrane. As the EW decreases to a certain level, proton conductivity increases; however, some problems develop with the durability and mechanical integrity because of the increased swelling of the membrane.

The Dow Chemical Company produced short-side-chain membrane having an EW of 800-900. It is reported that this membrane has four times the power of Nafion® membrane operating at the same voltage since Nafion® has an EW of 1100 [4].

Other companies produced similar kind of short-side-chain membranes as well. For example, Solvay Solexis, Inc., developed Hyflon Ion® which has 850-870 EW.

Other Nafion®-like membranes are Flemion® produced by Asahi Glass Co. Ltd, Aciplex® produced by Asahi Chemical Co. Ltd., 3M membrane produced by 3M Inc. and Gore Select® produced by W.L. Gore and Associates, Inc.

These short-side-chain membranes offer advantages at higher operating temperatures as compared with Nafion® since they have higher crystalllinity at a given EW and a higher glass transition temperature [4].

Properties of some commercial membranes can be seen in Table 2.1.

Table 2.1 Properties of some commercial membranes [5]

Supplier and trade mark	Equivalent weight (IEC; mequiv. g^{-1})	Thickness (μm)
Dupont		
Nafion® 120	1200 (0.83)	250
Nafion® 117	1100 (0.91)	175
Nafion® 115	1100 (0.91)	125
Nafion® 112	1100 (0.91)	50
Asahi Glass		
Flemion® T	1000 (1.00)	120
Flemion® S	1000 (1.00)	80
Flemion® R	1000 (1.00)	50
Asahi Chemicals		
Aciplex® S	1000-1200 (0.83-1.00)	25-100
Dow Chemical		
Dow®	800 (1.25)	125
Solvay Solexis, Inc.		
Hyflon® Ion	900 (1.11)	

2.2. Membranes for HTPEMFCs

Since the common perfluorosulfonic acid membranes cannot be used for high temperature applications, different polymers and systems are used for high temperature polymer electrolyte membrane fuel cells [6].

This kind of membranes are aromatic hydro-carbon based membranes. Many novel polymers having aromatic backbones can be used for HTPEMFCs such as polyetheretherketone (PEEK), polyethersulfone (PES) and polybenzimidazole (PBI) [4].

The most preferred polymer for HTPEMFC membrane is polybenzimidazole (PBI). PBI has good chemical and mechanical stability in the temperature range of 120 to 200 °C. The structure of PBI can be seen in Figure 2.3.

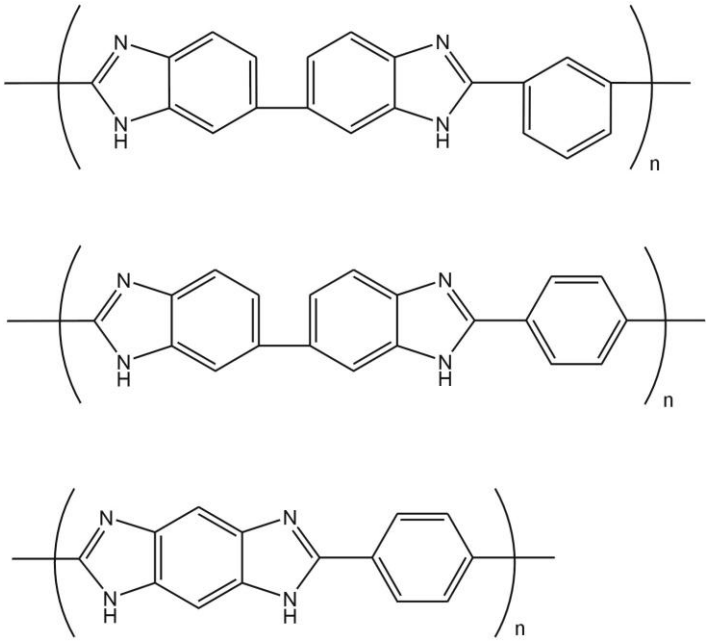

Figure 2.3 Structures of some PBIs [7]

As it is mentioned before, for HTPEMFC applications, PBI is used after it is doped with phosphoric acid, H_3PO_4. Phosphoric acid is a weak acid and it generates a hydrogen bonded network to increase conductivity without humidification after PBI is doped with it. As the doping level, temperature and humidification increase after PBI is doped with phosphoric acid, the protonic conductivity of the membrane also increases.

Doping level is an important parameter for the doping process of PBI. The doping level can be defined as the number of molecules of phosphoric acid per repeat unit of PBI. For PBI, the optimum doping level is 5. As the doping level drops below this value, the conductivity is affected negatively and as the doping level exceeds this value, mechanical strength decreases.

2.3. Composite Membranes

Some membranes have composite structures to enhance the physical, mechanical and chemical properties in order to achieve composite structure for membranes, different materials and techniques are used. Reinforcement of polymeric membranes, preparation of composite and hybrid membranes are some of the methods used. Sandwich membrane structures are also used with good results.

A non-conductive polymer for enhancing the mechanical properties, a conductive and non-conductive inorganic phase for enhancing thermal stability in addition to conductivity and water uptake properties and a compound that can be easily oxidized for reducing the degradation of the conducting polymer are reinforcement types that are used for the production of polymeric membranes. A solution of a functionalized polymer can be impregnated into a non-conductive porous substrate in order to enhance the mechanical properties of the membrane. Organic polymers showing mechanical and chemical resistance are used as porous substrate. Porous

PTFE sheets as ultra thin membranes or micro PTFE fibrils can be used to reinforce the composite perfluorosulfonic acid membranes and develop thin membrane technology. Although PTFE has weak adhesion onto the conducting polymer, it enhances the electrical resistance of the membrane. At least 95% PTFE as the reinforcing polymer and a conductive fluoropolymer can be mixed as copolymer and extruded in the form of droplets that can be sputtered to produce membranes. Membranes that are produced by this method have lower resistance to current flow and higher power than a membrane that has porous substrate. On the other hand, the minimum thickness of 100 or 200 μm is a disadvantage for these membranes for fuel cell applications [5].

Composite membranes can be produced from fluoropolymers that are doped with fillers or solid inorganic proton conductors such as zirconium hydrogen phosphates, hygroscopic oxides, heteropolyacids (HPA), phosphotungstic acid (PWA, PTA), etc. There are some other polymers used for high temperature PEMFC membranes. One of the most widely used polymers for this purpose is PBI. Polybenzimidazole (PBI) is a polymer that is used especially for intermediate temperature PEMFCs. When PBI is doped with phosphoric acid, it gains outstanding thermo-chemical stability, lower gas permeability and good proton conductivity. Therefore, PBI is used after it is doped. As poly(2,2-m-(phenylene)-5,5-bibenzimidazole) has a glass transition temperature of 425-435 °C, it has excellent thermal stability to be used in high temperature PEMFCs [8]. Also AB-PBI, poly(2.5-benzimidazole) that is a kind of PBI, shows outstanding performance in PEMFCs. In a research to enhance the durability of H_3PO_4/PBI membrane for real commercial operations, the Nafion®-PBI composite membrane was produced from a blend solution of Nafion®-Na and PBI in N,N'-dimethylformamide (DMF) by using the casting method [9]. Other polymers such as sulfonated poly(arylene ether sulfone), sulfonated polybenzimidazole and PTFE can be used with various different fillers. Some other composite

membranes that have outstanding conductivities can be produced by using the blend of PVDF and poly(styrene) sulfonic acid [5].

In today's novel high performance materials, an important topic is using nano-ordered composite materials that include organic polymers and inorganic components. The hybrid organic-inorganic membranes having nano-sized phases and interfaces are intriguing alternatives to polymeric membranes that can provide high temperature operations for fuel cells. Thermal stability can be enhanced by the inorganic component and proton conductivity can be provided by the organic component. Moreover, the inorganic phase enhances the chemical stability and the membrane proton conductivity at high temperatures by improving the water retention at higher temperatures [10].

There are some inorganic substances that are used for doping during production of PEMFC composite membranes in order to enhance the proton conductivity. These materials can be metal oxides such as TiO_2, SiO_2, ZrO_2 and acids such as heteropoly acids (HPA), phosphoric acid, solid acid named as $Cs_{2.5}H_{0.5}PM_{12}O_{40}$ (CsPOM), etc. Noble metals such as platinum, palladium, rhodium, ruthenium and iridium and nanosized particles such as nanoclays can be used to improve the physical, chemical and mechanical characteristics of the membranes.

Nafion®/silica composite membranes can be produced by the sol-gel acidocatalysation of tetraethoxysilane (TEOS) in a Nafion 115 membrane which has en equivalent weight of 1100. As the reaction time changes, the amount of TEOS that can be impregnated into the membrane changes. Due to the silica content, the water absorption of the composite membrane can be improved; however, the proton conductivity can be lowered. The silica particles cause the inhibition of proton transfer.

CHAPTER 3

MEMBRANE PRODUCTION USING SINGLE SCREW EXTRUDER

3.1. Machine Set Up and Operation

Wayne single screw extrusion machine was used in the project. The extrusion machine consists of hopper, barrel with heading zones, metering pump, control panel for temperature and pressure control, 15.24 mm (6”) wide film die, cylinders to form and to draw the film, air blowing unit to cool the film, and winding unit. The machine has a capability of combining two films by introducing a second film at the winding stage to the film that is extruded from the die. The general structure of a single screw extruder can be seen in Figure 3.1 and a cast film die can be seen in Figure 3.2. Figures 3.3 - 3.9 show the main parts of the Wayne single screw extrusion machine which was used in this study in order to produce polypropylene and nanoclay reinforced polypropylene films. This machine was purchased recently and a considerable amount of fine was spent on setting up the machine and start producing membranes successfully.

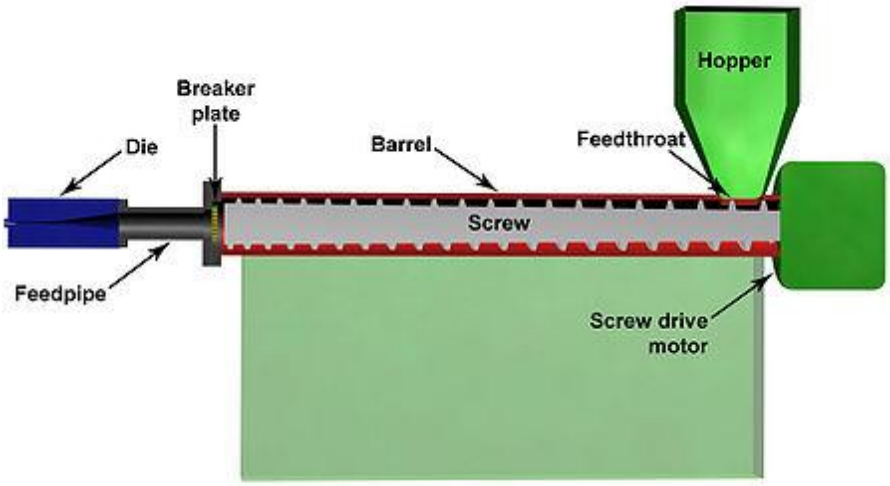

Figure 3.1 Schematic of a plastic extruder [11].

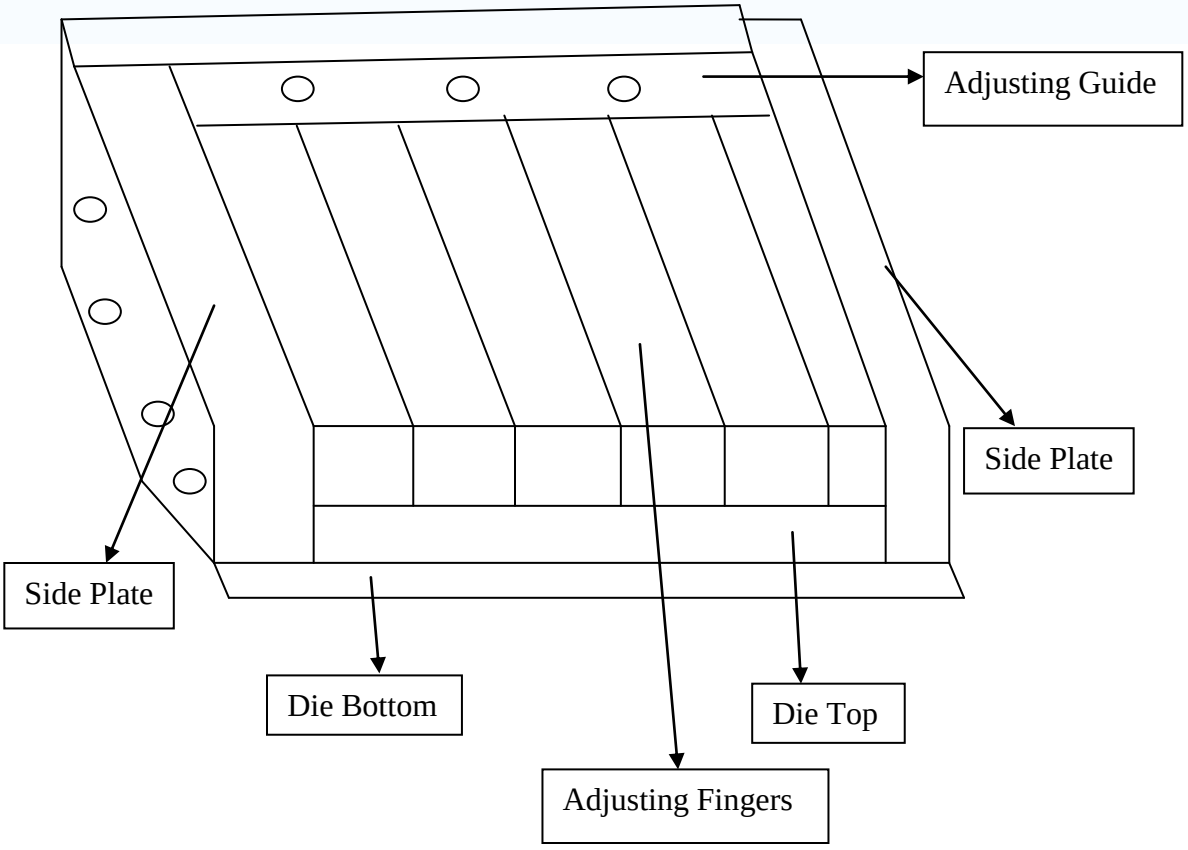

Figure 3.2 Schematic of the extrusion film die.

Figure 3.3 Wayne single screw extruder

Figure 3.4 Hopper of the single screw extruder

Figure 3.5 Barrel of the single screw extruder

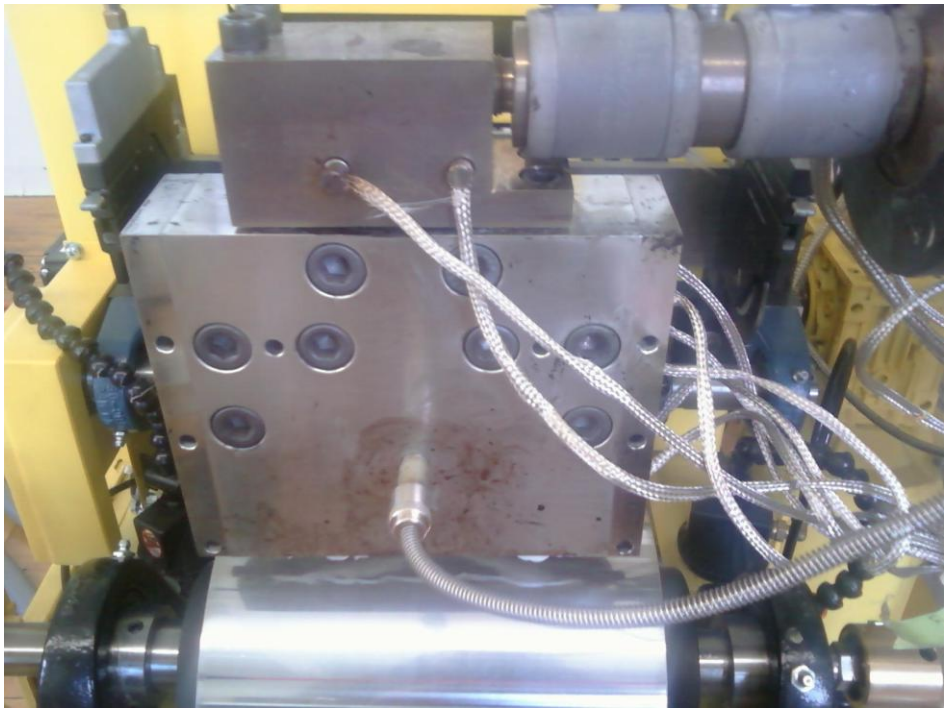

Figure 3.6 Cast film die of the single screw extruder

Figure 3.7 Air blowing and drawing unit of the single screw extruder

Figure 3.8 Winding unit of the single screw extruder

Figure 3.9 Control panel of the single screw extruder

3.2. Effect of Processing Parameters

Polypropylene was used to study the effect of the processing parameters during film manufacturing.

3.2.1. Introduction

Polypropylene (PP) finds various new uses in commercial film applications due to its product properties such as thickness, resistance to tear, tensile and burst, transparency, clarity, gloss and haze. Since PP has high tensile strength and elongation at break, low permeability and good chemical resistance as well as low price, it has been used in various packaging and other specialty applications [12].

The characteristics of cast PP films show differences not only due to their chemical structures and the additives and resin modifiers added but also due to their processing parameters in extrusion process. Therefore, determining the effect of processing parameters and process conditions in cast film extrusion is important to obtain the exact properties of the films for their end uses.

Cast film technology is the simplest technology to produce polymeric films in which the molten polymer is extruded through a slot die, fed by a single-screw extruder, onto a chilled roll in order to be cooled. Then, the solidified film is taken up from the chilled roll by a nip roll (take up roll) and transferred to a winding unit after the edges are trimmed. A limited amount of orientation is obtained in the film by this process; the orientation can be affected by the ratio between the die thickness and film thickness and by the ratio between the extrusion speed and the take up speed. Since the orientation can be easily determined in this method, cast film technology is a low cost and easy-to-handle process.

Temperature, screw motor speed and winding speed are the processing parameters that have effect on cast films. The final molecular orientation in a product depends on the thermomechanical history (melt temperature, stress, strain) of the product during processes [13]. It was reported that lower die temperature reduces the mobility of the chains to be extended at high draw ratios at the die exit [12]. Increasing screw motor speed results in the shear rate increase. At a given melt temperature, the higher the shear rate the higher the shear stress, which results in more molecular orientation in a product [13].

The aim of this study is to determine the effects of processing parameters such as temperature, screw motor speed and winding speed on the physical and structural characteristics

and mechanical performance of unmodified and pure PP cast films such as thickness, crystallinity, tear strength, tensile strength and burst strength.

3.2.2. Experimental

3.2.2.1. Materials and Equipments Used

Polypropylene pellets commercially named as "30 Melt Copolymer Natural" with a density of 0.91 g/cm^3 and an MFI of 34 g/10 min were bought from Premier Plastic Resins Company. No modifiers and additives were added while producing the PP cast films.

Wayne single screw extrusion machine having a 15.24 cm cast film die was used to produce polypropylene (PP) cast films in combination with a chill roll and a nip (take up) roll. The die melt was quenched onto a chill roll. The film was taken up through a pair of nip rolls onto a winder.

For tensile, tear and burst strength testing, Instron 5565 universal testing machine was used, which has 5 kN capacity and 0.001-1000 mm/min speed range. Thickness measurements were done using Testing Machines Inc., (TMI) micrometer. Crystallinity tests were performed on all film samples using a TA Instruments DSC Q-2000 differential scanning calorimetry (DSC).

3.2.2.2. Manufacturing and Testing

Twelve PP films were produced by using cast film technology. The machine parameters such as temperature, screw speed and winding speed were changed during production to observe their effects on film final properties. The machine parameters that were changed during the manufacturing process can be seen in Table 3.1. The barrel temperatures were the same along the barrel from feed end to the die for each sample.

Table 3.1 Machine parameters changed during manufacturing process of the films

Sample	Temperature (°C)	Screw Motor Speed (RPM)	Winding Speed (m/s)
Film1	190	400	0.1
Film2	205	400	0.1
Film3	215	400	0.1
Film4	220	400	0.1
Film5	225	400	0.1
Film 6	220	300	0.1
Film7	220	500	0.1
Film8	220	600	0.1
Film 9	220	400	0.12
Film 10	220	400	0.13
Film 11	220	400	0.15
Film 12	220	400	0.16

Thickness, tensile, tear and burst strength tests were performed on the samples. The effect of temperature on film thickness, tear, tensile and burst strength was investigated on films 1,2,3,4 and 5; the screw motor speed effect was investigated on films 4, 6, 7 and 8 and the winding speed effect was investigated on films 9, 10, 11 and 12. The tests were performed both in machine direction (MD) and cross direction (CD).

For tensile tests, "ASTM D 882-02 Standard Test Method for Tensile Properties of Thin Plastic Sheeting" test method was used. The nominal width of the specimens was 25.4 mm. The grip separation (gauge length) was 50 mm; the test specimens were 50 mm longer than the grip

separation. The rate of grip separation (cross head speed) was 500 mm/min. Five specimens were tested from each sample for the tensile tests [14].

For tear tests, "ASTM D 1938-06 Standard Test Method for Tear-Propagation Resistance (Trouser Tear) of Plastic Film and Thin Sheeting by a Single-Tear Method" was used. The nominal width of the specimens was 25.4 mm; the length of the test specimens was 80 mm. The grip separation (gauge length) was 50 mm. The rate of grip separation was 250 mm/min. Five specimens were tested from each sample for the tear tests [15].

For burst strength tests, "ASTM D 6797-02 Standard Test Method for Bursting Strength of Fabrics Constant-Rate-of-Extension (CRE) Ball Burst Test" was used. The specimens have the dimensions of 125 x 125 mm. The CRE machine was started with a speed of 305 mm/min. and the speed was kept constant till the specimens bursted. Five specimens were tested from each sample for the burst tests [16]. For thickness tests, 10 measurements were taken from each sample. For crystallinity tests, samples were heated from -50 °C to 350 °C at a temperature increase of 10 °C/min.

3.2.3. Results and Discussion

3.2.3.1. DSC Analysis and Crystallization

DSC tests were performed on all of the films. Since the melting peaks of all samples did not change much, it was concluded that the change of the crystal thickness was negligible (Figure 3.10). Therefore, the main difference in the crystalline structure of the PP films is thought to be caused by the orientation of the crystal blocks [17].

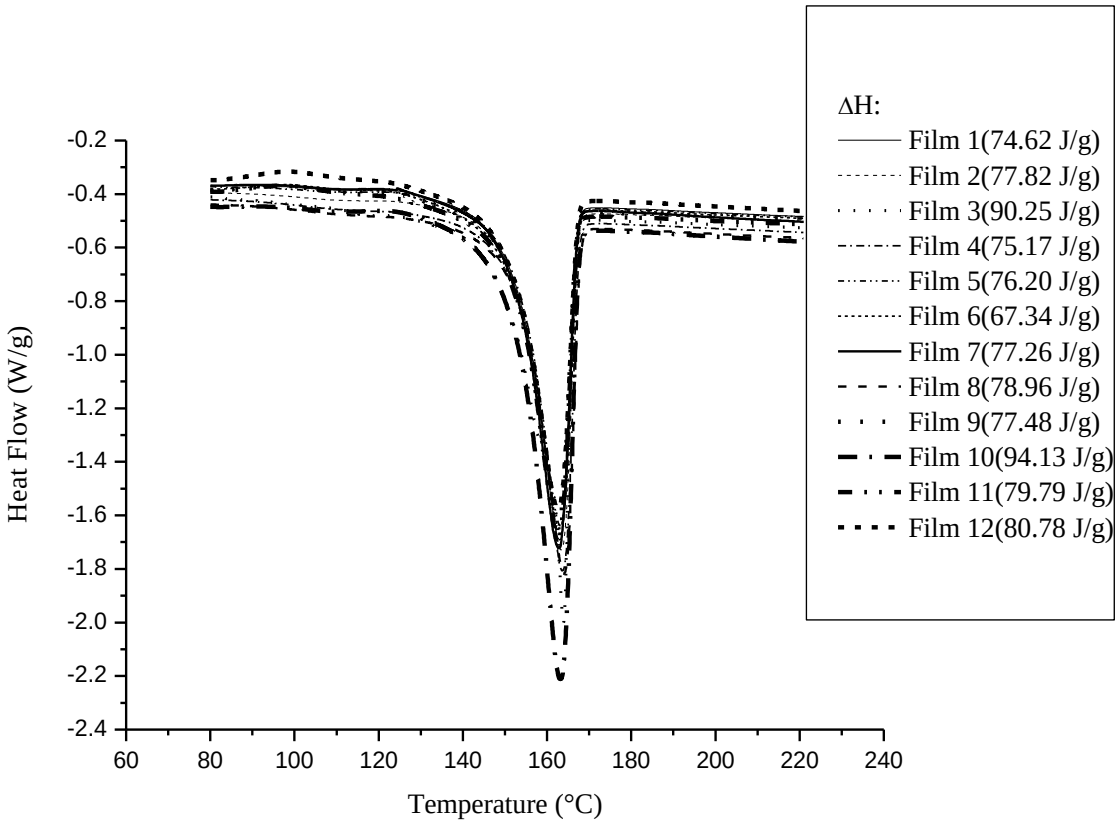

Figure 3.10 DSC of the PP films (heating rate: 10 °C/min)

Films 1, 2, 3, 4 and 5 were analyzed to examine the effect of temperature on crystallinity. Although the areas under the curves of DSC graphs and ΔH values (a parameter that can be used for defining crystallinity) fluctuate (Figure 3.10), they show a slightly increasing trend. As the temperature is increased during PP film production process, the crystallinity of the films increases slightly as shown in Figure 3.11.

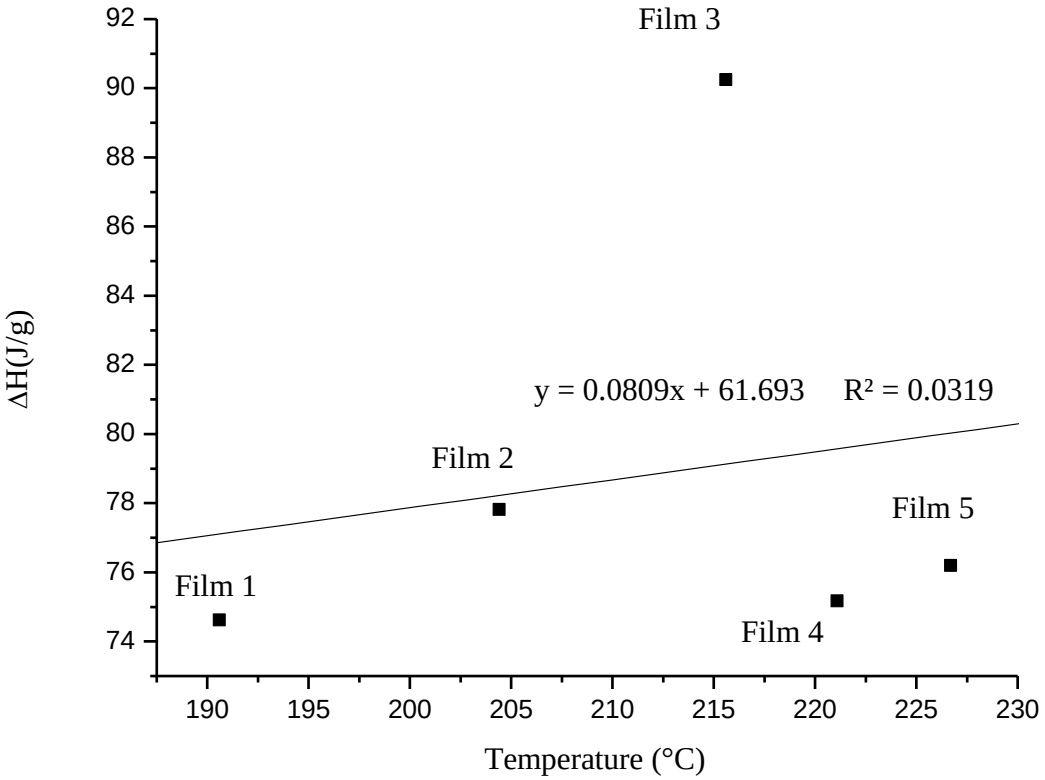

Figure 3.11 Effect of temperature on crystallinity

Films 4, 6, 7 and 8 were analyzed to examine the effect of screw motor speed on crystallinity. As the screw motor speed increases, ΔH value increases (Figure 3.12).

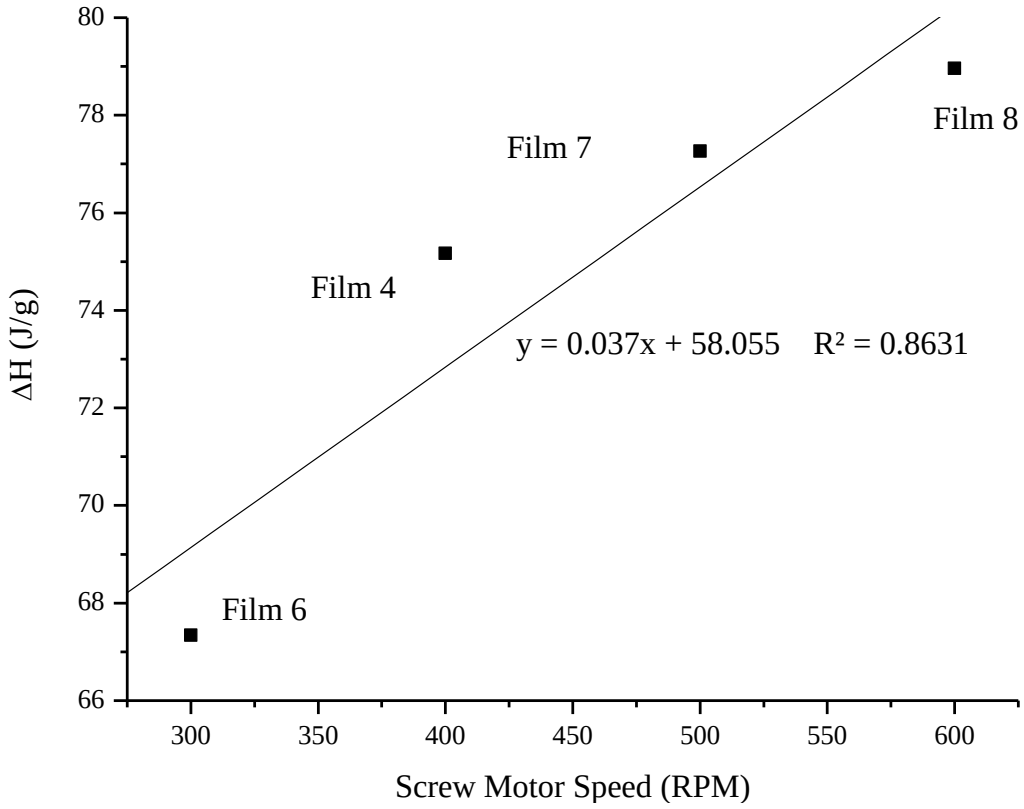

Figure 3.12 Effect of screw motor speed on crystallinity

Films 9, 10, 11 and 12 were analyzed to examine the effect of winding speed on crystallinity. Although the areas under the curves of DSC graphs and ΔH values fluctuate (Figure 3.13), this is not enough to reach a conclusion about the winding speed and crystallinity relation.

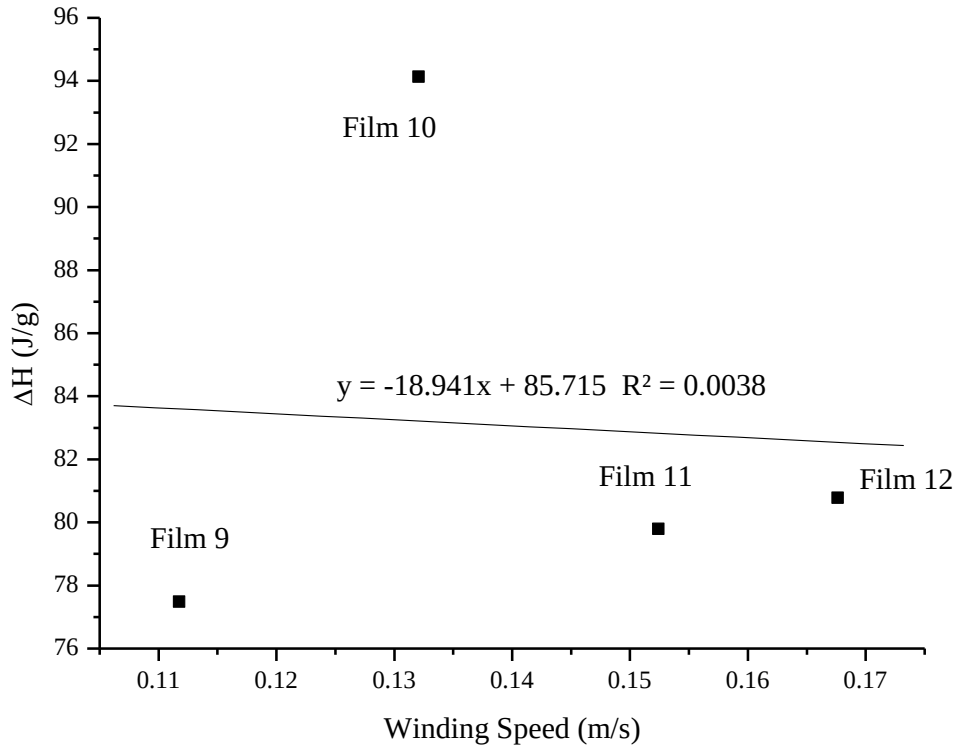

Figure 3.13 Effect of winding speed on crystallinity

3.2.3.2. Thickness Analysis

The results of thickness tests for all of the 12 PP film samples can be seen in Table 3.2.

Table 3.2 Thickness test results

Film #	**1**	**2**	**3**	**4**	**5**	**6**	**7**	**8**	**9**	**10**	**11**	**12**
Thickness (mm)	0.0355	0.0356	0.0321	0.0345	0.0356	0.0224	0.0484	0.0522	0.0332	0.0267	0.0221	0.0209

One of the extrusion machine parameters in film manufacturing process is temperature. Therefore, thicknesses of the films 1, 2, 3, 4 and 5 were measured to analyze the effect of temperature on thickness (Figure 3.14). As the temperature increases, the thickness of the films decreases since the viscosity of the films decreases with increasing temperature.

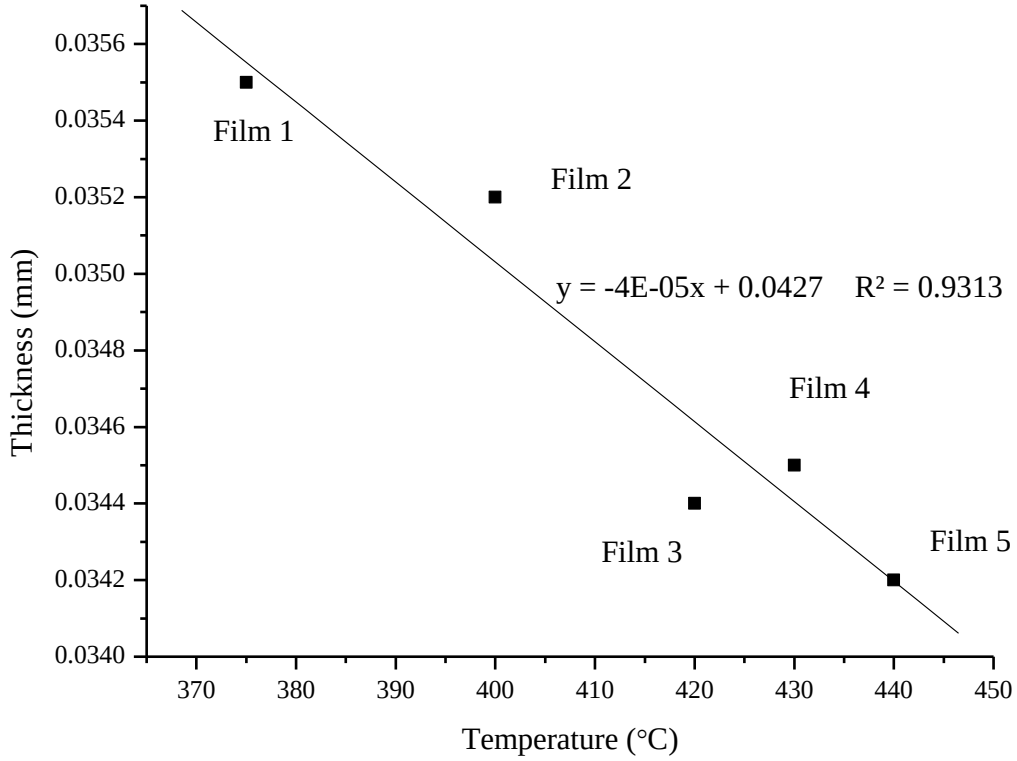

Figure 3.14 Effect of temperature on film thickness

Another extrusion machine parameter in film manufacturing process is the screw motor speed. Thicknesses of the films 4, 6, 7 and 8 were measured to analyze the effect of screw motor speed on thickness (Figure 3.15). As the screw motor speed increases, the thickness of the films also increases since the screw transfers more polymer from the barrel to the die.

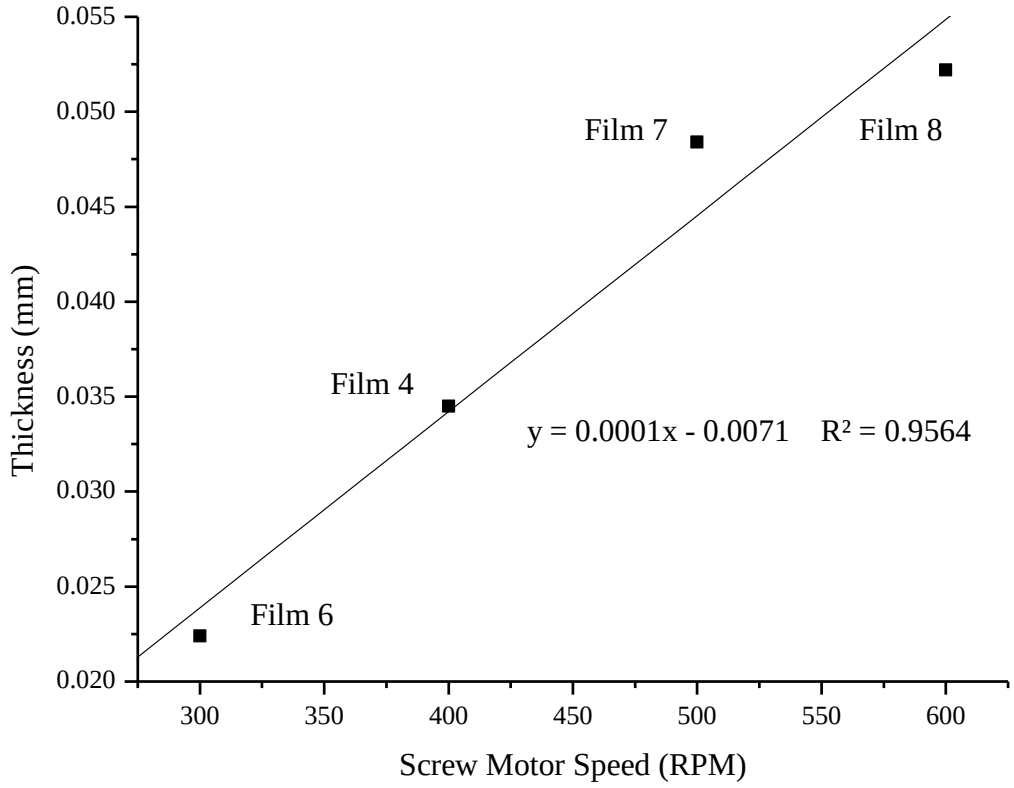

Figure 3.15 Effect of screw motor speed on film thickness

To analyze the effect of winding speed on thickness, thicknesses of the films 9, 10, 11 and 12 were measured (Figure 3.16). As the winding speed increases, the thickness of the films drops since the increase in winding speed stretches the films and makes them thinner.

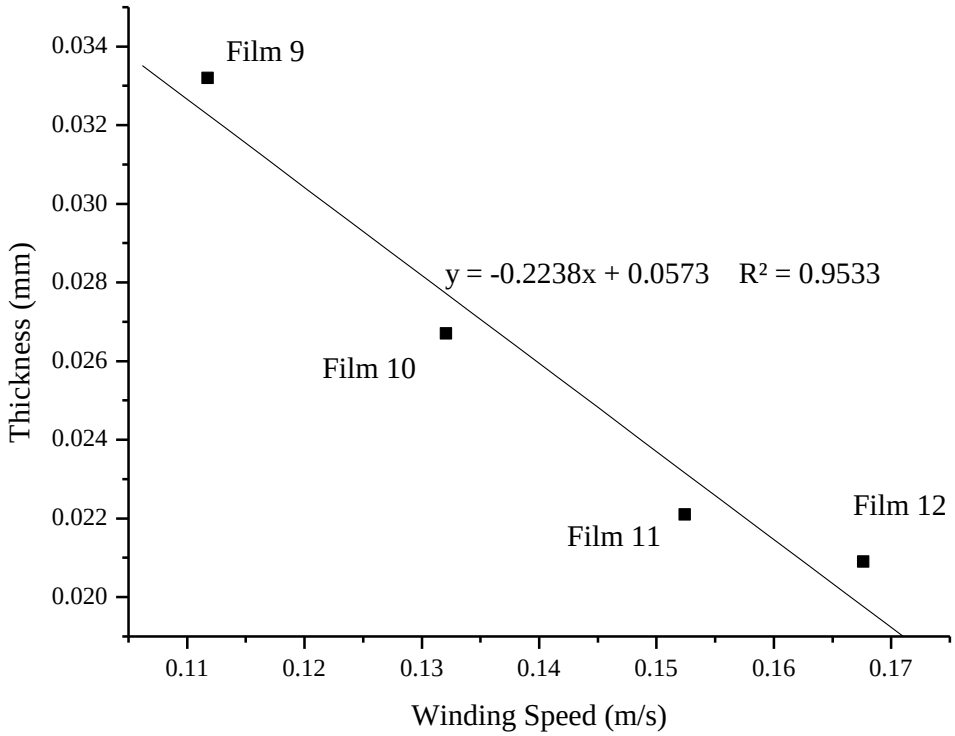

Figure 3.16 Effect of winding speed on film thickness

3.2.3.3. Tear Strength Analysis

Tear strength of the films 1, 2, 3, 4 and 5 were measured to determine the effect of temperature on tear strength (Figure 3.17). As the temperature increases, tear strength of the films increases in MD. Since the polymer chains become more oriented in MD as the temperature decreases, tear strength becomes higher with increasing temperature. As the temperature increases, tear strength of the films decreases in CD since the polymer chains are less oriented in MD and less force is needed to tear the polymer chains in CD.

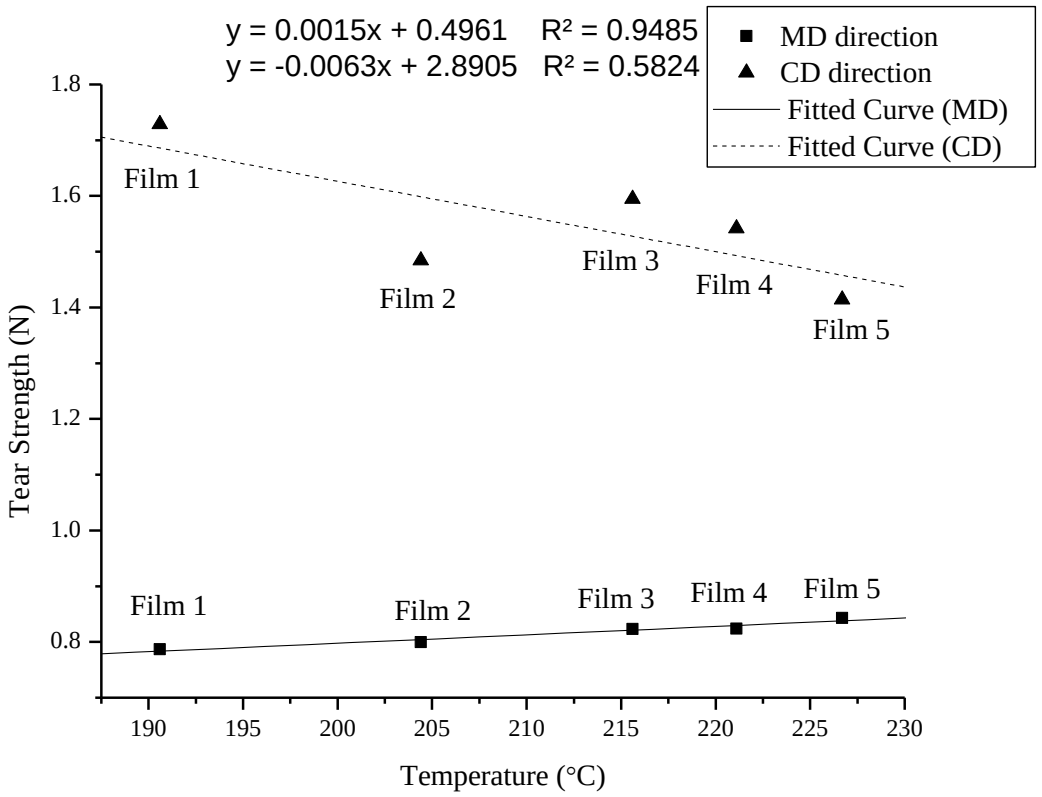

Figure 3.17 Effect of temperature on tear strength of the films

To analyze the effect of screw motor speed on tear strength, tear strengths of the films 4, 6, 7 and 8 were measured (Figure 3.18). Although with increasing screw speed, the tear strength in MD is expected to decrease, the data do not show any specific trend. Therefore, no conclusion can be made from the data obtained. The shear rate increases with increasing screw motor speed. At a given melt temperature, higher shear rate gives higher shear stress, resulting in more molecular orientation in a product. The amount of molecular orientation is proportional to the magnitude of stress. Since the molecular orientation improves in MD, tear strength of the films increases in CD with increasing screw motor speed.

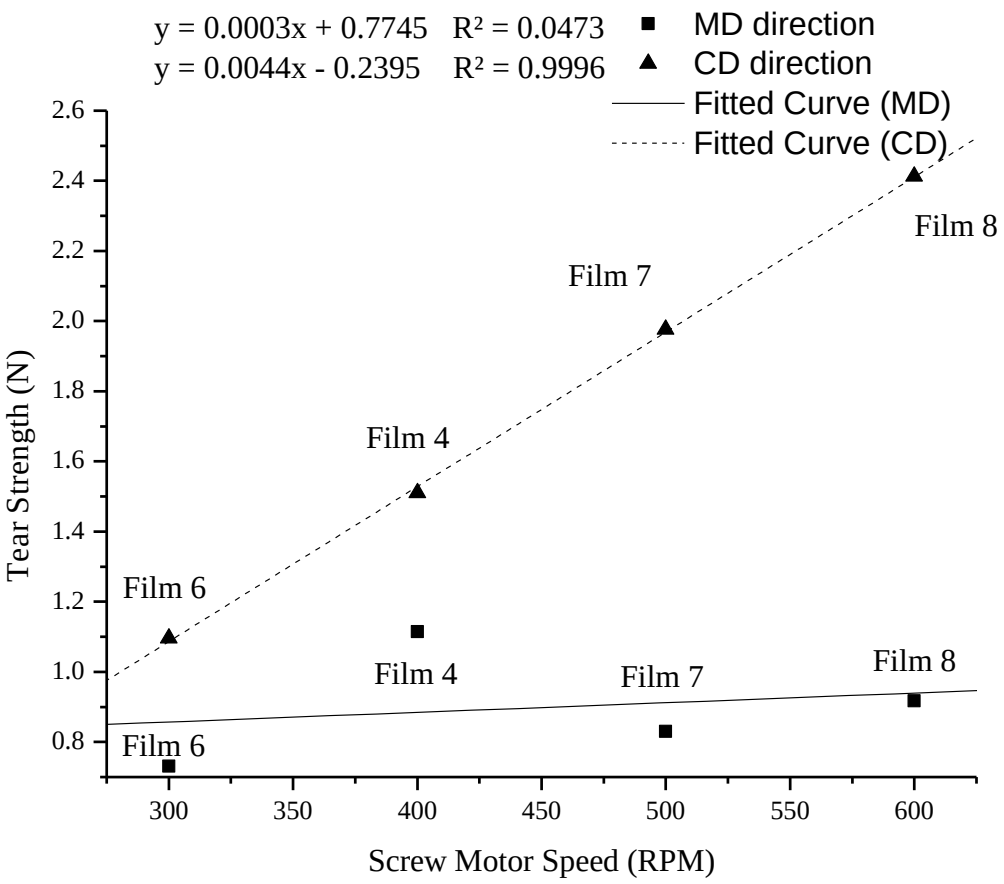

Figure 3.18 Effect of screw motor speed on tear strength of the films

To analyze the effect of winding speed on tear strength, tear strengths of the films 9, 10, 11 and 12 were measured (Figure 3.19). As the winding speed increases, the tear strength of the films drops in MD. The orientation in MD increases due to high draw ratio. Therefore, tear strength in MD decreases with increasing winding speed. Although the tear strength of films is expected to increase in CD with increasing winding speed, the data show no specific trend.

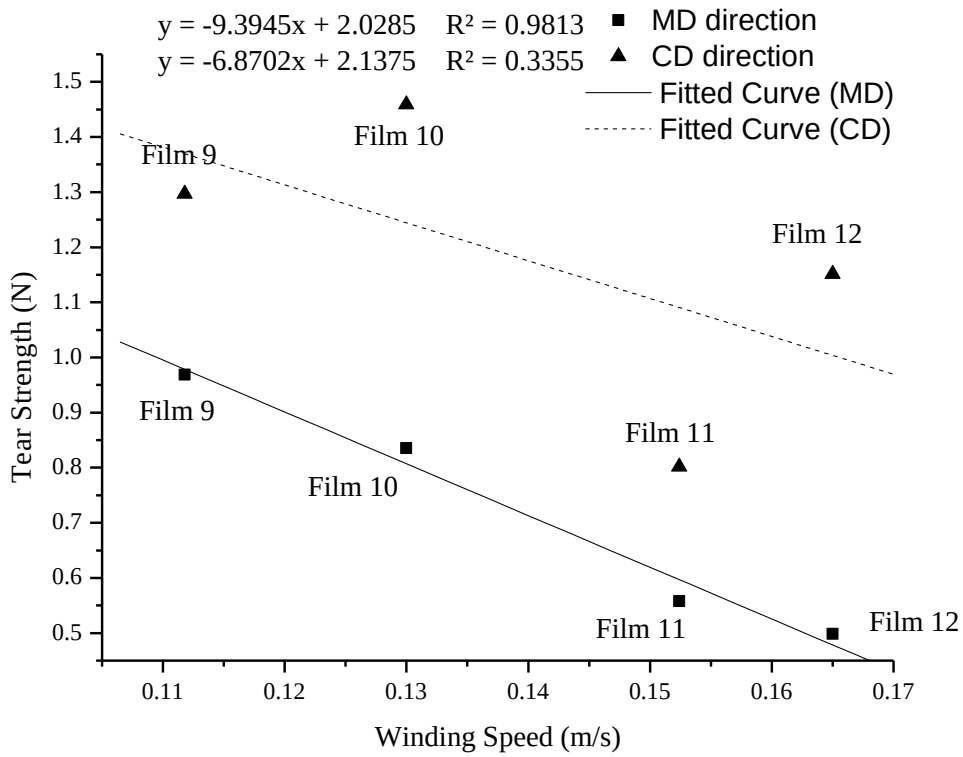

Figure 3.19 Effect of winding speed on tear strength of the films

3.2.3.4. Tensile Strength Analysis

Tensile strength of the films 1, 2, 3, 4 and 5 were measured to determine the effect of temperature on tensile strength (Figure 3.20). At a given shear rate, lower melt temperature gives higher viscosity, resulting in higher shear rate. Lower melt temperature or higher shear rate gives rise to higher shear stress, resulting in more molecular orientation in MD. Therefore, as the molecular orientation increases due to lower temperatures, tensile strength increases. However, from Figure 3.20, it can be seen that as the temperature increases, tensile strength increases both in MD and CD.

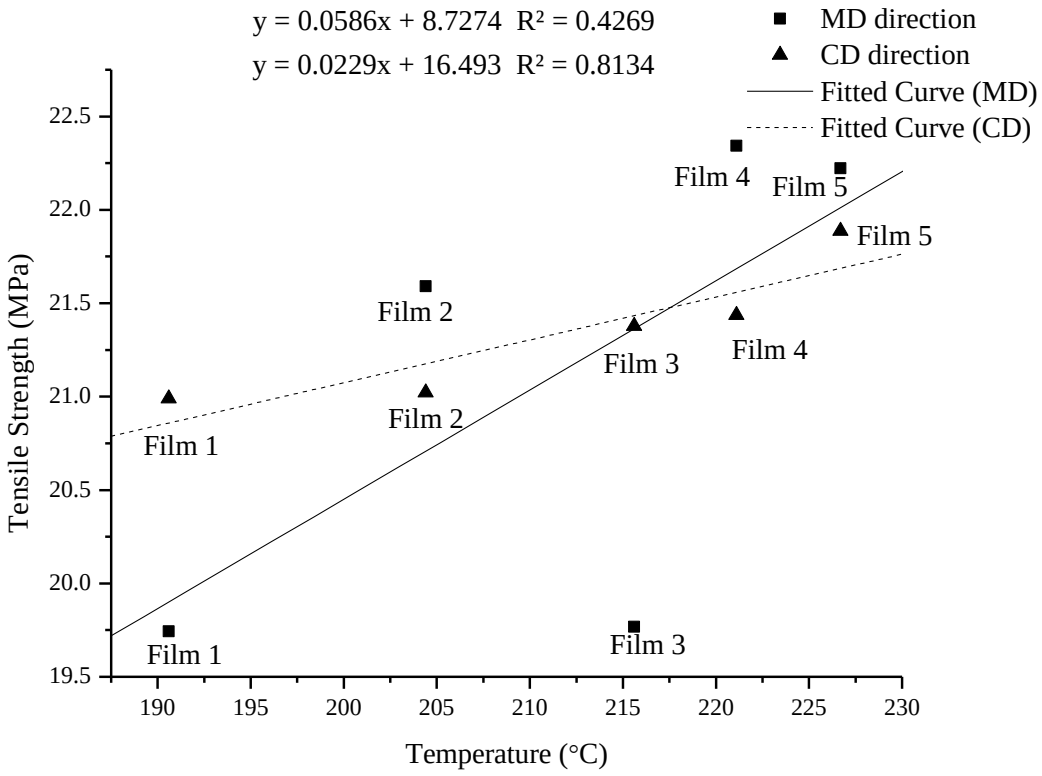

Figure 3.20 Effect of temperature on tensile strength of the films

To analyze the effect of screw motor speed on tensile strength, tensile strengths of the films 4, 6, 7 and 8 were measured (Figure 3.21). The shear rate increases with increasing screw motor speed. At a given melt temperature, higher shear rate gives higher shear stress, resulting in more molecular orientation in a product. Since the molecular orientation increases in MD, the tensile strength of the films increases in MD. Tensile strength of the films decreases with increasing screw motor speed in CD because of the orientation in MD.

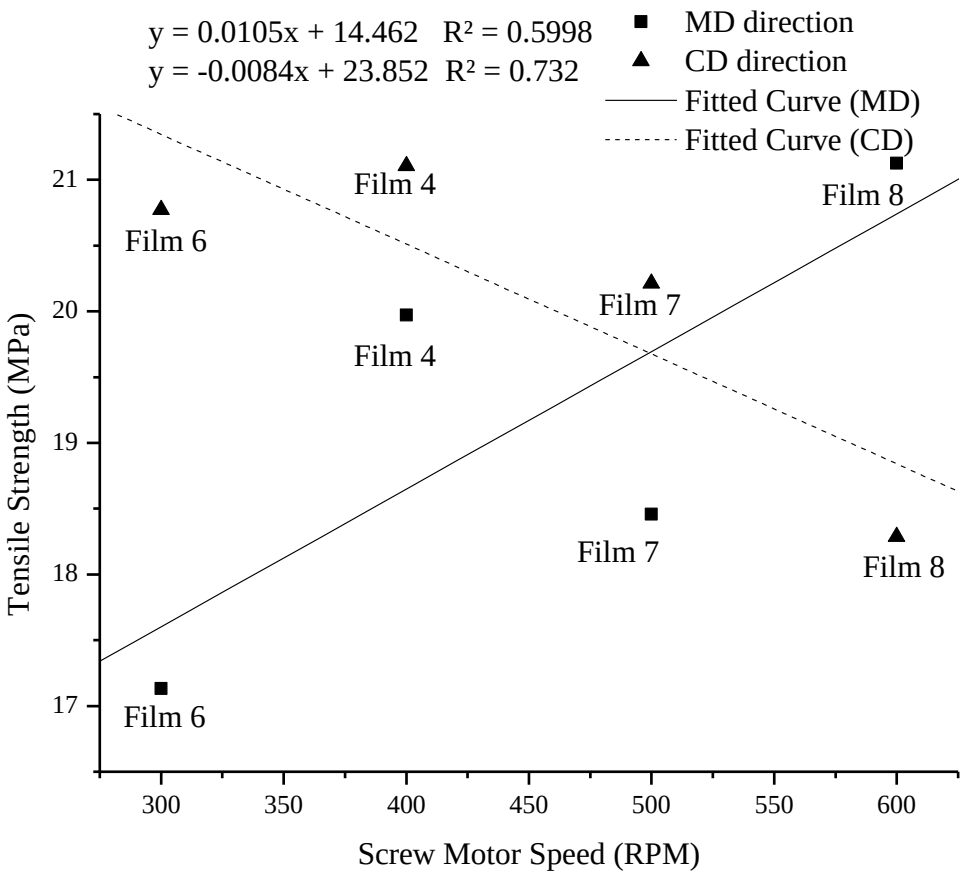

Figure 3.21 Effect of screw motor speed on tensile strength of the films

To analyze the effect of winding speed on tensile strength, tensile strengths of the films 9, 10, 11 and 12 were measured (Figure 3.22). As the winding speed increases, the tensile strength of the films increases in MD since the orientation in MD improves due to the increasing draw ratio. The tensile strength of films decreases in CD with increasing winding speed due to the orientation increase in MD.

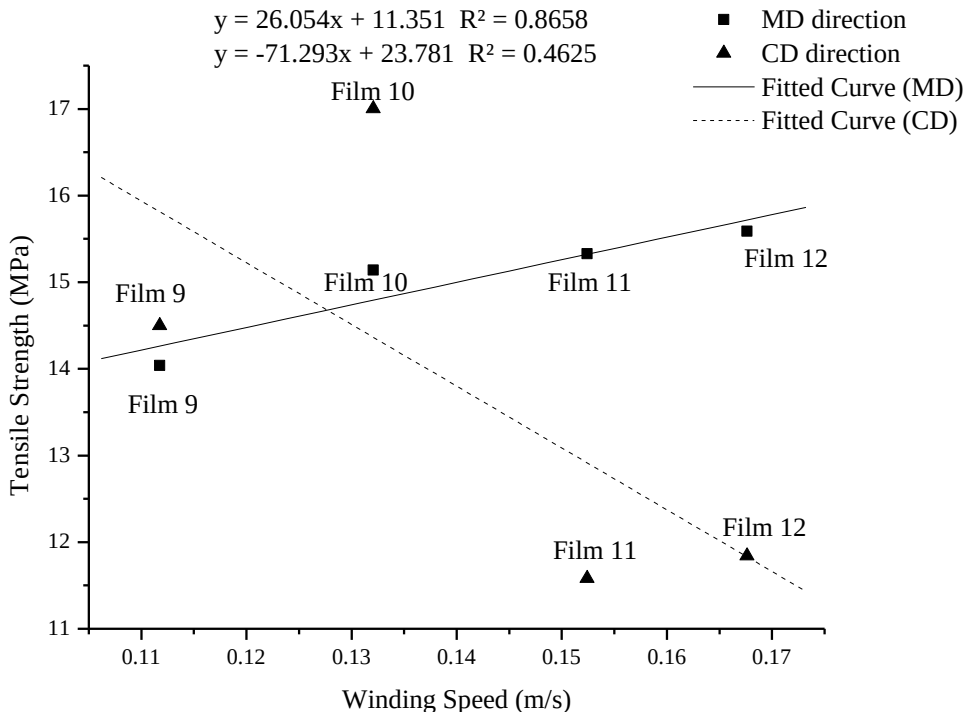

Figure 3.22 Effect of winding speed on tensile strength of the films

3.2.3.5. Burst Strength Analysis

During the burst strength tests, only Film 6 bursted. The tests were done by using Instron universal testing machine and there was not enough space in the machine's bursting strength equipment for highly stretchable films to extend. The graphs of the other 11 films did not show any decreasing trend at 45 mm extension. This means that the graphs obtained did not have their maximum loads since they have an increasing trend. Therefore, the burst strength values, stress at the maximum load, could not be obtained for the other 11 films.

As it is seen in Figure 3.23, the graphs of all of the films show a similar trend. For the same extension value, 45 mm, Film 11 gives the lowest load value (not considering Film 6) while Film 8 gives the highest load value.

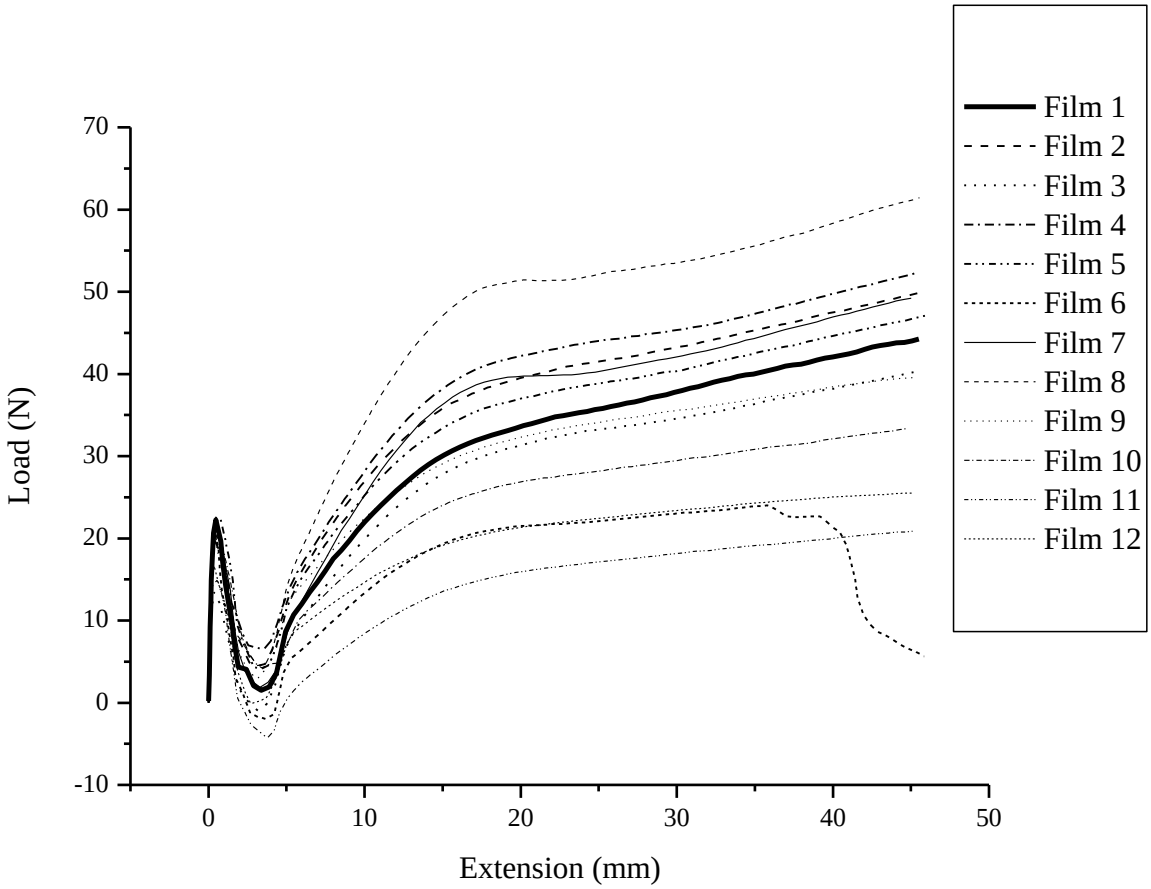

Figure 3.23 Burst strength of the films

The films exhibit early load peaks at the extension of nearly 0.4-0.8 mm range, but then their load values begin to decrease as the extension increases. The load values begin to increase from the extension range of 3.2-4.2 mm to the extension 45 mm.

3.2.4. Conclusions

In this work, twelve different PP cast films were manufactured and analyzed to find the effects of machine parameters such as temperature, screw speed and winding speed on film properties such as crystallinity, thickness, tear strength, tensile strength and burst strength. These analyses were done in MD and CD directions for tear and tensile strength.

From the DSC analysis it was found that the position of the melting peak did not have a significant change. Because of this, it was assumed that the crystal thickness change was negligible. Therefore, the main difference in the crystalline structure of the PP films is considered to be caused by the orientation of the crystal blocks.

The thickness analysis was done by considering temperature, screw motor speed and winding speed. It was found that when the temperature increases, the thickness of the films decreases since the viscosity of the films decreases with increasing temperature. As the screw motor speed increases, the screw transfers more polymer from the barrel to the die which results in increase of film thickness. Increase of winding speed causes the films to be stretched, making them thinner.

Since the polymer chains become less oriented in MD as the temperature increases, tear strength becomes higher with increasing temperature. When the temperature increases, tear strength of the films decreases in CD since the polymer chains are less oriented in MD and less force is needed to tear the polymer chains in CD. Although it is expected that increasing screw speed decreases the tear strength in MD, tear strength of the films does not show any specific trend as the screw motor speed increases; as a result no conclusions can be made from the data obtained. Tear strength of the films increases in CD with increasing screw motor speed because the molecular orientation increases in MD**.** When the winding speed increases, the tear strength of the films decreases in MD because the orientation in MD increases due to high draw ratio. Therefore, when winding speed increases, tear strength in MD decreases. Although the tear strength of films should increase in CD with increasing winding speed, the data show no specific trend.

When the molecular orientation increases because of lower temperatures, tensile strength should increase according to the literature. However in this work, as the temperature increased, tensile strength increased in MD. When screw motor speed increases, the shear rate also increases. At a given melt temperature, higher shear rate gives higher shear stress which causes higher molecular orientation in the product. Molecular orientation increase in MD causes the tensile strength of the films to increase**.** Tensile strength of the films decreases with increasing screw motor speed in CD due to the orientation in MD. Increase in winding speed causes the tensile strength of the films to increase in MD since the orientation in MD increases because of the increasing draw ratio. The tensile strength of films decreases in CD with increasing winding speed because of the orientation increase in MD.

Except Film 6, the films did not burst in burst strength tests. Therefore, burst stress at the maximum load could not be obtained for the other 11 films.

CHAPTER 4

NANOCLAY REINFORCED MEMBRANE STRUCTURES USING TWIN AND SINGLE SCREW EXTRUDERS

4.1. Introduction

Polymer layered silicate (PLS) nanaocomposites have gained attention recently since the final composite product shows improvement on mechanical, barrier, thermal and some other properties as compared with its polymer matrix. Furthermore, silicate based nanoclays that these nanocomposites are made from are environmentally friendly, naturally abundant and economical [18].

Nanoclay reinforced composites are one type of nanoplatelet-reinforced composites. In their bulk state, clays exist as layered materials. These natural or organically modified clays have a stacked structure of parallel silicate layers in their pure state. In order to use nanoclays more efficiently, there must be a good layer separation and uniform dispersion throughout the polymer matrix phase. The morphology of nanoclay reinforced polymer composites can be seen in Figure 4.1 [18, 19].

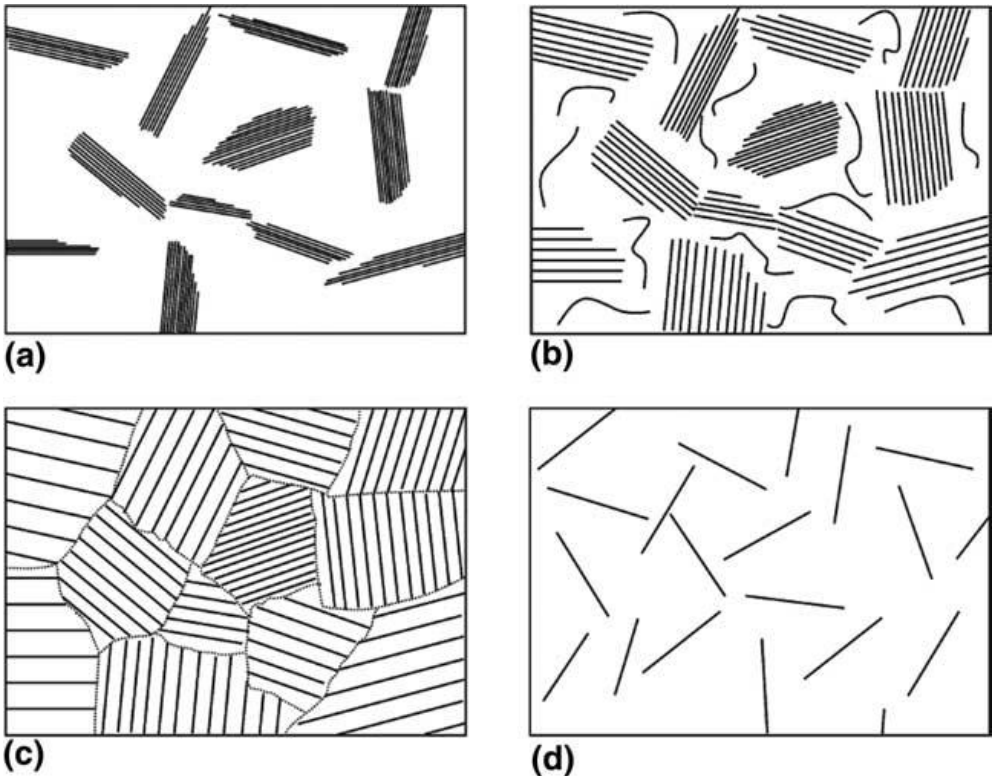

Figure 4.1 Schematics of the polymer-clay nanocomposite morphologies: a) conventional miscible b) partially intercalated and exfoliated c) fully intercalated and dispersed d) fully exfoliated and dispersed [19].

The interlayer spacing of a clay particle is minimum in the conventional miscible state. After insertion of polymer resin into the place between adjacent layers of a clay particle, the interlayer spacing gets larger. This state is called as intercalated state. The state is called as exfoliated state if fully separation of the layers of clay particle is achieved. Intercalated and exfoliated clay layers can be seen in Figure 4.2 and 4.3. For nanocomposites, the clay layers must be intercalated or exfoliated and must not be aggregated as tactoids [18, 19].

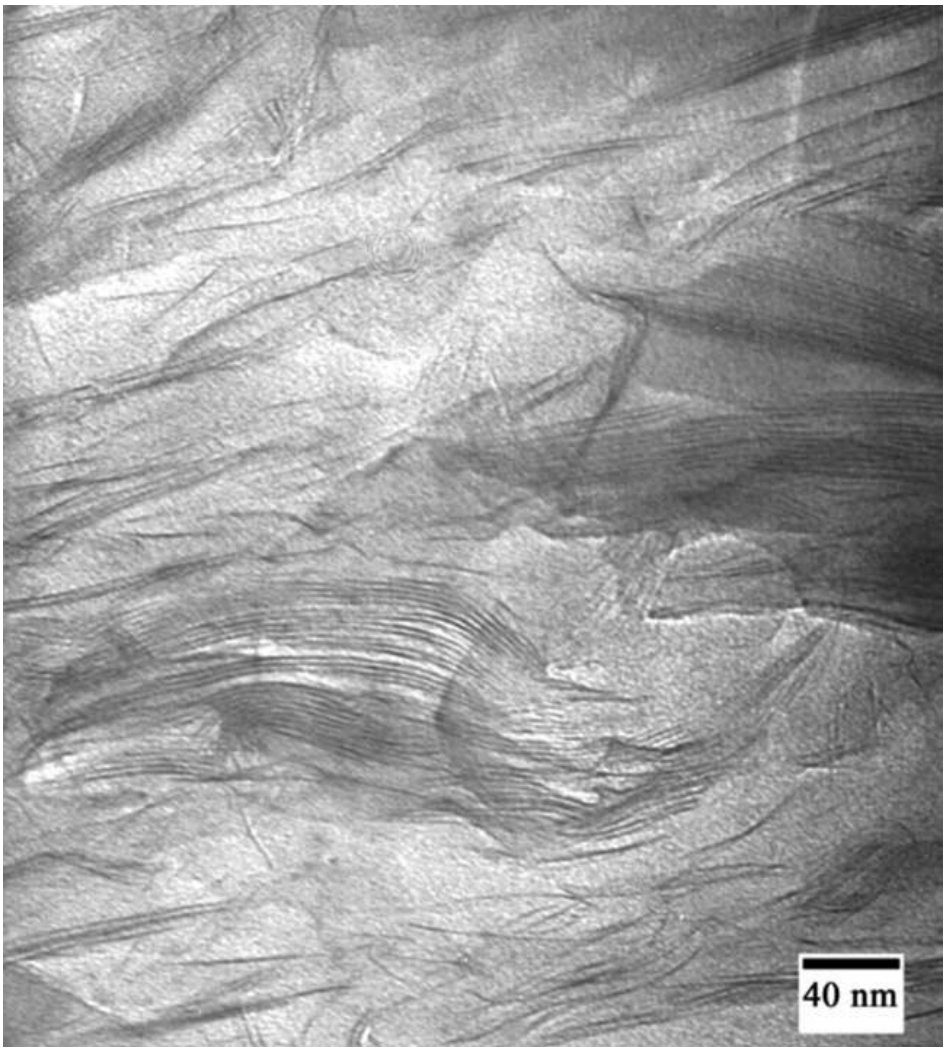

Figure 4.2 Intercalated and exfoliated states of TEM micrograph of a montmorillonite poly (L-lactic acid) [19].

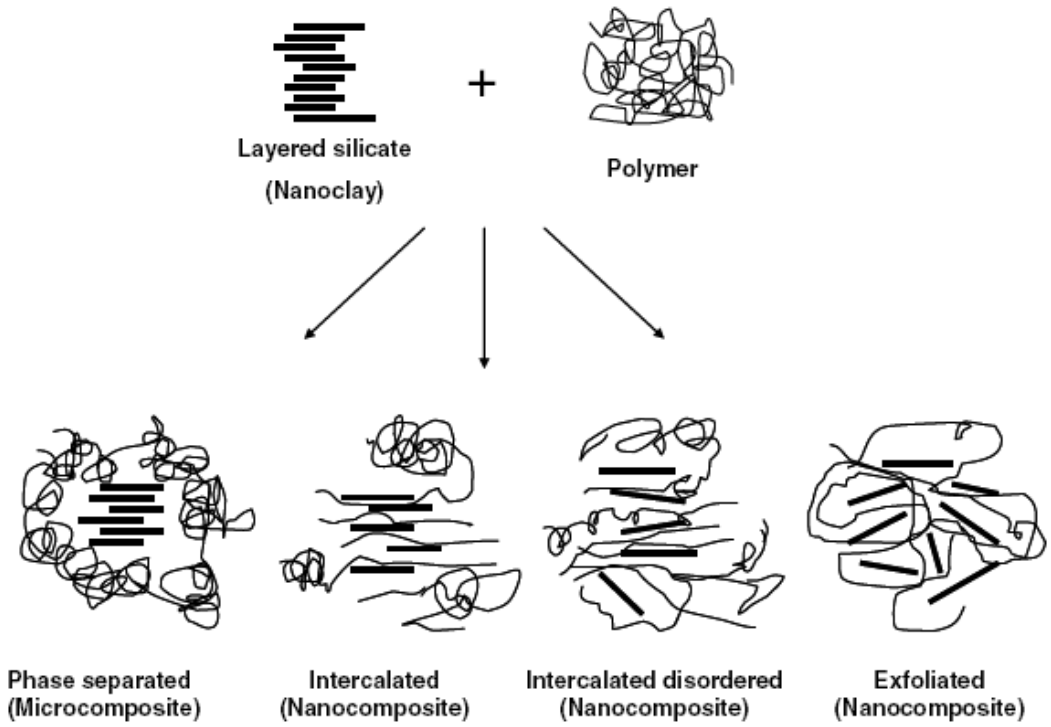

Figure 4.3 Schematic representation of intercalated and exfoliated nanocomposites [18].

The most widely used clay materials are montmorillonite, saponite and synthetic mica. Properties that nanoclay materials provide for polymeric materials are improved stiffness, strength, toughness, thermal stability, reduced gas permeability and coefficient of thermal expansion [19].

Sometimes, agglomeration of the mineral in the polymeric matrix can occur because of the lack of affinity between hydrophilic silicate and hydrophobic polymer. In order to solve this problem, surface modification is performed for clay particles [19].

Many matrix polymers have been used for PLS nanocomposite production such as nylon, polystyrene and polypropylene which are synthetic, non-degradable, and polylactide and starch which are biopolymers [18].

It has been proven that small amounts of montmorillonite nanoclay addition increases the tensile strength, tensile modulus, and heat degradation temperature (HDT) of Nylon 6/clay hybrid. Moreover, if the platelets are well dispersed in the polymeric matrix, the composites gain higher load transfer efficiency [19]. Properties of Nylon 6/clay nanocomposites can be seen in Table 4.1.

Table 4.1 Properties of Nylon 6/clay nanocomposites [19]

Sample	Wt% clay montmorillonite	Tensile strength (MPa)	Tensile modulus (GPa)	Charpy impact strength (kJ/m^3)	HDT at 18.5 kg cm^{-2} (°C)
NCH-5	4.2	107	2.1	2.1	152
NCC-5	5.0	61	1.0	1.0	89
Nylon 6	0	69	1.1	1.1	65

Furthermore, thermal stability, fire resistance and gas barrier properties of nanoclay reinforced polymer composites can be increased by addition of nanometer scale reinforcement.

Nanoclay/polypropylene composites are used as functional parts in automobiles.

4.2. Experimental

4.2.1. Materials and Equipments Used

Polypropylene pellets commercially named as “30 Melt Copolymer Natural” with a density of 0.91 g/cm^3 and an MFI of 34 g/10 min were bought from Premier Plastic Resins Company.

Cloisite® 15A, which is an organically modified montmorillonite clay, was used as nanoclay (supplied by Southern Clay Products). Cloisite® 15A consists of organically modified nanometer scale, layered magnesium aluminum silicate platelets. Cloisite® 15A is a natural montmorillonite modified with a quaternary ammonium salt [20].

Fusabond® P M613-05 which was supplied by DuPont, was used as compatibilizer; it is a chemically modified polypropylene. Fusabond® P M613-05 has an MFI (190 °C/1000 g) of 49 g/10 min and a melting point of 162 °C (324 °F) [21].

Leistritz Micro 27 twin screw extrusion machine having two co-rotating screws of 27 mm diameter was used for melt intercalation (Figures 4.4, 4.5, 4.6, and 4.7). This is a lab extruder that provides compounding and reaction processes for production settings [22]. PP pellets, Fusabond® P M613-05 compatibilizer and Cloisite® 15A nanoclay were mixed by using the twin screw extruder. The temperature profile of extrusion was the same from the feed zone to the die at 220 °C. The mixtures were extruded at a screw speed of 200 RPM. Extruded strands of the molten composite were then water quenched and pelletized.

Figure 4.4 Leistritz twin screw extrusion machine

Figure 4.5 Control panel of the twin screw extruder

Figure 4.6 Polymer feeder and hopper of the twin screw extruder

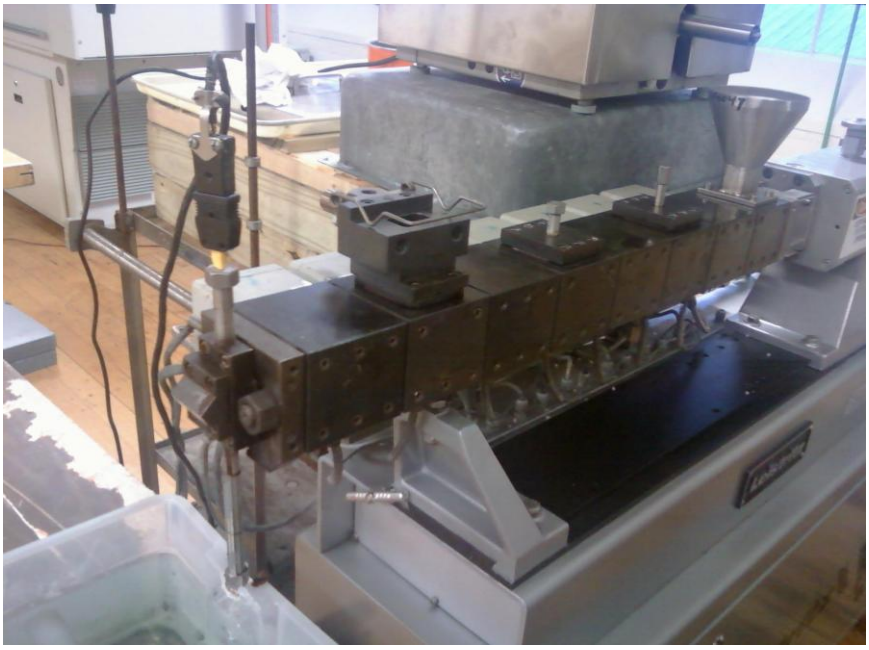

Figure 4.7 Barrel and filament die of the twin screw extruder

Wayne single screw extrusion machine having a 15.24 cm wide cast film die was used to produce nanoclay reinforced polypropylene (PP) cast films in combination with a nip (take up) roll. The films were taken up through a pair of nip rolls onto a winder.

For tensile, tear and burst strength testing, Instron 5565 universal testing machine was used, which has 5 kN capacity and 0.001-1000 mm/min speed range (Figure 4.8).

Figure 4.8 Instron 5565 universal testing machine **[23]**

Thickness measurements of nanoclay reinforced PP films were done using Testing Machines Inc., (TMI) 49-72 series micrometer. This micrometer has digital display and motorized automatic cycling [24].

For morphology analysis of nanoclay reinforced PP films, Carl Zeiss EVO 50 VP scanning electron microscope (SEM) operating at 20 kV was used [25].

Before phase morphology analysis of the nanoclay reinforced film specimens, gold sputtering was done for each specimen. The electrically conductive thin coating is representative

of the surface of the specimen. The coating inhibits charging, reduces thermal damage, and improves secondary electron emission, which are beneficial for scanning electron microscopy. For gold sputtering, EMS 550X sputter coating device, which has multi specimen holder and is capable of fully automatic control and high resolution fine coating, was used. It has a deposition rate of 0-25 nm/min [26].

4.2.2. Manufacturing and Testing

Nine nanoclay reinforced PP films were produced using cast film technology. For the films having nanoclay content of 5%, the screw motor speed was 690 RPM; for the other films, the screw motor speed was 500 RPM. 500 RPM was not enough to produce films having 5% nanoclay content with smooth surface without defects.

The contents of the nanoclay added films produced are given in Table 4.2. Their mechanical and physical properties were measured.

For tensile tests, "ASTM D 882-02 Standard Test Method for Tensile Properties of Thin Plastic Sheeting" was used. The nominal width of the specimens was 25.4 mm. The grip separation (gauge length) was 50 mm; the test specimens were 50 mm longer than the grip separation. The rate of grip separation (cross head speed) was 500 mm/min. Five specimens were tested from each sample for the tensile tests [14]. Instron 5565 universal testing machine is shown in Figure 4.9 during a tensile test.

Table 4.2 Nanoclay added films and their contents

	Compatibilizer (%)	Nanoclay (%)	Compatibilizer (g)	Nanoclay (g)	PP (g)	Mixture (g)
Film 1	10%	1%	100	10	890	1000
Film 2	10%	3%	100	30	870	1000
Film 3	10%	5%	100	50	850	1000
Film 4	15%	1%	150	10	840	1000
Film 5	15%	3%	150	30	820	1000
Film 6	15%	5%	150	50	800	1000
Film 7	20%	1%	200	10	790	1000
Film 8	20%	3%	200	30	770	1000
Film 9	20%	5%	200	50	750	1000

For tear tests, "ASTM D 1938-06 Standard Test Method for Tear-Propagation Resistance (Trouser Tear) of Plastic Film and Thin Sheeting by a Single-Tear Method" was used. The nominal width of the specimens was 25.4 mm; the length of the test specimens was 80 mm. The grip separation (gauge length) was 50 mm. The rate of grip separation was 250 mm/min. Five specimens were tested from each sample for the tear tests [15]. Instron 5565 universal machine is shown in Figure 4.10 during a tear test.

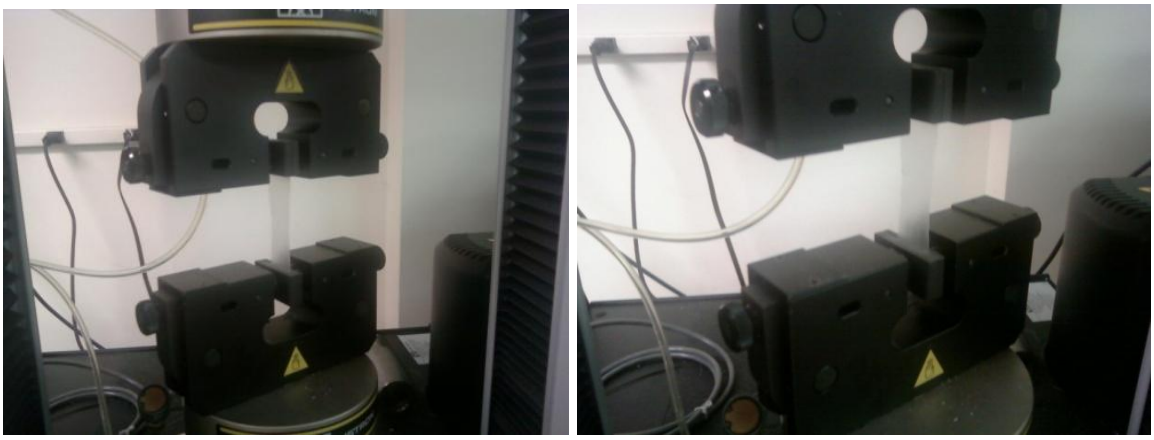

Figure 4.9 Tensile testing of the films

Figure 4.10 Tear testing of the films

For burst strength tests, "ASTM D 6797-02 Standard Test Method for Bursting Strength of Fabrics Constant-Rate-of-Extension (CRE) Ball Burst Test" was used. The specimens have the dimensions of 125 x 125 mm. The CRE machine was started with a speed of 305 mm/min. and the speed was kept constant till the specimens bursted. Five specimens were tested from each sample for the burst tests [16]. Instron 5565 universal machine is shown in Figure 4.11 during a burst strength test.

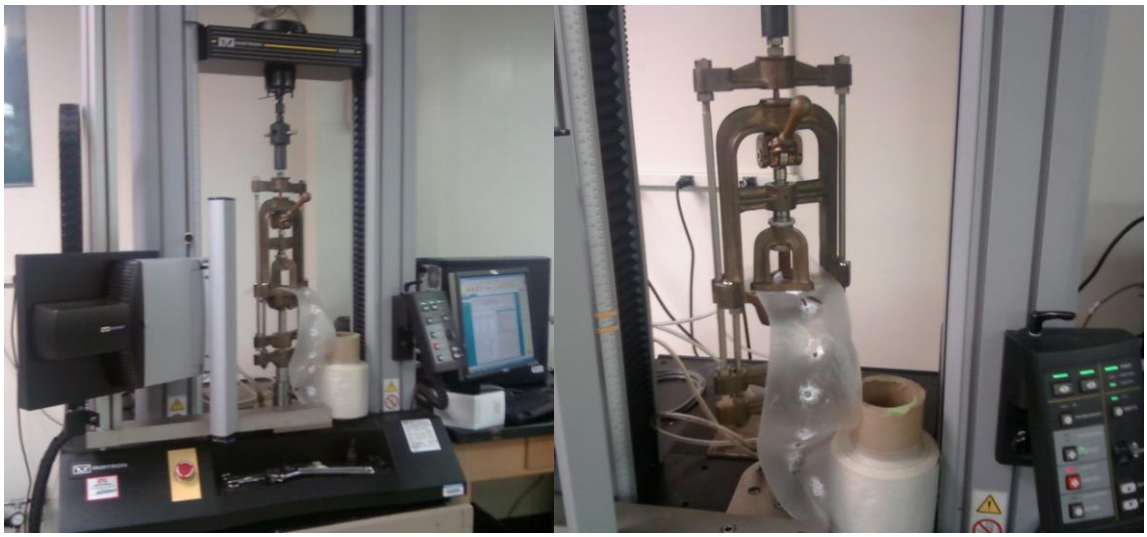

Figure 4.11 Instron 5565 universal machine performing burst strength test

For thickness tests, 5 measurements were taken from each sample and the average was used. Table 4.3 shows the thickness of the nanoclay reinforced films. These thickness results were used in order to calculate tensile strength.

Table 4.3 Thickness of the nanoclay reinforced films

Film #	Film 1	Film 2	Film 3	Film 4	Film 5	Film 6	Film 7	Film 8	Film 9
Thickness (mm)	0.128	0.130	0.162	0.092	0.138	0.162	0.114	0.142	0.20

4.3. Results and Discussion

4.3.1. Morphology Analysis

As it is seen from Figure 4.12 and 4.13, Film 1 has more homogeneous nanoclay dispersion since it has only 1% nanoclay content. Film 2 has bigger nanoclay particles since it has lower nanoclay dispersion due to 3% nanoclay content.

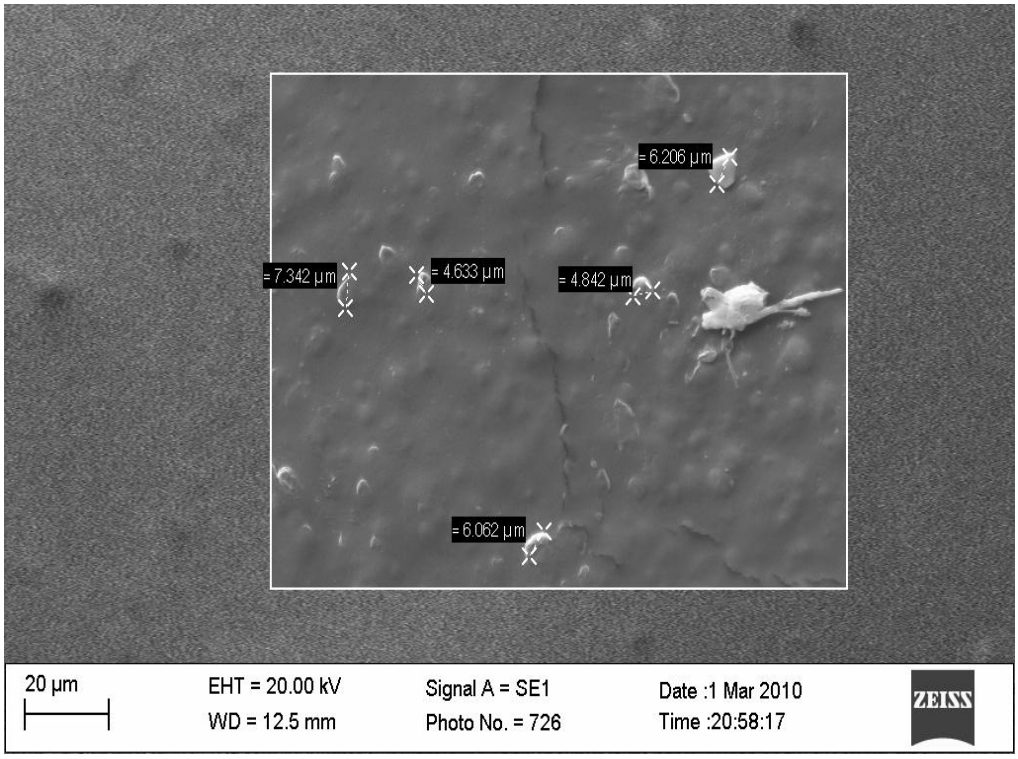

Figure 4.12 Nanoclay dispersion in Film 1

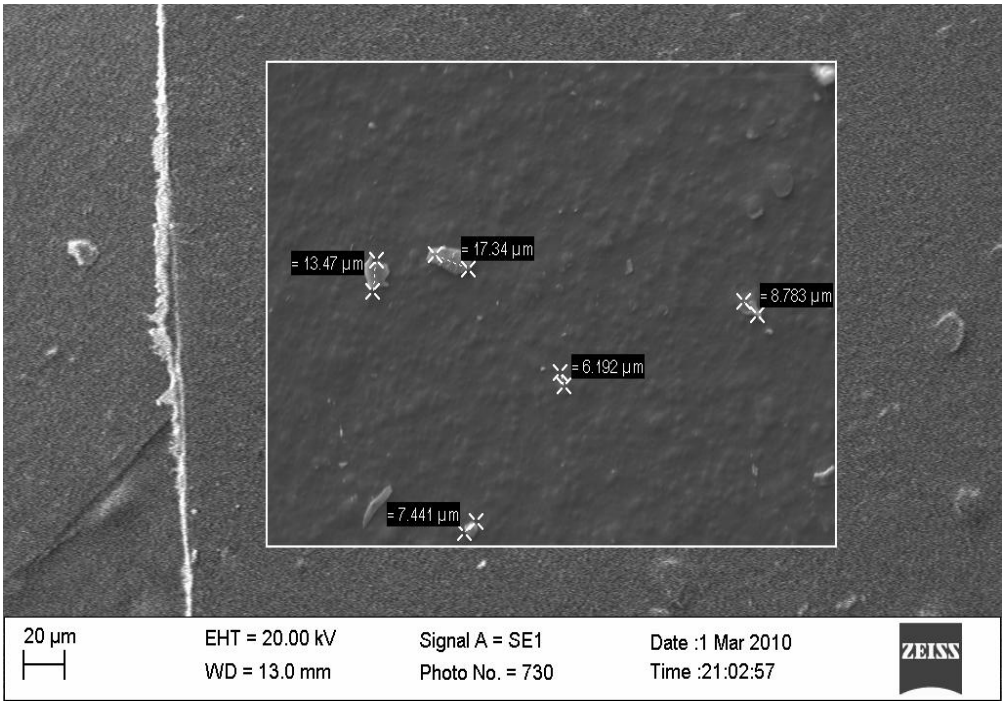

Figure 4.13 Nanoclay dispersion in Film 2

Although Film 3 has the highest nanoclay content (5%) as compared with Film 1 and Film 2, it has better nanoclay dispersion and has smaller nanoclay particles in its structure compared to Film 2 (Figure 3.36 and 3.37). Screw speed was increased for the films having 5% nanoclay content because the films could not be drawn with the same screw speed that was used for the films having 1% and 3% nanoclay content. Therefore, since the screw speed was increased, shear stress increased. This caused the polymer and nanoclay to mix more homogeneously, making the morphological structure of Film 3 more homogeneous.

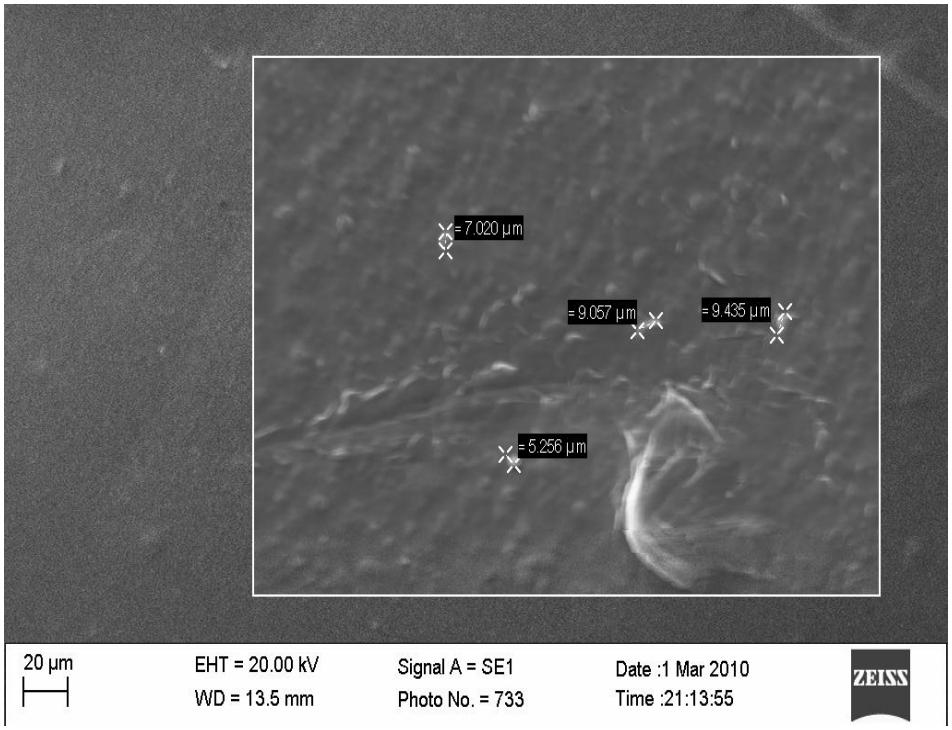

Figure 4.14 Nanoclay dispersion in Film 3

As it is seen from Figure 4.15 and 4.16, Film 4 has more homogeneous nanoclay dispersion since it has only 1% nanoclay content; Film 5 has bigger nanoclay particles in its structure since it has lower nanoclay dispersion due to 3% nanoclay content.

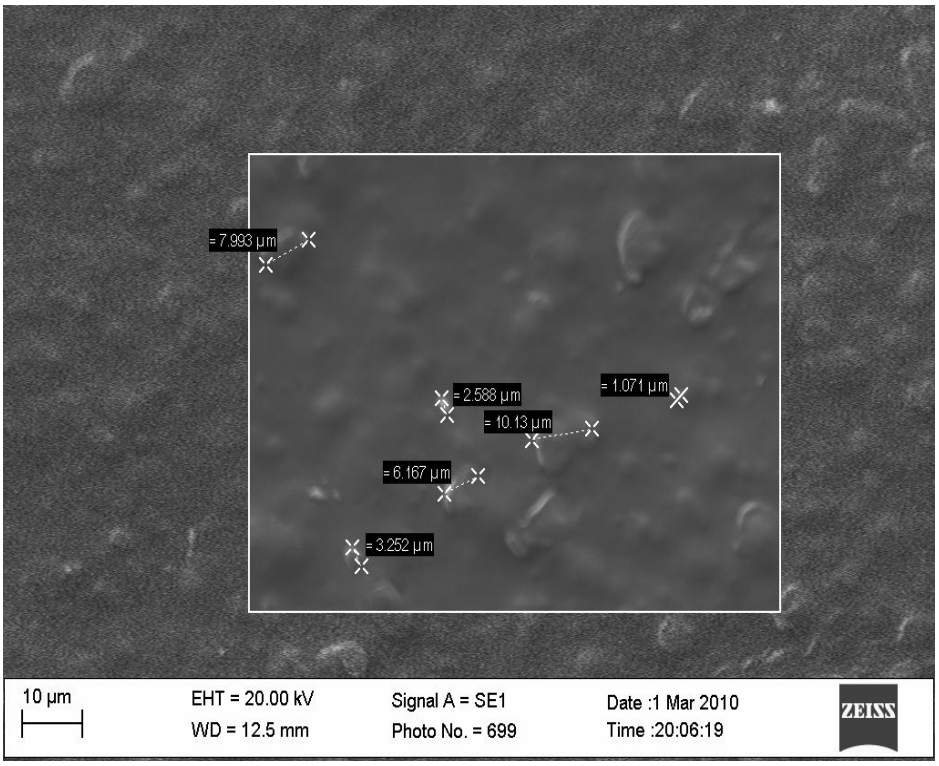

Figure 4.15 Nanoclay dispersion in Film 4

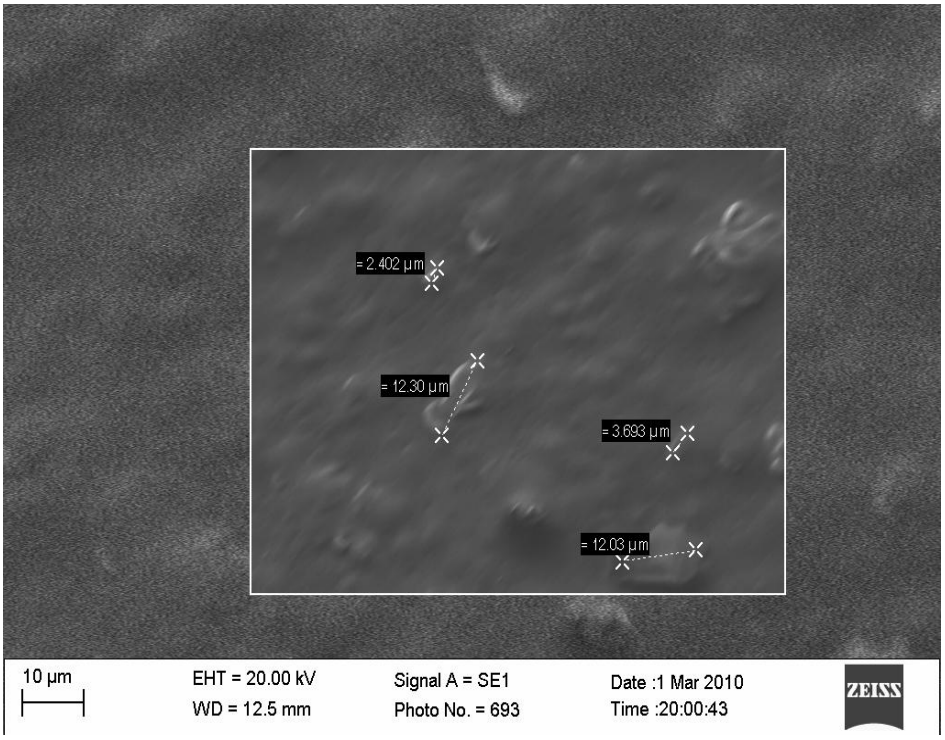

Figure 4.16 Nanoclay dispersion in Film 5

Although Film 6 has the highest nanoclay content (5%) as compared with Film 4 and Film 5, it has better nanoclay dispersion and has smaller nanoclay particles in its structure compared to Film 5 (Figure 4.16 and 4.17). Screw speed was increased for the films having 5% nanoclay content, which increased shear stress. This caused the polymer and nanoclay to mix more homogeneously, making the morphological structure of Film 6 more homogeneous.

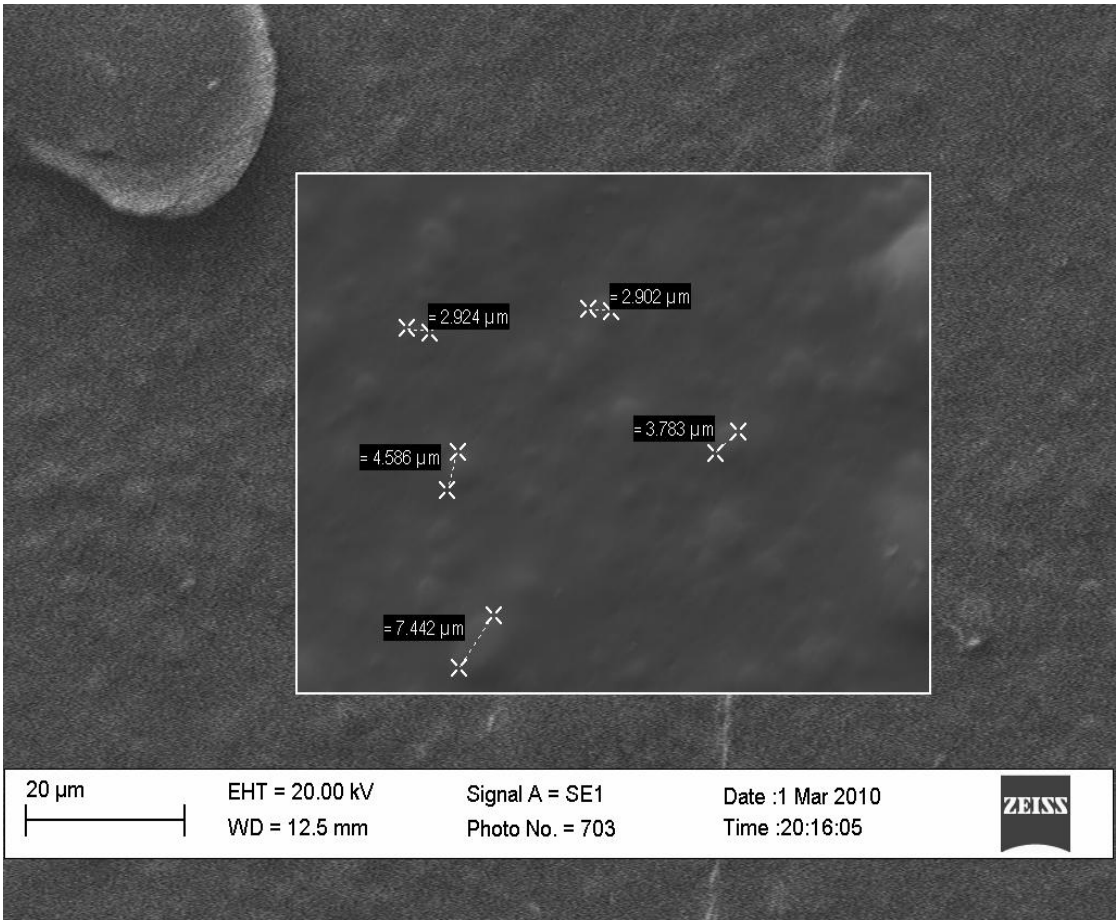

Figure 4.17 Nanoclay dispersion in Film 6

As it is seen from Figure 4.18 and 4.19, Film 7 has more homogeneous nanoclay dispersion since it has only 1% nanoclay content; Film 8 has bigger nanoclay particles in its structure since it has lower nanoclay dispersion due to 3% nanoclay content.

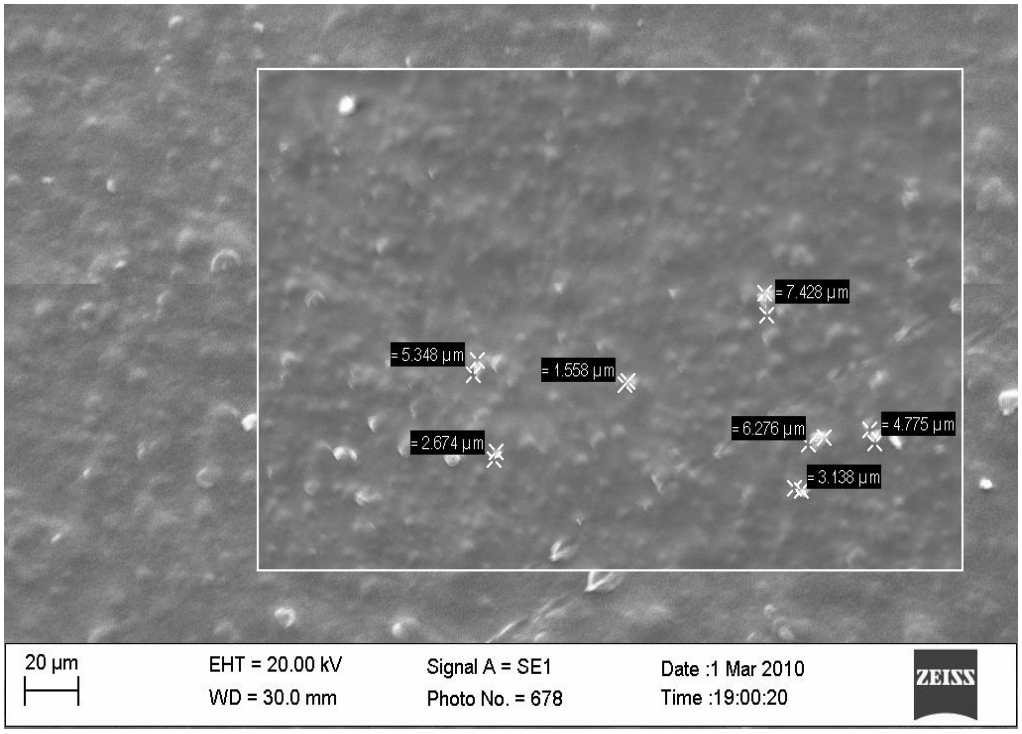

Figure 4.18 Nanoclay dispersion in Film 7

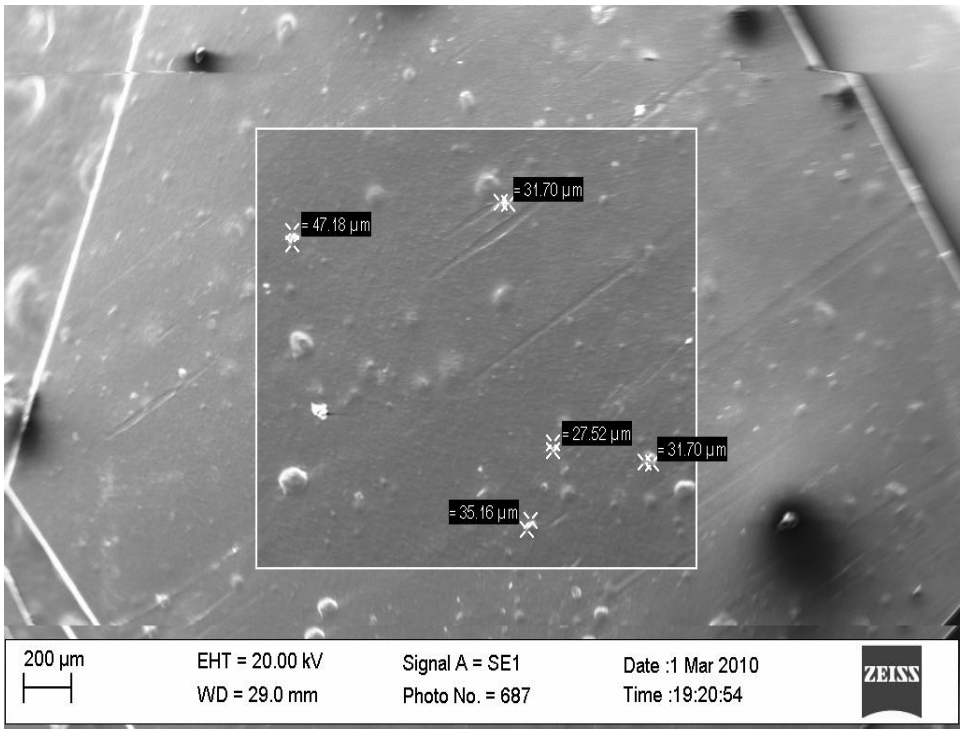

Figure 4.19 Nanoclay dispersion in Film 8

Although Film 9 has the highest nanoclay content (5%) as compared with Film 7 and Film 8, it has better nanoclay dispersion and has smaller nanoclay particles in its structure compared to Film 8 (Figure 4.19 and 4.20) due to increased screw speed.

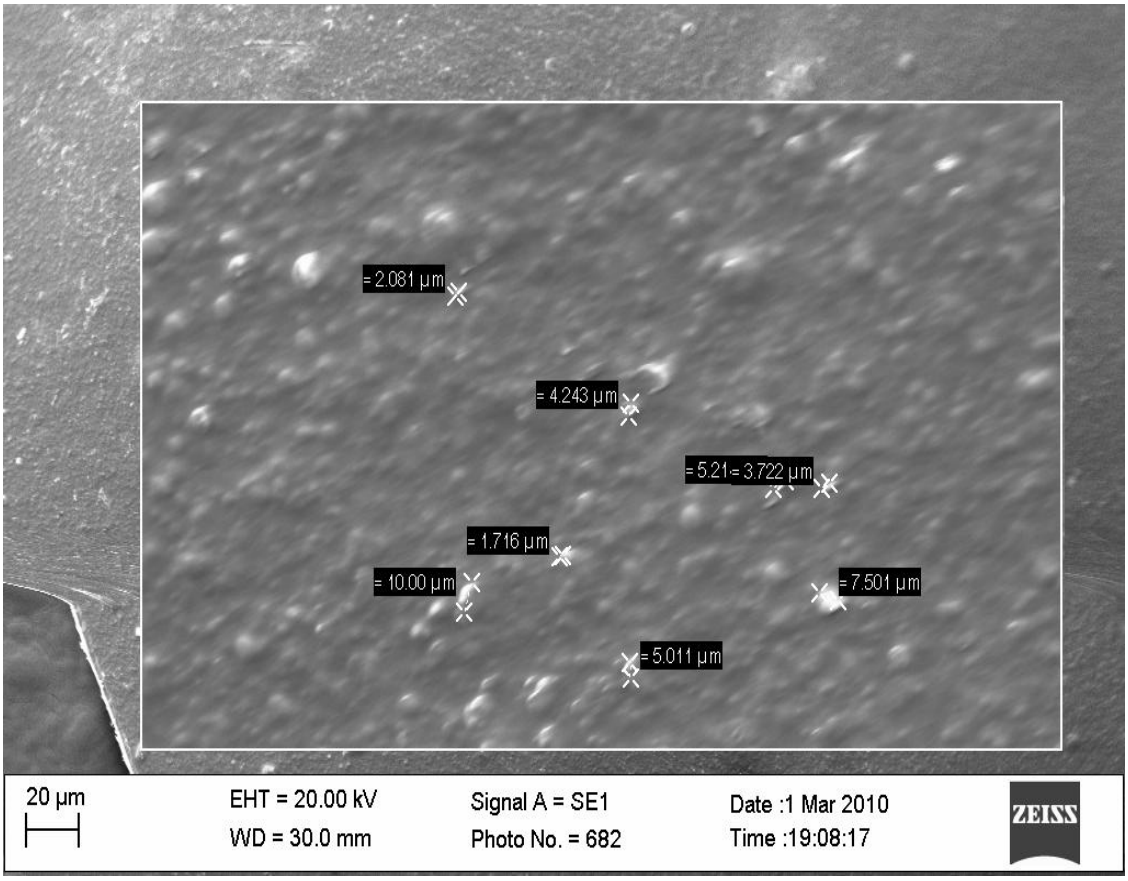

Figure 4.20 Nanoclay dispersion in Film 9

If the films 1, 4, 7 having 1% nanoclay content, films 2, 5, 8 having 3% nanoclay content and films 3, 6, 9 having 5% nanoclay content are compared according to the increasing compatibilizer content from 10% to 20%, it could be seen that no conclusion can be drawn from the morphology analysis about the effect of compatibilizer content increase on the nanoclay dispersion and the homogeneity of the morphological structure of the films.

4.3.2. DSC Analysis

Film 1, Film 2 and Film 3 have nanoclay contents of 1%, 3% and 5%, respectively. From Figures 4.21, 4.22 and 4.23 it can be seen that the melting points of films 1, 2 and 3 slightly increase as the nanoclay content increases.

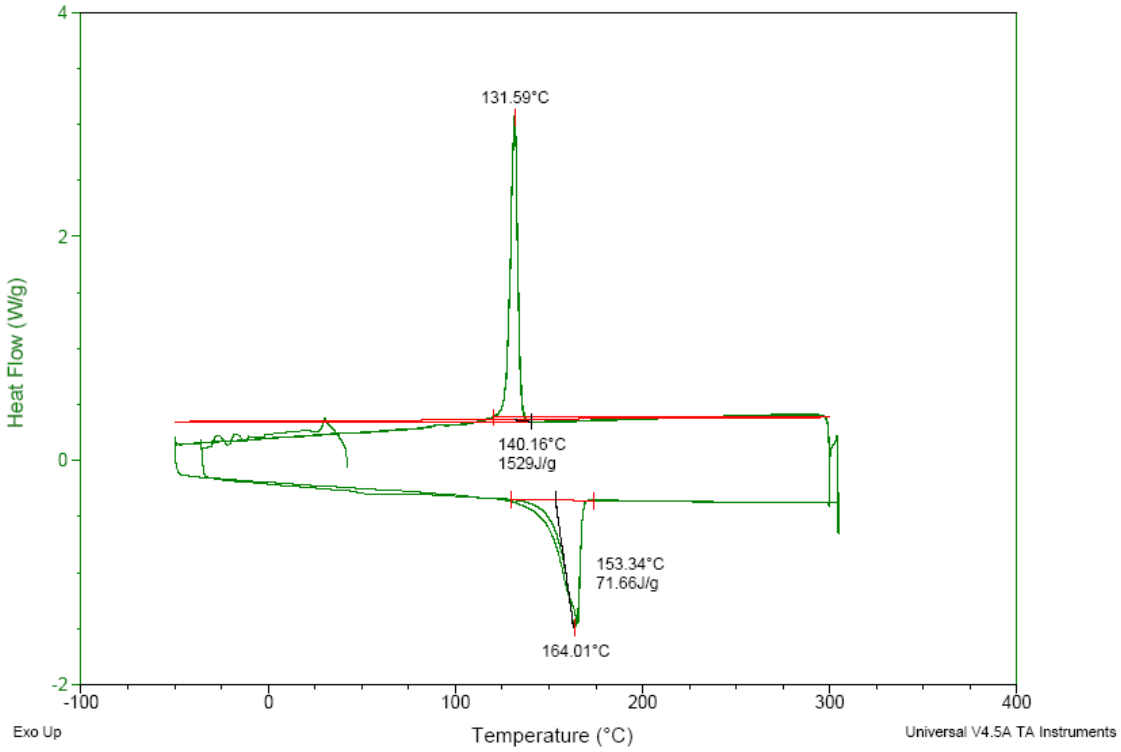

Figure 4.21 DSC graph of Film 1

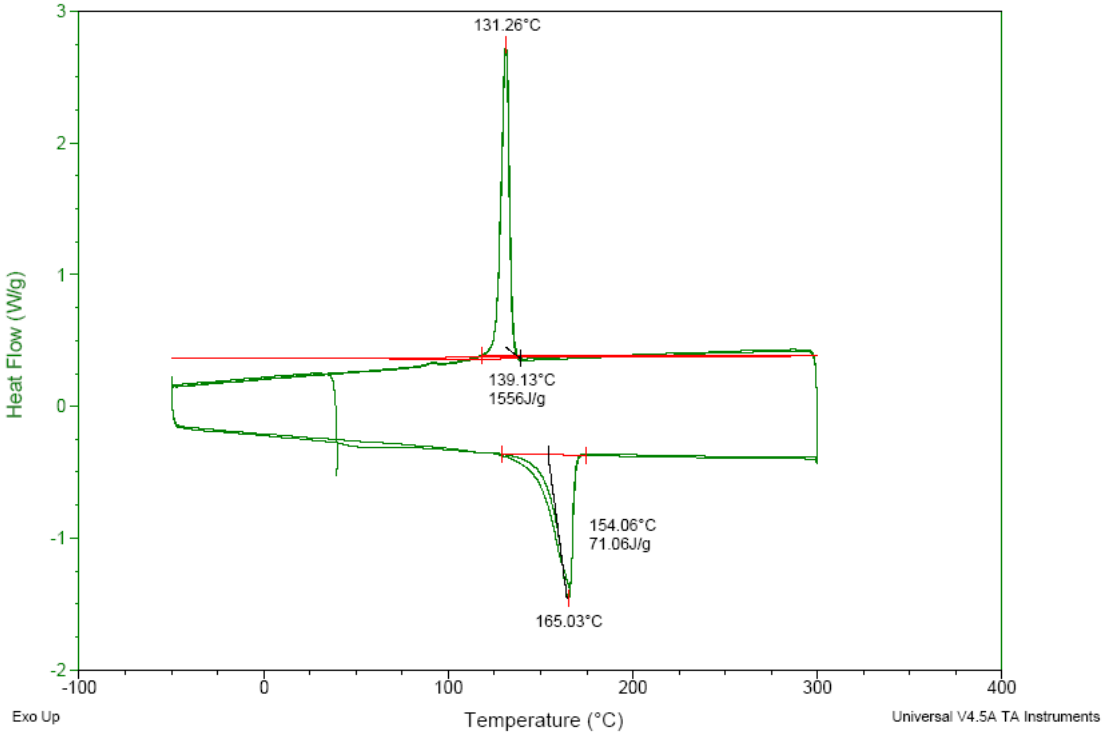

Figure 4.22 DSC graph of Film 2

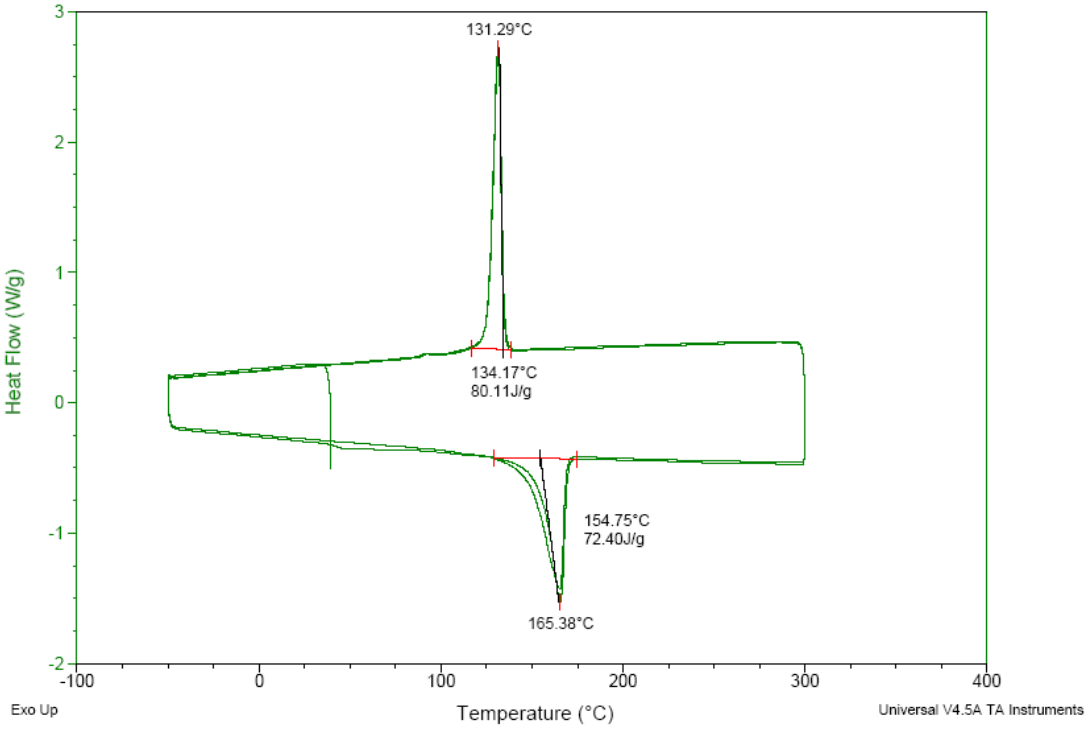

Figure 4.23 DSC graph of Film 3

Film 4, Film 5 and Film 6 have nanoclay contents of 1%, 3% and 5%, respectively. From Figures 4.24, 4.25 and 4.26 it can be seen that the melting points of films 4, 5 and 6 slightly increase as the nanoclay content increases.

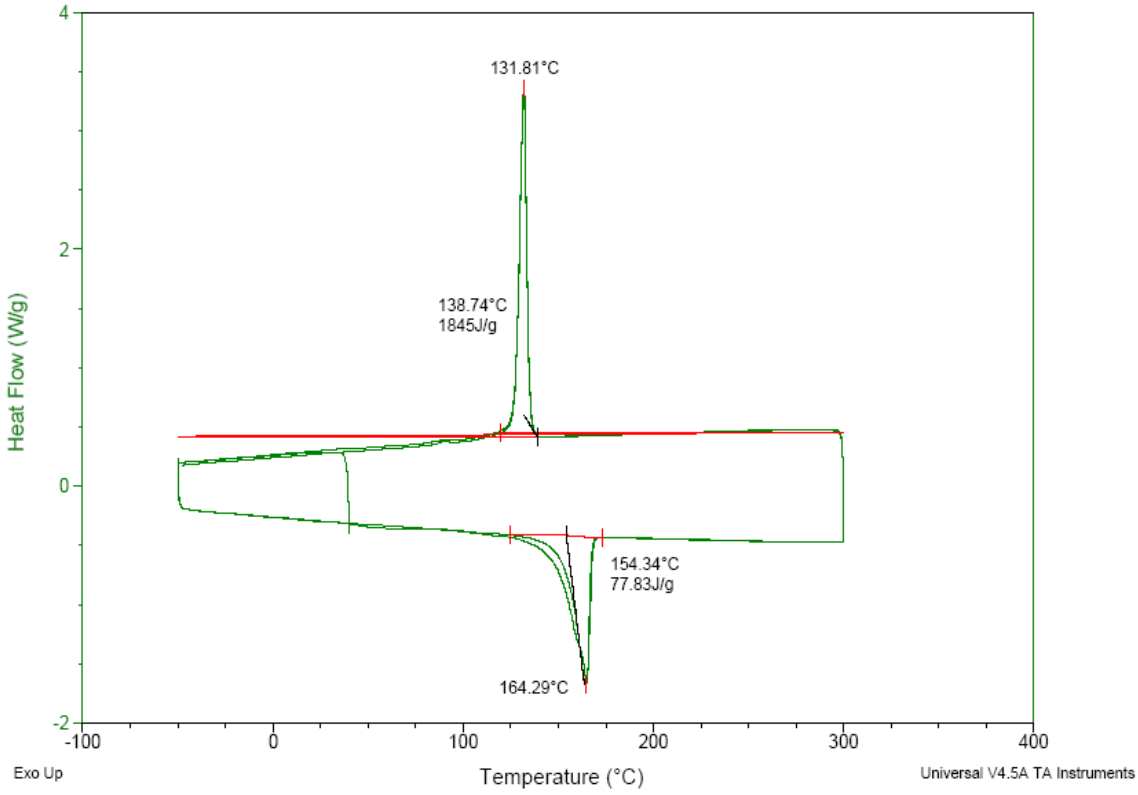

Figure 4.24 DSC graph of Film 4

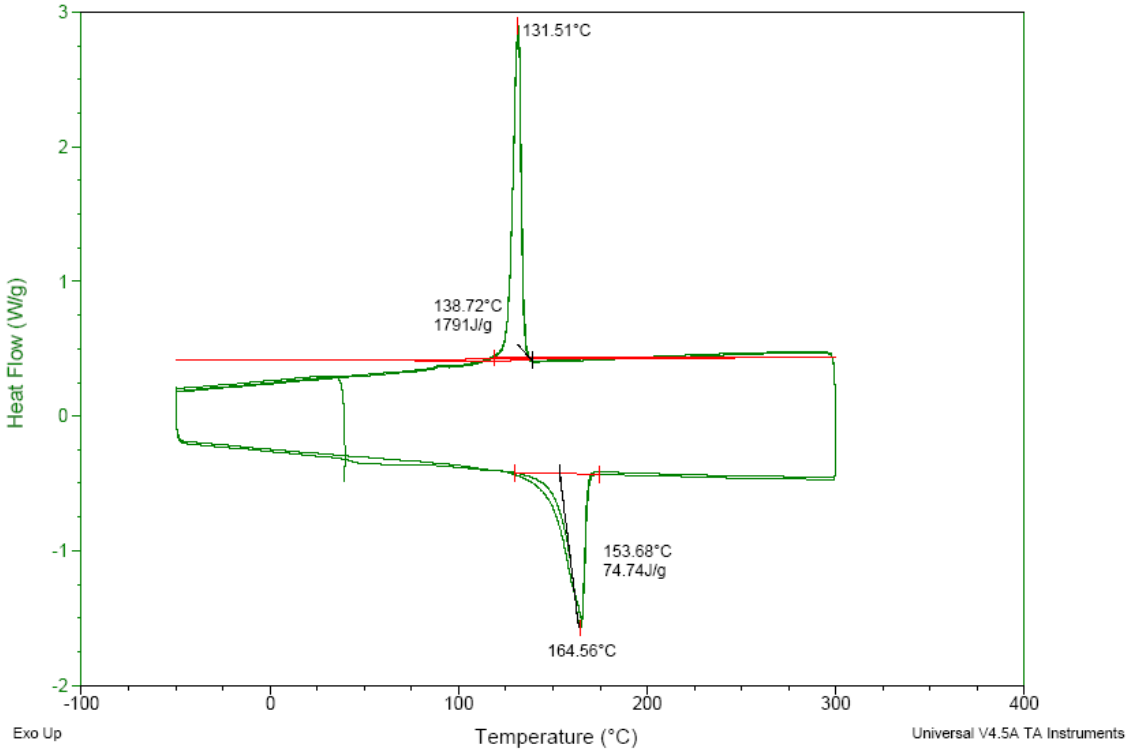

Figure 4.25 DSC graph of Film 5

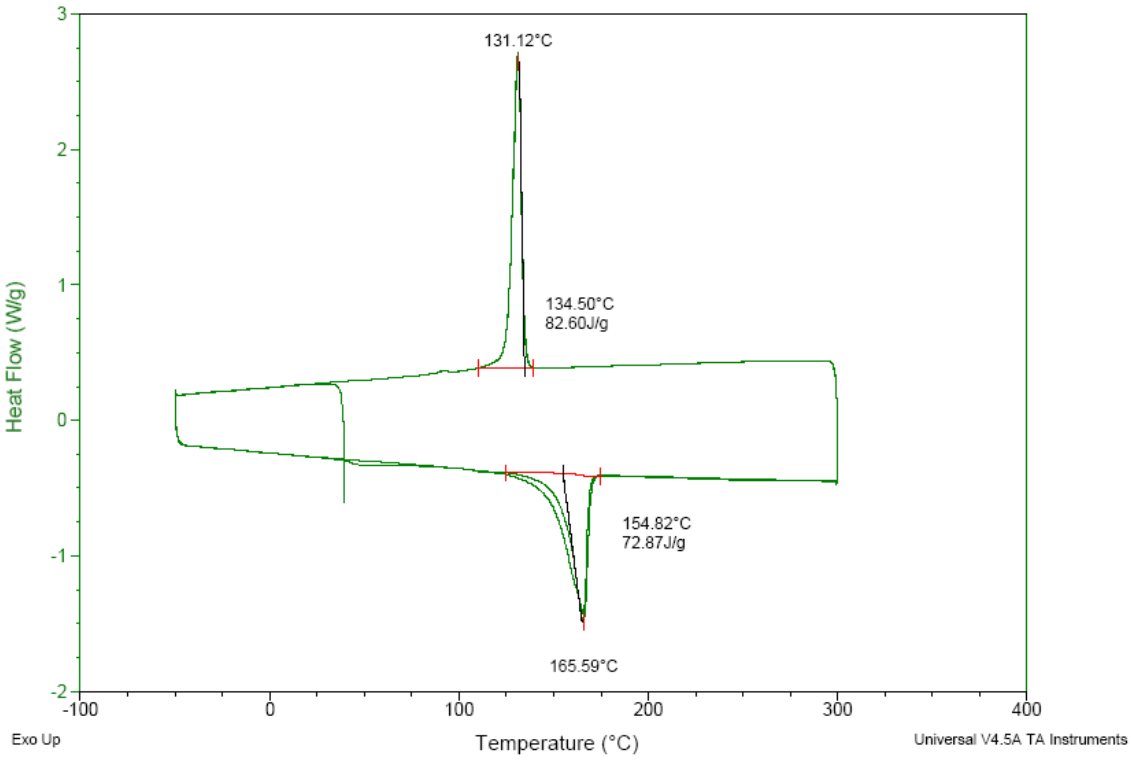

Figure 4.26 DSC graph of Film 6

Film 7, Film 8 and Film 9 have nanoclay contents of 1%, 3% and 5%, respectively. From Figures 4.27, 4.28 and 4.29 it can be seen that the melting points of films 7, 8 and 9 slightly increase as the nanoclay content increases.

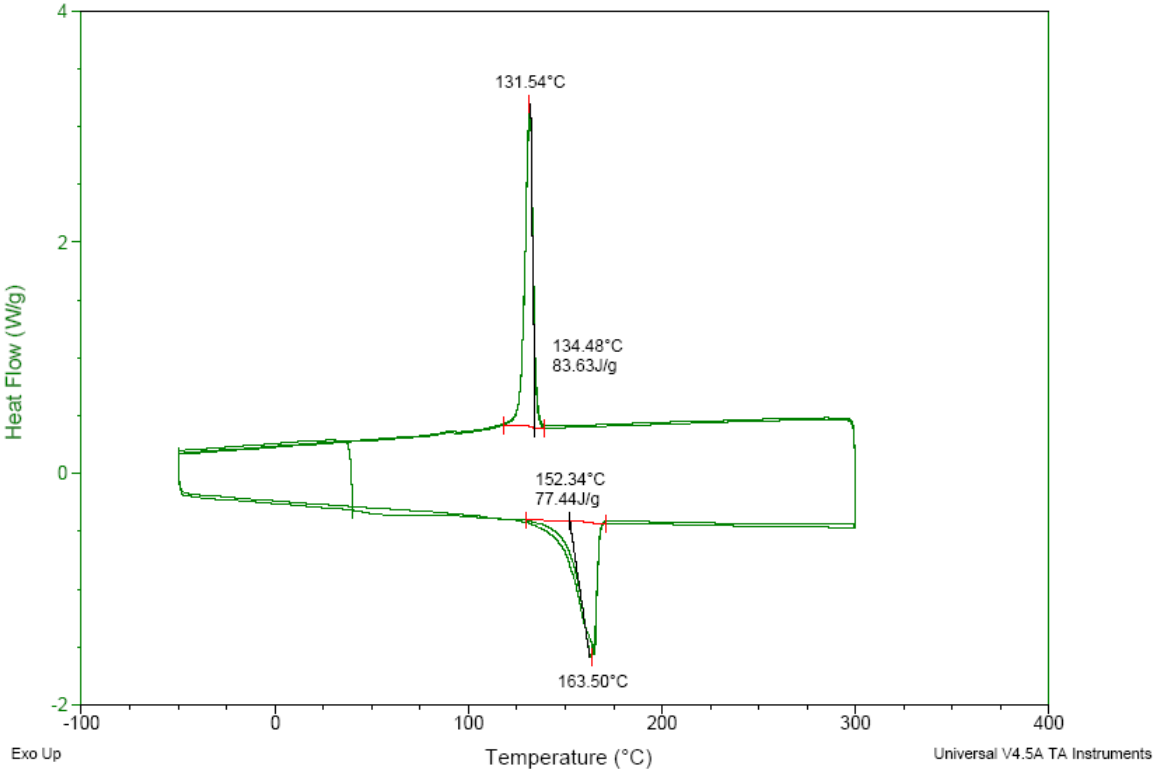

Figure 4.27 DSC graph of Film 7

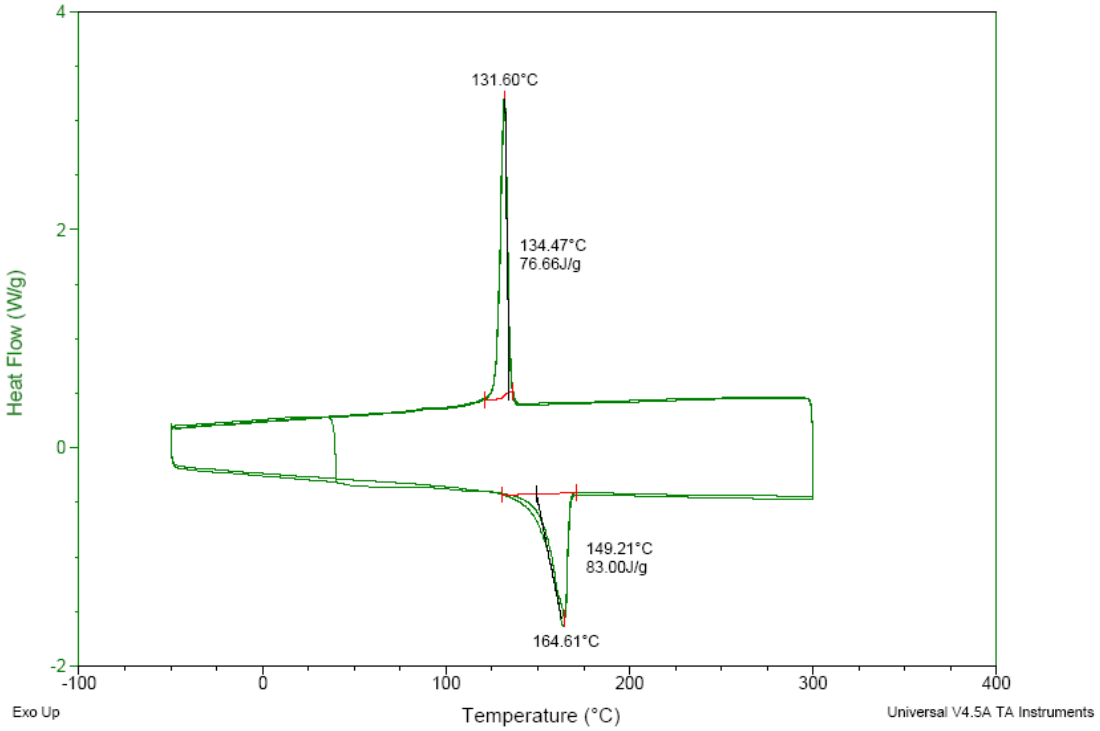

Figure 4.28 DSC graph of Film 8

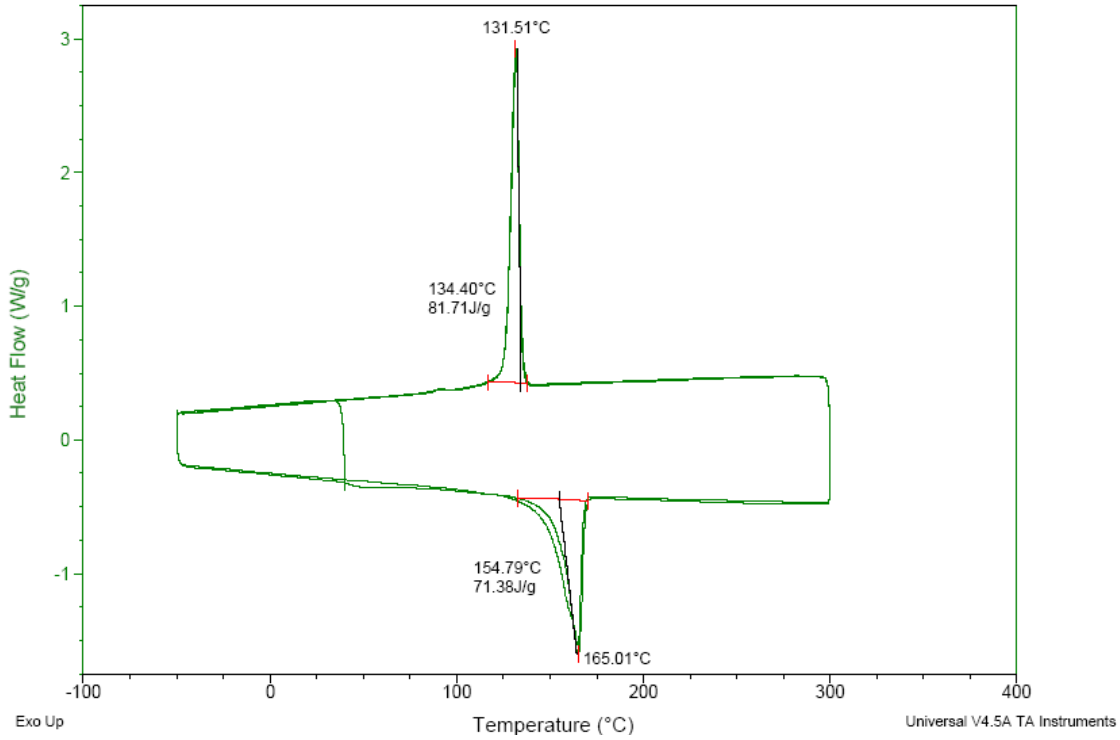

Figure 4.29 DSC graph of Film 9

4.3.3. Tensile Strength Analysis

Tensile strength analysis was done to examine the effect of nanoclay and compatibilizer content of nanoclay reinforced PP films. The tensile strength of the films is shown in Table 4.4.

Table 4.4 Tensile stress values

FILM #	TENSILE STRESS (MPa)					
	SAMPLE 1	SAMPLE 2	SAMPLE 3	SAMPLE 4	SAMPLE 5	AVERAGE
Film 1	6.89	7.55	6.99	5.38	8.47	7.056
Film 2	4.32	4.7	5.48	5.64	5.46	5.12
Film 3	6	6.97	7.08	7.43	6.7	6.836
Film 4	6.7	7.55	6.84	6.69	5.9	6.736
Film 5	4.56	4.65	4.47	4.96	4.46	4.62
Film 6	9.45	9.37	9.53	8.44	9.42	9.242
Film 7	5.03	5.71	6.11	7.59	7.84	6.456
Film 8	4.87	4.43	4.91	4.62	4.89	4.744
Film 9	6.06	5.97	5.75	5.94	5.89	5.922

Evaluation According to Nanoclay Content:

- Condition of 10 wt % Compatibilizer Presence

Tensile test results for Film 1, Film 2 and Film 3 are shown in Figure 4.30. Film 1 includes 1%, Film 2 includes 3% and Film 3 includes 5% nanoclay.

In Figure 4.30, the strain value of Film 1 is nearly 560%. However, the strain values of Film 2 is 420% and the strain values of Film 3 is 60% (Figure 4.30). This shows that as the nanoclay content of the films, having 10% compatibilizer content, increases, the extension of the films decreases.

As it is seen from Table 4.4, maximum tensile stress for films 1, 2 and 3 decreases first then increases as the nanoclay content increases from 1% to 5%. The increase in nanoclay content reduces the tensile strength. As explained earlier, nanoclay dispersion in Film 1 is better than nanoclay dispersion in Film 2. However, for Film 3, having the highest nanoclay content the screw speed was increased, resulting in higher tensile strength. It can be seen from morphology analysis that Film 3 has more homogeneous structure than Film 2. As a result, the tensile strength of Film 2 (3% nanoclay content) decreased as compared with Film 1 (1% nanoclay content), however, the tensile strength of Film 3 (5% nanoclay content) increased although it has higher nanoclay content as compared with Film 2.

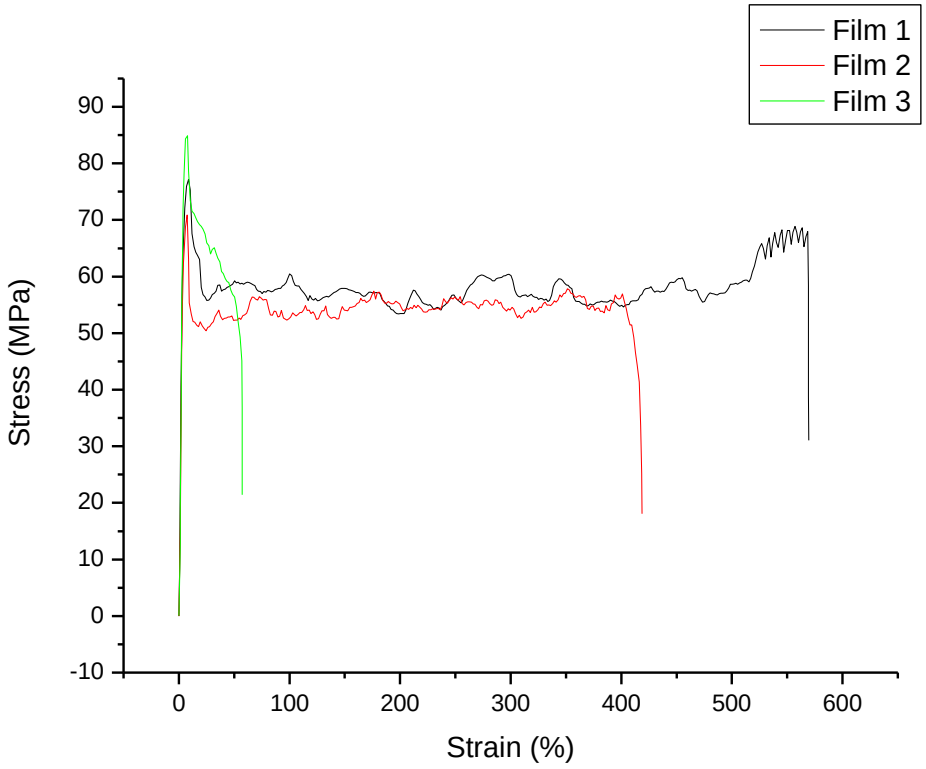

Figure 4.30 Tensile stress-strain curve of Film 1, Film 2 and Film 3

- Condition of 15 wt % Compatibilizer Presence

Tensile test results for Film 4, Film 5 and Film 6 are shown in Figure 4.31. Film 4 includes 1%, Film 5 includes 3% and Film 6 includes 5% nanoclay.

In Figure 4.31, the strain value of Film 4 is nearly 375%. However, the strain value of Film 5 is nearly 125% and the strain value of Film 6 is nearly 25%. This shows that as the nanoclay content of the films, having 15% compatibilizer content, increases, the extension of the films decreases.

As it is seen from Table 4.4, maximum tensile stress for films 4, 5 and 6 decreases first then increases as the nanoclay content increases from 1% to 5%. The increase in nanoclay

content reduces the tensile strength. The results are similar to those with 10 wt% compatibilizer. As explained earlier, nanoclay dispersion in Film 4 is better than nanoclay dispersion in Film 5. However, for Film 6, having the highest nanoclay content the screw speed was increased, resulting in higher tensile strength. It can be seen from morphology analysis that Film 6 has more homogeneous structure than Film 5. As a result, the tensile strength of Film 5 (3% nanoclay content) decreased as compared with Film 4 (1% nanoclay content), however, the tensile strength of Film 6 (5% nanoclay content) increased although it has higher nanoclay content as compared with Film 5.

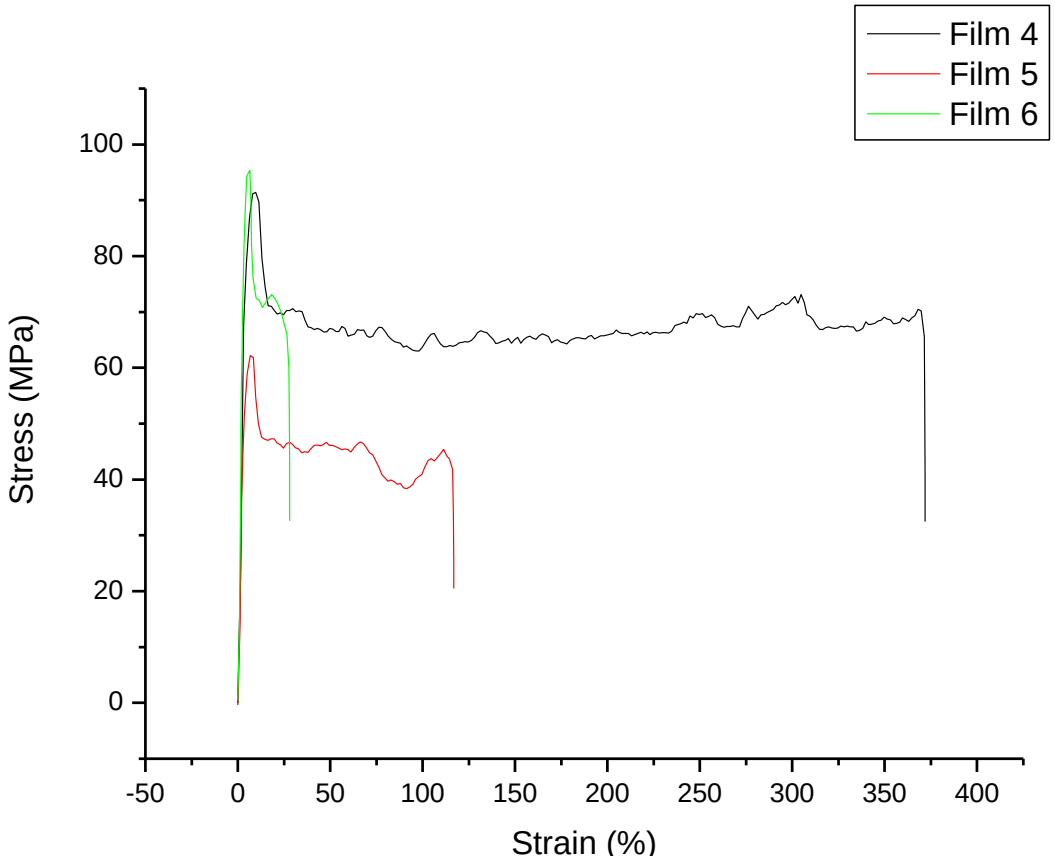

Figure 4.31 Tensile stress-strain curve of Film 4, Film 5 and Film 6

- Condition of 20 wt % Compatibilizer Presence

Tensile test results for Film 7, Film 8 and Film 9 are shown in 4.32. Film 7 includes 1%, Film 8 includes 3% and Film 9 includes 5% nanoclay.

In Figure 4.32, the strain value of Film 7 is nearly 500%. However, the strain value of Film 8 is nearly 220% and the strain value of Film 9 is nearly 25%. This shows that as the nanoclay content of the films, having 20% compatibilizer content, increases, the extension of the films decreases.

As it is seen from Table 4.4, maximum tensile stress for films 7, 8 and 9 decreases first then increases as the nanoclay content increases from 1% to 5%. The increase in nanoclay content reduces the tensile strength. The results are similar to those with 10 wt% and 15 wt% compatibilizer. As explained earlier, nanoclay dispersion in Film 7 is better than nanoclay dispersion in Film 8. However, for Film 9, having the highest nanoclay content the screw speed was increased, resulting in higher tensile strength. It can be seen from morphology analysis that Film 9 has more homogeneous structure than Film 6. As a result, the tensile strength of Film 7 (3% nanoclay content) decreased as compared with Film 8 (1% nanoclay content), however, the tensile strength of Film 9 (5% nanoclay content) increased although it has higher nanoclay content as compared with Film 8.

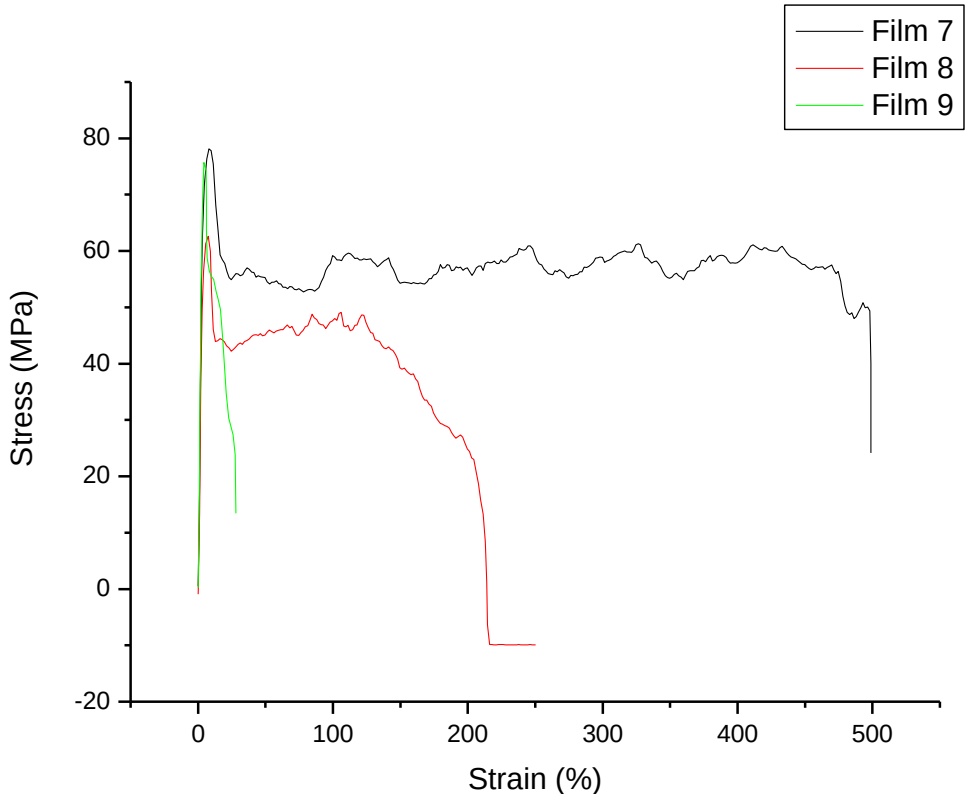

Figure 4.32 Tensile stress-strain curve of Film 7, Film 8 and Film 9

Evaluation According to Compatibilizer Content:

- *Condition of 1 wt % Nanoclay Presence*

Film 1 includes 10%, Film 4 includes 15% and Film 7 includes 20% compatibilizer.

As seen from Figure 4.30, the strain value of Film 1 is 550%. However, the strain values of Film 4 is 375% and the strain values of Film 7 is 500% (Figure 4.31 and 4.32). The compatibilizer content of the nanoclay reinforced films, having 1% nanoclay content, increases, the strain of the films decreases first then increases.

As it is seen from Table 4.4, tensile stress for films 1, 4 and 7 decreases, as the compatibilizer content increases from 10% to 20%.

- *Condition of 3 wt % Nanoclay Presence*

Film 2 includes 10%, Film 5 includes 15% and Film 8 includes 20% compatibilizer.

From Figure 4.30, the strain value of Film 2 is 420%. However, the strain value of Film 5 is 120% and the strain value of Film 8 is 220% (Figure 4.31 and 4.32). As the compatibilizer content of the nanoclay reinforced films, having 3% nanoclay content, increases, the strain of the films decreases first then increases.

As it is seen from Table 4.4, tensile stress for films 2, 5 and 8 firstly decreases, then increases as the compatibilizer content increases from 10% to 20%. For Film 5 (15% compatibilizer content) the tensile strength decreased as compared with Film 2 (10% compatibilizer content), but for Film 8 (20% compatibilizer content) the tensile strength increased as compared with Film 5.

- *Condition of 5 wt % Nanoclay Presence*

Film 3 includes 10%, Film 6 includes 15% and Film 9 includes 20% compatibilizer.

As seen from Figure 4.30, the strain value of Film 3 is 50%. However, the strain value of Film 6 is 25% and the strain value of Film 9 is 25% (Figure 4.31 and 4.32). As the compatibilizer content of the nanoclay reinforced films, having 5% nanoclay content, increases, the strain of Film 6 and Film 9 decreases nearly to the same values.

As it is seen from Table 4.4, tensile stress for films 3, 6 and 9 firstly increases then decreases as the compatibilizer content increases from 10% to 20%. For Film 6 (15% compatibilizer content) the tensile strength increased as compared with Film 3 (10% compatibilizer content), but for Film 9 (20% compatibilizer content) the tensile strength decreased as compared with Film 6.

If all of these results considering the evaluation of compatibilizer content change are examined, no specific conclusion can be drawn about the effect of compatibilizer content on tensile strength of the films.

4.3.4. Tear Strength Analysis

Tear strength analysis was done based on nanoclay and compatibilizer content of the reinforced PP films.

To compare the tear strength of the films, the area under the load-extension curve was determined and this value was divided by the extension value. Calculated tear strength values can be seen in Table 4.5. The tear load (N) was used to compare the tear strength of the nanoclay reinforced PP films.

Table 4.5 Calculated tear strength values

FILM #		SAMPLE 1	SAMPLE 2	SAMPLE 3	SAMPLE 4	SAMPLE 5	AVERAGE
Film 1	Area (Nmm)	43.94985	51.80483	43.06312	46.73279	49.26152	
	Extension (mm)	61.26669	71.98334	53.38326	61.41662	58.4834	
	Tear (N)	0.717353	0.719678	0.806678	0.760914	0.842316	0.769388
Film 2	Area (Nmm)	45.48238	50.08909	43.09892	43.10592	43.02687	
	Extension (mm)	72.02501	66.0332	64.04986	57.83327	64.20817	
	Tear (N)	0.63148	0.758544	0.672896	0.745348	0.670115	0.695677
Film 3	Area (Nmm)	62.63299	45.72679	53.51617	68.26655	45.18898	
	Extension (mm)	63.04992	49.28306	55.81651	62.40853	56.37492	
	Tear (N)	0.993387	0.92784	0.958787	1.093866	0.801579	0.955092
Film 4	Area (Nmm)	43.66039	40.15241	35.75421	37.94295	37.27858	
	Extension (mm)	72.28343	63.52534	65.3251	62.19165	61.69145	
	Tear (N)	0.604017	0.632069	0.547327	0.610097	0.604275	0.599557
Film 5	Area (Nmm)	41.15258	32.33616	42.86967	40.48964	48.41843	
	Extension (mm)	60.25837	64.10818	65.3251	73.03321	67.66686	
	Tear (N)	0.682935	0.5044	0.656251	0.5544	0.715541	0.622706
Film 6	Area (Nmm)	61.36684	52.12976	45.33582	63.19742	58.0279	
	Extension (mm)	73.16661	56.44162	46.20817	65.35012	59.42502	
	Tear (N)	0.838727	0.923605	0.981121	0.967059	0.976489	0.9374
Film 7	Area (Nmm)	75.60466	62.22934	74.50421	76.11081	64.46762	
	Extension (mm)	71.44169	68.50009	72.09998	73.61652	64.17499	

	Tear (N)	1.058271	0.908456	1.033346	1.033882	1.00456	1.007703
Film 8	Area (Nmm)	46.81317	50.85026	53.44458	58.28861	49.8039	
	Extension (mm)	66.01655	58.60016	72.55827	72.43325	75.13343	
	Tear (N)	0.709113	0.86775	0.736575	0.804722	0.662873	0.756206
Film 9	Area (Nmm)	43.94985	51.80483	43.06312	46.73279	49.26152	
	Extension (mm)	61.26669	71.98334	53.38326	61.41662	58.4834	
	Tear (N)	0.717353	0.719678	0.806678	0.760914	0.842316	0.769388

Evaluation According to Nanoclay Content:

- Condition of 10 wt % Compatibilizer Presence

Tear test results for Film 1, Film 2 and Film 3 can be seen in Figure 4.33. Film 1 includes 1%, Film 2 includes 3% and Film 3 includes 5% nanoclay.

As it is seen from Table 4.5, tear strength of films 1, 2 and 3 decreases first, then increases as the nanoclay content increases from 1% to 5%. The increase in nanoclay content reduces the tear strength since nanoclay dispersion cannot be achieved as good as in the films having lower nanoclay content. Besides, as it can be seen from morphology analysis nanoclay dispersion in Film 1 is better than Film 2. Therefore, for Film 1, the more evenly dispersed nanoparticles resist tearing force (load) making the tear strength higher. However, when Film 2 is tried to be torn, since the nanoclay dispersion is not as good as Film 1 and nanoclay particles are not evenly dispersed in the structure to resist the tearing force, it is seen that tear strength decreases compared to Film 1. For Film 3, having the highest nanoclay content, the situation is different. Since for 5% nanoclay content, the films could not be drawn with the same screw

speed that was used for the films having 1% and 3% nanoclay content, screw speed was increased. Since the screw speed was increased, shear stress increased. Increase in the shear stress made the polymer and nanoclay mix more homogeneously by making the films, having 5% nanoclay content, gain higher tear strength. Better nanoclay dispersion in Film 3 can be seen from SEM micrographs of morphology analysis. Because of this, for Film 2 (3% nanoclay content) the tear strength decreased as compared with Film 1 (1% nanoclay content), but for Film 3 (5% nanoclay content) the tear strength increased although it has higher nanoclay content as compared with Film 2.

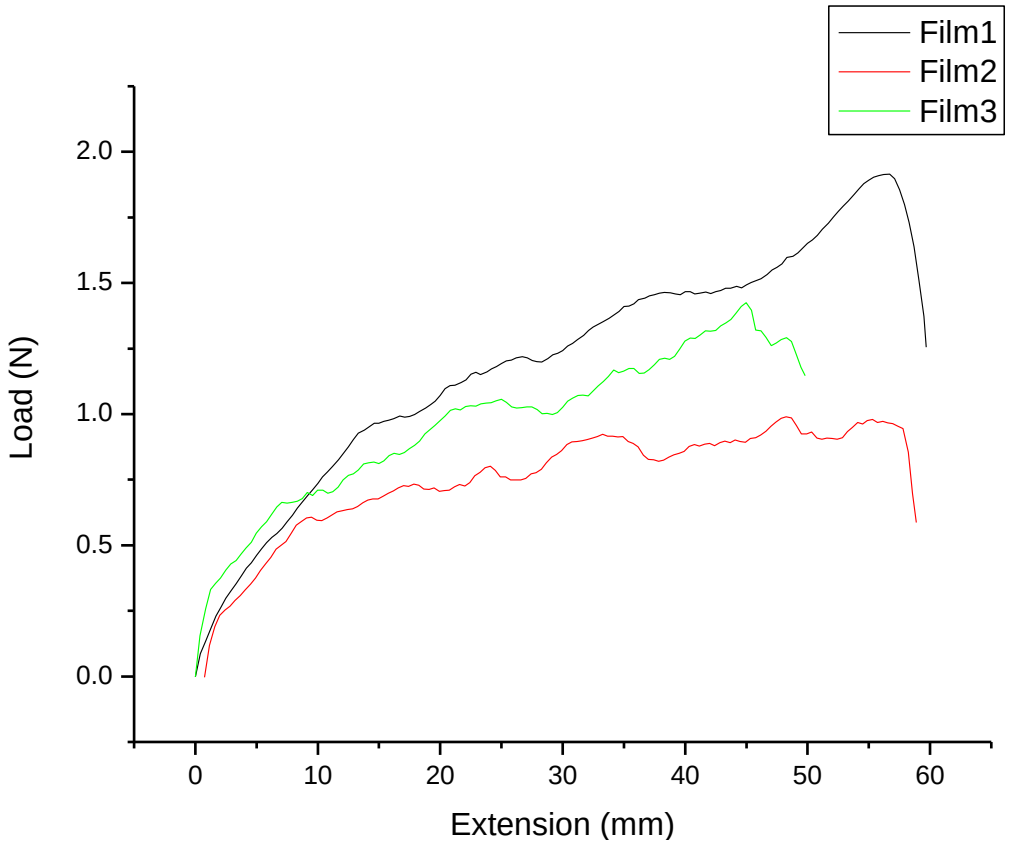

Figure 4.33 Tear load-extension curve of Film 1, Film2 and Film 3

- Condition of 15 wt % Compatibilizer Presence

Tear test results for Film 4, Film 5 and Film 6 are shown in Figure 4.34. Film 4 includes 1%, Film 5 includes 3% and Film 6 includes 5% nanoclay content.

As it is seen from Table 4.5, tear strength for films 4, 5 and 6 increases as the nanoclay content increases from 1% to 5%. Since the difference of nanoclay dispersion is not much different in Film 4 and 5 according to SEM micrographs of morphology analysis, this small difference is thought to have little effect on tear strength of the films 4 and 5. For Film 6 (5% nanoclay content); since the screw speed was increased, the tear strength increased although it has higher nanoclay content as compared with Film 5.

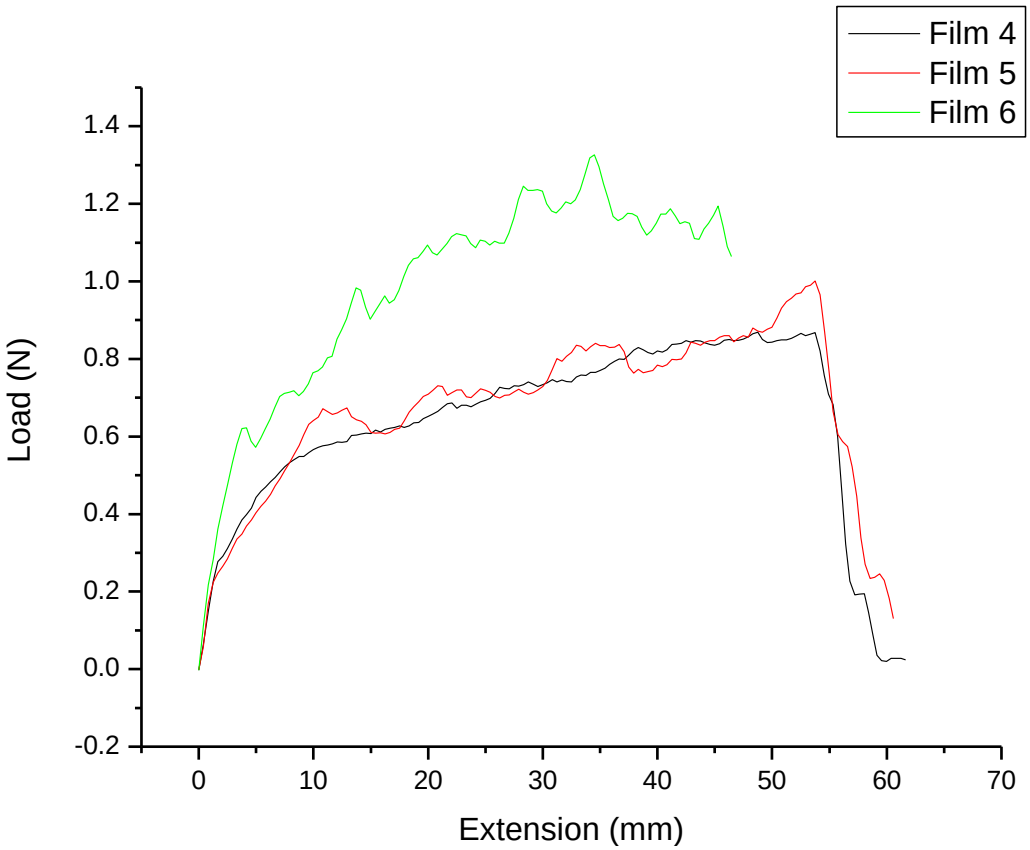

Figure 4.34 Tear load-extension curve of Film 4, Film 5 and Film 6

- Condition of 20 wt % Compatibilizer Presence

Tear test results for Film 7, Film 8 and Film 9 are shown in Figure 4.35. Film 7 includes 1%, Film 8 includes 3% and Film 9 includes 5% nanoclay content.

As it is seen from Table 4.5, tear strength for films 7, 8 and 9 firstly decreases then increases as the nanoclay content increases from 1% to 5%. The reasons are similar to the results explained before.

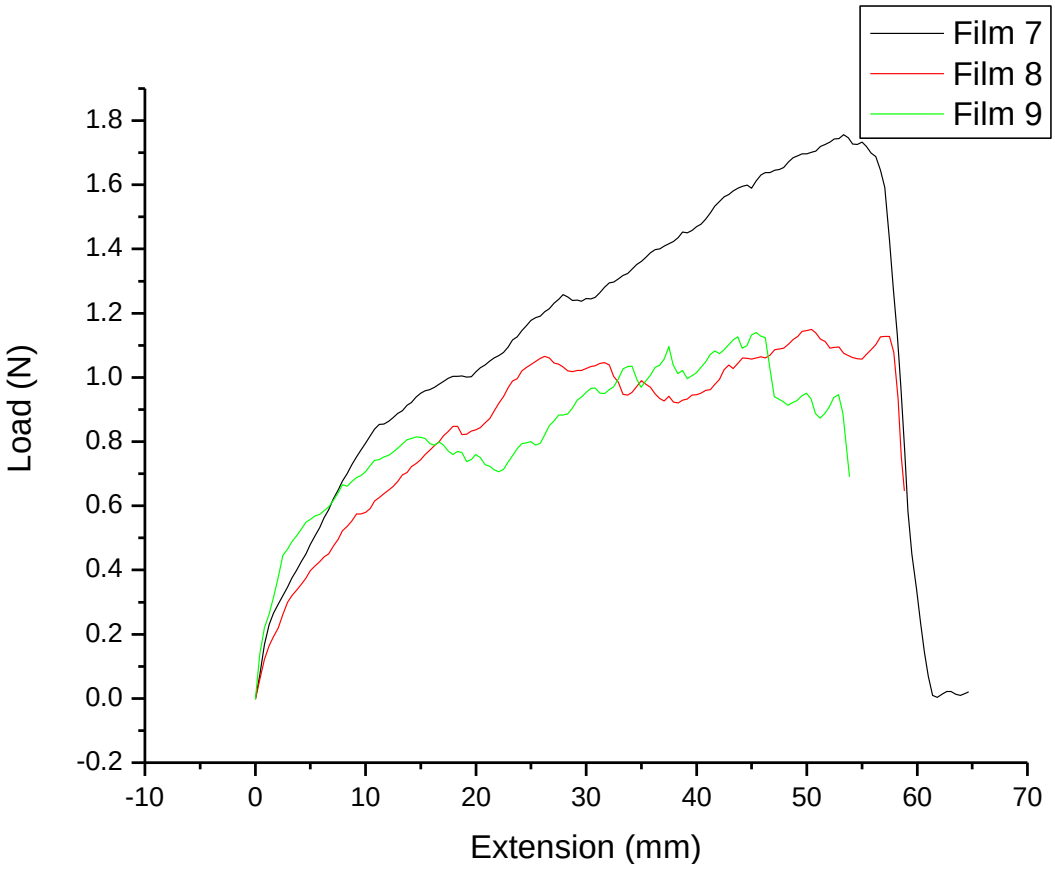

Figure 4.35 Tear load-extension curve of Film 7, Film 8 and Film 9

Evaluation According to Compatibilizer Content:

- Condition of 1 wt % Nanoclay Presence

Film 1 includes 10%, Film 4 includes 15% and Film 7 includes 20% compatibilizer.

As it is seen from Table 4.5, tear strength for films 1, 4 and 7 decreases first then increases as the compatibilizer content increases from 10% to 20%. For Film 4 (15% compatibilizer content), the tear strength decreased as compared with Film 1 (10% compatibilizer content), but for Film 7 (20% compatibilizer content) the tear strength increased as compared with Film 4.

- Condition of 3 wt % Nanoclay Presence

Film 2 includes 10%, Film 5 includes 15% and Film 8 includes 20% compatibilizer.

As it is seen from Table 4.5, tear strength for films 2, 5 and 8 decreases first then increases as the compatibilizer content increases from 10% to 20%. For Film 5 (15% compatibilizer content), the tear strength decreased as compared with Film 2 (10% compatibilizer content), but for Film 8 (20% compatibilizer content), the tear strength increased as compared with Film 5.

- Condition of 5 wt % Nanoclay Presence

Film 3 includes 10%, Film 6 includes 15% and Film 9 includes 20% compatibilizer.

As it is seen from Table 4.5, tear strength for films 3, 6 and 9 decreases as the compatibilizer content increases from 10% to 20%.

4.3.5. Bust Strength Analysis

Burst strength analysis was done based on the nanoclay and compatibilizer content of the reinforced PP films.

To compare the burst strength of the films, load values (N) at the time of burst were used. Load and extension values for burst strength tests are shown in Table 4.6.

Evaluation According to Nanoclay Content:

- Condition of 10 wt % Compatibilizer Presence

Burst strength test results for Film 1, Film 2 and Film 3 are shown in Figure 4.36. Film 1 includes 1%, Film 2 includes 3% and Film 3 includes 5% nanoclay.

As seen from Figure 4.36, the extension value of Film 1 is 45 mm. However, the extension value of Film 2 is 33 mm and the extension value of Film 3 is 20 mm. This shows that as the nanoclay content of the nanoclay reinforced films, having 10% compatibilizer content, increases, the extension of the films decreases.

Table 4.6 Load and extension values from burst strength tests

FILM #		SAMPLE 1	SAMPLE 2	SAMPLE 3	SAMPLE 4	SAMPLE 5	AVERAGE
Film 1	Load (N)	53.5	52.26	51.81	53.51	55.62	53.34
	Extension (mm)	44.6	44.6	43.7	43.7	44	44.06
Film 2	Load (N)	43.06	45.35	44.93	43.55	44.47	44.272
	Extension (mm)	28.2	38.6	30.7	34.7	27.6	31.96
Film 3	Load (N)	52.35	53.69	55.34	53.69	50.28	53.07
	Extension (mm)	14.3	15.5	17.2	17.1	14.9	15.8
Film 4	Load (N)	38.48	39.77	40.2	41.81	49.28	41.908
	Extension (mm)	24.6	32.3	34.8	37.8	34.2	32.74
Film 5	Load (N)	34.61	36.45	37.79	38.5	39.67	37.404
	Extension (mm)	17.3	27.9	25.4	27.2	24.4	24.44
Film 6	Load (N)	51.9	52.1	49.63	53.59	54.41	52.326
	Extension (mm)	12.9	15	13.3	15.2	14	14.08
Film 7	Load (N)	47.53	47.04	46.75	44.54	48.49	46.87
	Extension (mm)	44.1	44.8	43.4	44.3	43.6	44.04
Film 8	Load (N)	41.46	46.11	42.59	42.63	45.32	43.622
	Extension (mm)	29	33.5	26.2	30.2	32.8	30.34
Film 9	Load (N)	60.07	59.58	56.91	63.51	56.99	59.412
	Extension (mm)	16.7	15.6	17.6	17.1	16.9	16.78

As it is seen from Table 4.6, burst strength for films 1, 2 and 3 decreases first then increases as the nanoclay content increases from 1% to 5%. Although the burst strength for Film 1 cannot be determined since the film could not burst in the specified extension range that was determined according to the instruments available space for this test, it is obvious from the data that the maximum load that Film 1 can burst is over 60, which is higher than Film 2. The increase in the nanoclay content makes the films have lower burst strength since nanoclay dispersion cannot be achieved as good as in the films having lower nanoclay content. Moreover, nanoclay dispersion in Film 1 is better than Film 2. When Film 1 is tried to be bursted, the more evenly dispersed nanoparticles resist bursting force (load) making the burst strength higher. However, when Film 2 is tried to be bursted, since the nanoclay dispersion is not as good as Film 1 and nanoclay particles are not evenly dispersed in the film structure to resist the bursting force, the burst strength decreases compared to Film 1. For Film 3, screw speed was increased which made the polymer and the nanoclay mix more homogeneously; this increased the burst strength since the more the nanoclay particles are evenly dispersed the better they resist the bursting force. Better nanoclay dispersion in Film 3 can be seen from the SEM micrographs of morphology analysis. Because of this, for Film 2 (3% nanoclay content) the burst strength decreased as compared with Film 1 (1% nanoclay content), but for Film 3 (5% nanoclay content) the burst strength increased although it has higher nanoclay content as compared with Film 2.

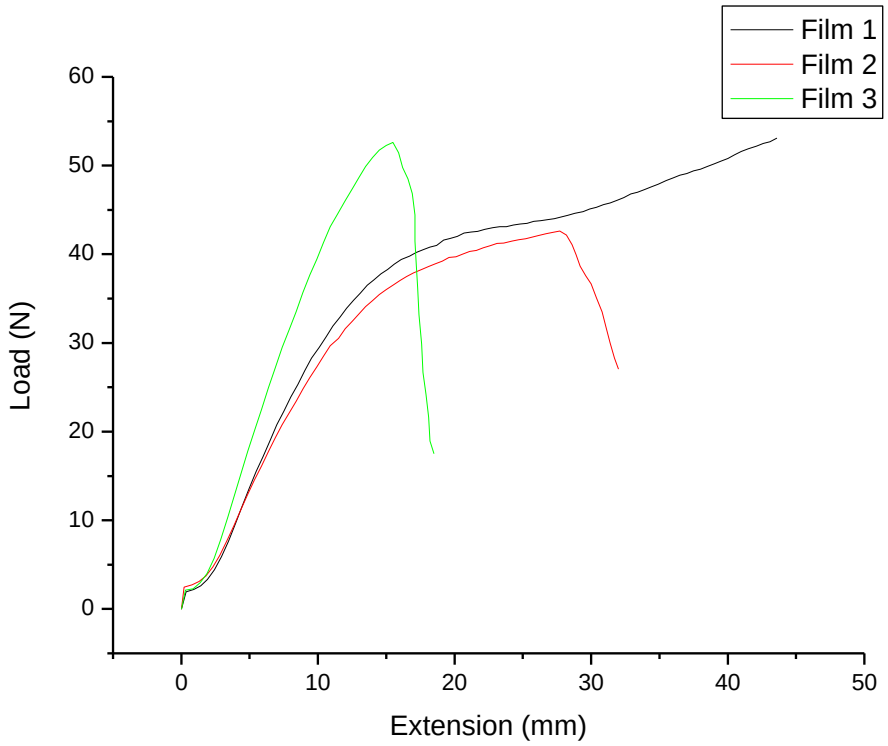

Figure 4.36 Burst load-extension curve of Film 1, Film 2 and Film 3

- Condition of 15 wt % Compatibilizer Presence

Burst strength test results for Film 4, Film 5 and Film 6 can be seen in Figure 4.37. Film 4 includes 1%, Film 5 includes 3% and Film 6 includes 5% nanoclay.

As seen from Figure 4.37, the extension value of Film 4 is 27.5 mm. However, the extension value of Film 5 is 27.5 mm and the extension value of Film 6 is 15 mm. This shows that as the nanoclay content of the nanoclay reinforced films, having 15% compatibilizer content, increases, the extension of the films decreases.

As it is seen from Table 4.6, burst strength for films 4, 5 and 6 decreases first then increases as the nanoclay content increases from 1% to 5%. The increase in the nanoclay content makes the films have lower burst strength since nanoclay dispersion cannot be achieved as good

as in the films having lower nanoclay content. Also, as it can be seen from morphology analysis nanoclay dispersion in Film 4 is better than Film 5. Therefore, when Film 4 is tried to be bursted, the more evenly dispersed nanoparticles resist bursting force (load) making the burst strength higher. However, when Film 5 is tried to be bursted, since the nanoclay dispersion is not as good as Film 4 and nanoclay particles are not evenly dispersed in the film structure to resist the bursting force, burst strength decreases compared to Film 4. For Film 6, screw speed was increased which made the polymer and the nanoclay mix more homogeneously; this increased the burst strength since the more the nanoclay particles are evenly dispersed the better they resist the bursting force. Better nanoclay dispersion in Film 6 can be seen from the SEM micrographs of morphology analysis. Because of this, for Film 5 (3% nanoclay content) the burst strength decreased as compared with Film 4 (1% nanoclay content), but for Film 6 (5% nanoclay content) the burst strength increased although it has higher nanoclay content as compared with Film 5.

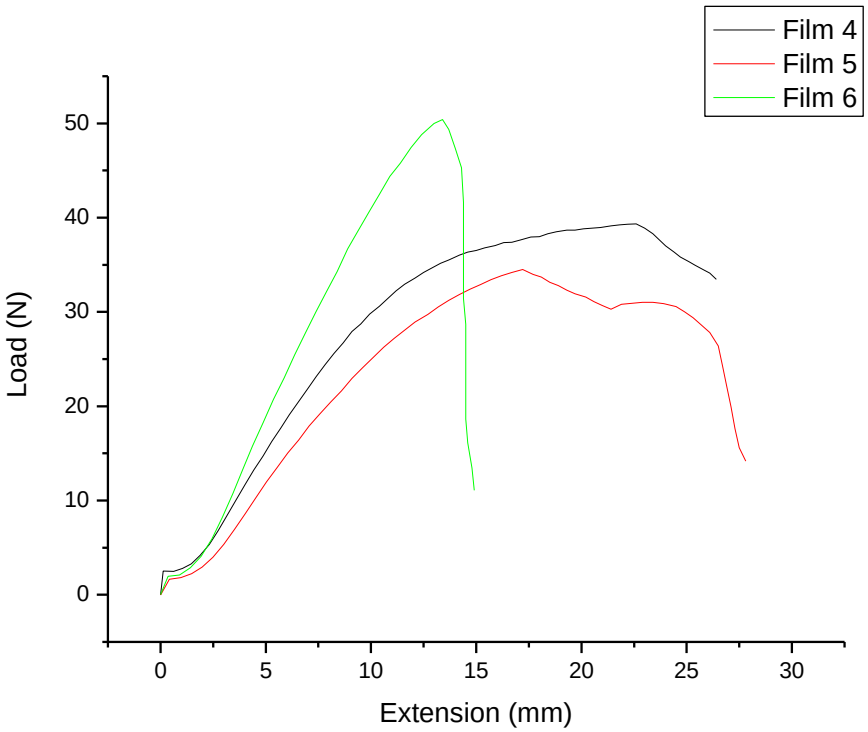

Figure 4.37 Burst load-extension curve of Film 4, Film 5 and Film 6

- Condition of 20 wt % Compatibilizer Presence

Burst strength test results for Film 7, Film 8 and Film 9 are shown in Figure 4.38. Film 7 includes 1%, Film 8 includes 3% and Film 9 includes 5% nanoclay content.

As seen from Figure 4.38, the extension value of Film 7 is 45 mm. However, the extension value of Film 8 is 35 mm and the extension value of Film 9 is 18 mm ranges. This shows that as the nanoclay content of the nanoclay reinforced films, having 20% compatibilizer content, increases, the extension of the films decreases.

As it is seen from Table 4.6, burst strength for films 7, 8 and 9 decreases first then increases as the nanoclay content increases from 1% to 5%. Although the burst strength for Film 7 cannot be determined since the film could not burst in the specified extension range that was determined according to the instruments available space for this test, it is obvious from the data that the maximum load that Film 7 can burst is over 47 which is higher than Film 8. The increase in the nanoclay content makes the films have lower burst strength since nanoclay dispersion cannot be achieved as good as in the films having lower nanoclay content. Moreover, nanoclay dispersion in Film 7 is better than Film 8. Therefore, when Film 7 is tried to be bursted, the more evenly dispersed nanoparticles resist bursting force (load) making the burst strength higher. However, when Film 8 is tried to be bursted, since the nanoclay dispersion is not as good as Film 7 and nanoclay particles are not evenly dispersed in the film structure to resist the bursting force, burst strength decreases compared to Film 7. For Film 9, screw speed was increased which made the polymer and the nanoclay mix more homogeneously; this increased the burst strength since the more the nanoclay particles are evenly dispersed the better they resist the bursting force. Better nanoclay dispersion in Film 9 can be seen from the SEM micrographs of morphology analysis. Because of this, for Film 8 (3% nanoclay content) the burst strength decreased as

compared with Film 7 (1% nanoclay content), but for Film 9 (5% nanoclay content) the burst strength increased although it has higher nanoclay content as compared with Film 8.

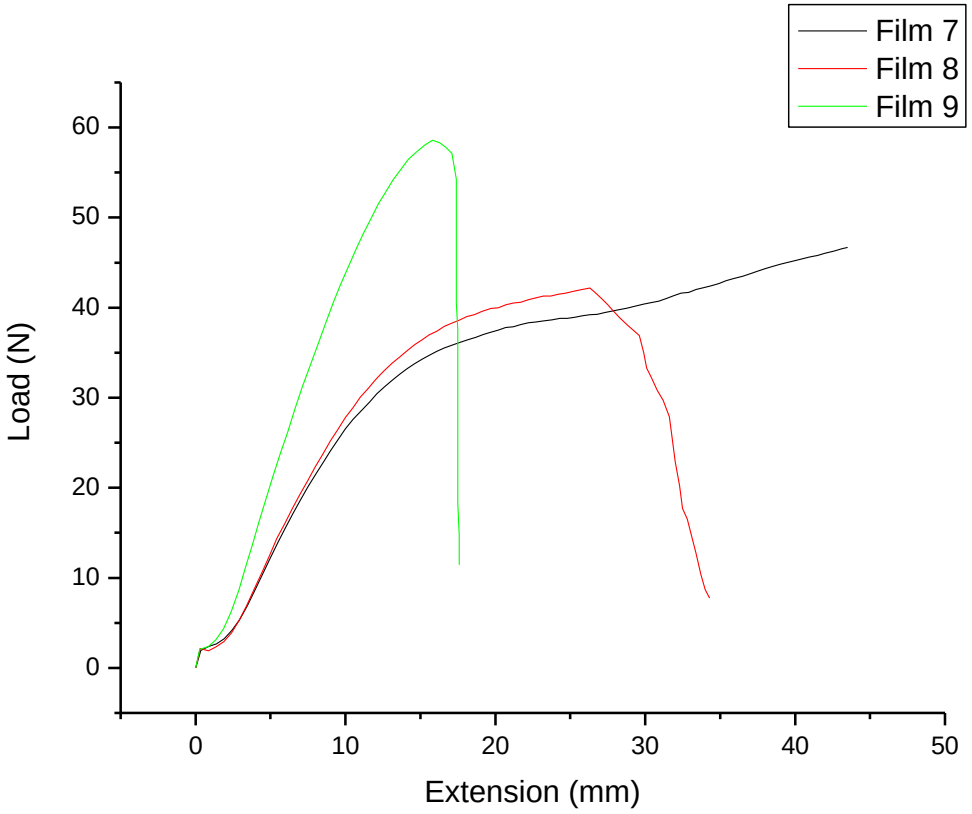

Figure 4.38 Burst load-extension curve of Film 7, Film 8 and Film 9

Evaluation According to Compatibilizer Content:

- *Condition of 1 wt % Nanoclay Presence*

Film 1 includes 10%, Film 4 includes 15% and Film 7 includes 20% compatibilizer content.

As seen from Figure 4.39, the extension value of Film 1 is 45 mm. However, the extension value of Film 4 is 30 mm and the extension value of Film 7 is 45 mm. This shows that

as the compatibilizer content of the nanoclay reinforced films, having 1% nanoclay content, increases, the extension of the films firstly decreases then increases.

As it is seen from Table 4.6, burst strength for films 1, 4 and 7 firstly decreases then increases as the compatibilizer content increases from 10% to 20%.

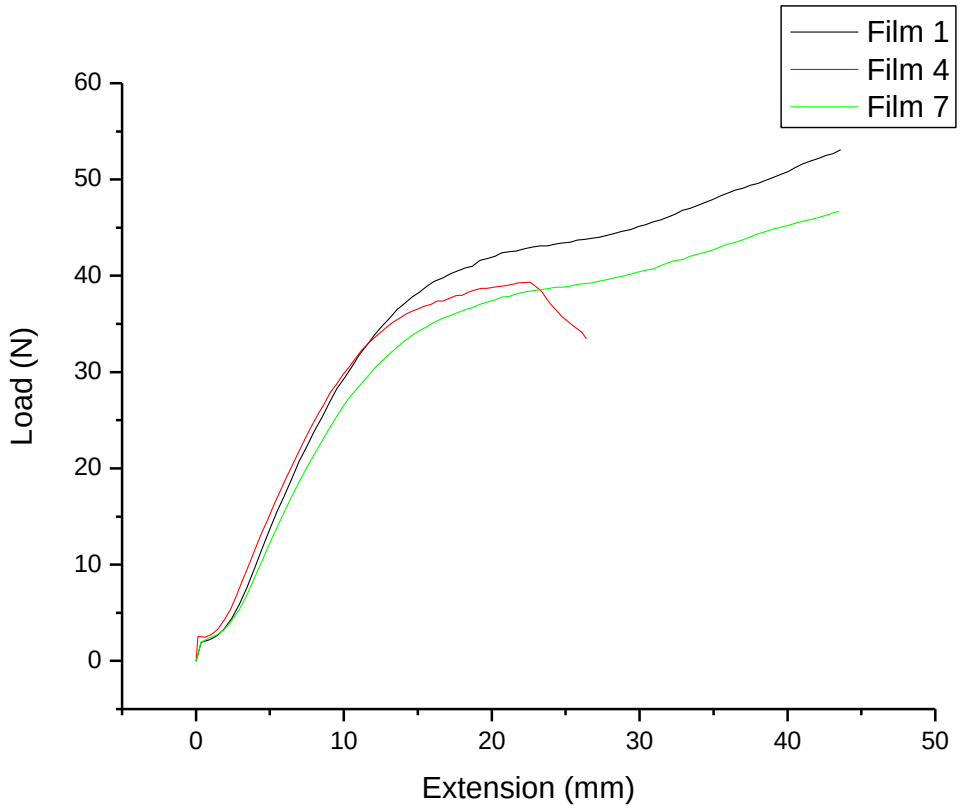

Figure 4.39 Burst load-extension curve of Film 1, Film 4 and Film 7

- *Condition of 3 w % Nanoclay Presence*

Film 2 includes 10%, Film 5 includes 15% and Film 8 includes 20% compatibilizer content.

As seen from Figure 4.40, the extension value of Film 2 is 32.5 mm. However, the extension value of Film 5 is 27.5 mm and the extension value of Film 8 is 35 mm ranges. This

shows that as the compatibilizer content of the nanoclay reinforced films, having 3% nanoclay content, increases, the extension of the films firstly decreases then increases.

As it is seen from Table 4.6, burst strength for films 2, 5 and 8 firstly decreases then increases as the compatibilizer content increases from 10% to 20%.

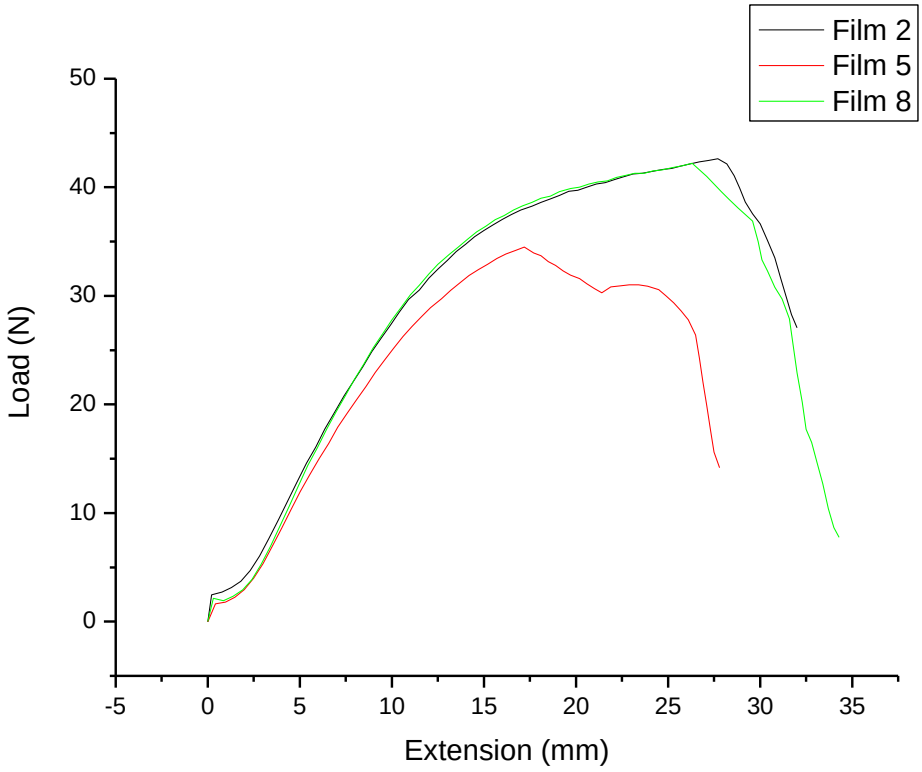

Figure 4.40 Burst load-extension curve of Film 2, Film 5 and Film 8

- *Condition of 5 w % Nanoclay Presence*

Film 3 includes 10%, Film 6 includes 15% and Film 9 includes 20% compatibilizer content.

As seen from Figure 4.41, the extension value of Film 3 is 18 mm. However, the extension value of Film 6 is 15 mm and the extension value of Film 9 is 18 mm. This shows that

as the compatibilizer content of the nanoclay reinforced films, having 5% nanoclay content, increases, the extension of the films firstly decreases then increases as the compatibilizer content increases from 10% to 20%.

As it is seen from Table 4.6, burst strength for films 3, 6 and 9 firstly decreases then increases as the compatibilizer content increases from 10% to 20%.

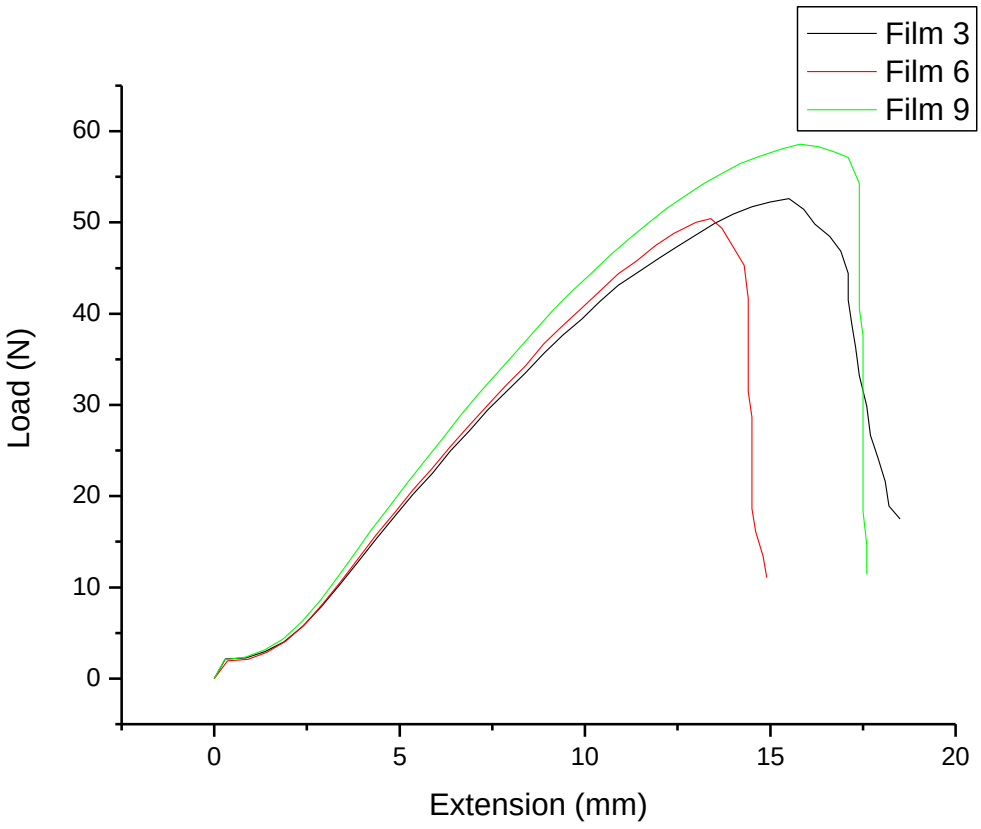

Figure 4.41 Burst load-extension curve of Film 3, Film 6 and Film 9

CHAPTER 5

DEVELOPMENT OF PBI MEMBRANE

5.1. Materials Used

To increase the fuel cell performance at high temperatures, the polymer electrolyte membrane must have better water retention characteristics to allow higher proton conductivity that improves fuel cell efficiency.

In order to extend the fuel cell operation temperature range, novel membranes having better material properties, such as higher thermal stability than Nafion®, need to be produced.

A material that is used for high temperature polymer electrolyte fuel cells is polybenzimidazole (PBI). Polybenzimidazoles are usually used after they are doped with acids because they gain high proton conductivity with no or low humidification after doping with acids. Especially phosphoric acid is used to dope polybenzimidazoles.

Therefore, PBI was synthesized to be used as fuel cell membrane.

5.1.1. Polymer and Dopant

PBI is chosen as the polymer because of its outstanding characteristics that are needed for fuel cell membranes. PBI has excellent thermal stability. With some modifications using doping process, thermal stability of the PBI membranes can be increased. Since PBI reacts easily with acids, it is easy to dope it with phosphoric acid which is the most frequently used dopant for PBI

[27, 28]. PBI can keep its mechanical properties up to 300 °C. As the temperature increases, the performance of the fuel cell increases, too. Therefore, polymers that can withstand high temperatures such as PBI are good candidates as electrolytes. By using PBI as a polymer for fuel cell membrane, temperature limitation that is imposed by the electrolyte materials can be overcome.

As acid, phosphoric acid (H_3PO_4) was used for doping in this project. Doping is a process which includes immersing of a polymer film into an aqueous or aqueous-organic solution of an acid for a certain period [27]. By doping PBI with phosphoric acid, the proton conductivity can be increased. In addition, doping process eliminates the need for water to have high proton conductivity and helps to improve thermal stability. Therefore, phosphoric acid-doped PBI will not require humidification in high temperature fuel cell applications.

5.1.2. Synthesis of PBI

To synthesize PBI polymer, 3.24 g (15.1 mmol) of 3, 3, 4, 4'-tetraaminobiphenyl and 2.51 g (15.1 mmol) of isophthalic acid were mixed in 180 g of polyphosphoric acid and 0.05 g of triphenyl phosphite. The reaction system consisted of a 250 ml four neck flask equipped with a calcium chloride drying tube and nitrogen inlet. Stirring was done by a heating/stirring mantle. The system was heated at 200 °C for 10 hours. Then, the polymer was isolated by pouring down the reaction mixture into deionised (DI) water. The polymer was then filtered by using filter papers and applying vacuum. Then, the polymer obtained was neutralized with potassium hydroxide and filtered again. After neutralization process, the polymer powder was rinsed with deionised water and filtered. The polymer obtained was left overnight inside an oven at 50 °C. As a last step the polymer was ground in order to have polymer powder [29].

5.2 Machines Used

5.2.1. Ultrasonic Generator

In this project, broadband ultrasonic generator was used in order atomize the solution with the help of an ultrasonic nozzle. The broadband ultrasonic generator can be seen in Figure 5.1. This generator, which is designed and manufactured by Sono-tek Corp., delivers a high frequency electrical energy required to operate ultrasonic atomizing nozzles that are also supplied by Sono-tek.

One of the features of the ultrasonic generator is that it can operate over a frequency range of 25-120 kHz, which can be selected according to the nozzle used. The ultrasonic generator uses advanced phase-locked-loop control technology in order to lock onto a nozzle's specific operating frequency automatically. It includes an output for connection to a remote alarm, an input for remote power control and an LCD power meter and power level control for setup and monitoring of nozzle operation. It has the capability of providing audible and visual alarms if a system malfunction occurs. The ultrasonic generator can be triggered on/off by an external control signal [30].

Figure 5.1 Ultrasonic Broadband Generator [30]

5.2.2. Ultrasonic Nozzle

Sono-tek ultrasonic nozzle that has a corrosion-resistant titanium and stainless steel construction was used as titanium has good acoustical properties, high tensile strength, and excellent corrosion resistance. This ultrasonic spraying system is chosen for the project because it is more precise, more controllable, and more environmentally friendly liquid atomization. This highly controllable spray produces reliable, consistent results by producing a tight and controllable drop size distribution which gives the flexibility to influence coating porosity. By the help of ultrasonic energy, it is possible to disperse agglomerated particles and obtain homogenous coatings. Ultrasonic nozzle provides not only 80% reduction in material consumption but also provides reduced wasteful overspray and atmospheric contamination due

to soft spray characteristics. It has a non-clogging design that saves time for cleaning the inside of the nozzle. Only the solvent of the polymer is enough to clean the nozzle. It has no moving parts so there is no chance to encounter with the problem of wearing out. This technique can be used for substrate coatings, moisturizing, spray drying, web coating, fine-line spraying, and many other industrial and R&D applications [30]. The ultrasonic nozzle and its parts can be seen in Figure 5.2.

The ultrasonic atomizing nozzle technology is different from other spray nozzle technologies. As the ultrasonic atomizing nozzles are pressureless, they create a soft, low-velocity spray, typically in the order of 7.5-12.5 cm (3-5 inches) per second. Other atomization techniques using pressure to spray, produce drops with velocities well over 100 times that produced by ultrasonic atomization. This velocity differential means that pressure sprays generate on the order of 10,000 as much kinetic energy as do ultrasonically atomized sprays. This difference in spray energy creates some outcomes. In coating applications, the unpressurized, low-velocity spray decreases the amount of overspray by making the drops settle on the substrate rather than bouncing off it. Therefore, substantial material savings and decrease in emissions into the environment can be easily achieved [30].

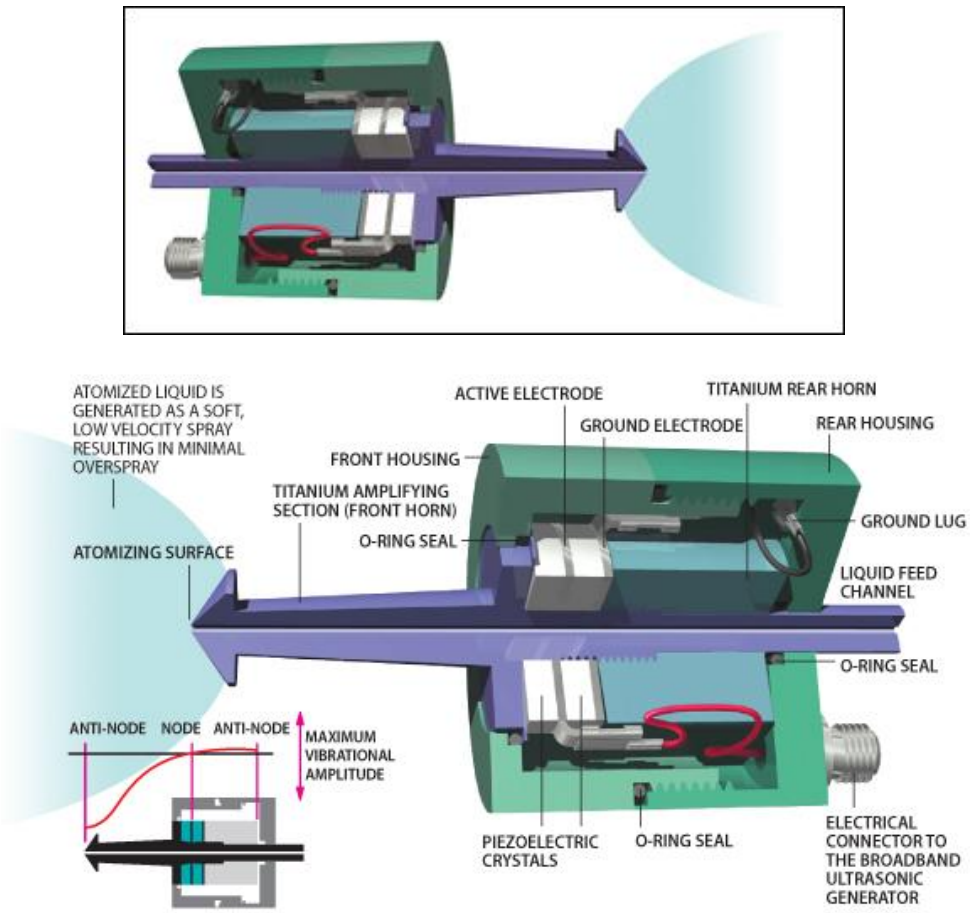

Figure 5.2 Ultrasonic nozzle and its parts [30]

Also Sono-Tek ultrasonic nozzle system that we use has an optional dual liquid feed assembly installed. This dual liquid feed option gives us the opportunity to be able to mix two liquids right at the nozzle's atomizing surface. Therefore, there is no need for premature mixing of components and it is also ideal for micro-encapsulation [30]. The ultrasonic nozzle cross-sectional view can be seen in Figure 5.3.

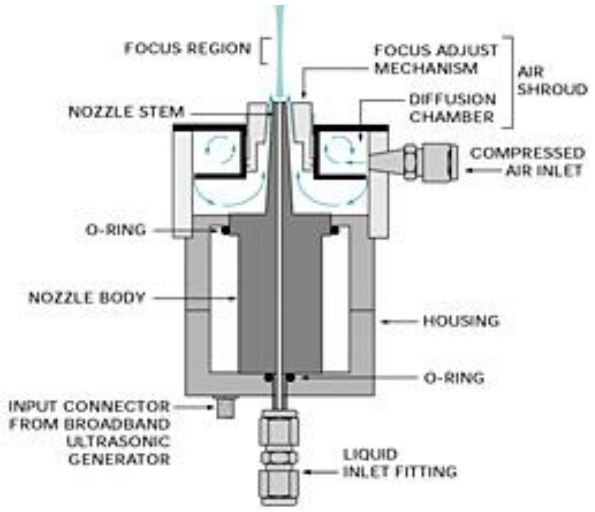

Figure 5.3 Ultrasonic nozzle cross-sectional view [30]

The AccuMist^{TM} system combines microspray ultrasonic atomizing nozzle with low pressure air for the formation of a soft, highly focused beam of small spray drops. 6894 Pa (1 psi) compressed air is inserted into the diffusion chamber of the air shroud that forms a uniformly distributed flow of air around the nozzle stem. The spray that is ultrasonically produced at the tip of the stem is immediately entrained in the low pressure air stream. The focusing mechanism on the air shroud allows complete control of spray width having a range of 2mm - 10mm.The spray envelope is bow-shaped. The width of the bow is controlled by moving the focus-adjust mechanism in and out [30].

Working Principle Of Ultrasonic Spray Nozzles

Ultrasonic nozzles employ high frequency sound waves which are beyond the range of human hearing. Ultrasonic nozzles have disc-shaped ceramic piezoelectric transducers that convert electrical energy into mechanical energy. These piezoelectric transducers receive electrical input in the form of a high frequency signal from a power generator. Then they convert

this into vibratory motion at the same frequency. Two titanium cylinders exaggerate the motion and enhance the vibration amplitude at the atomizing surface.

By the excitation of the piezoelectric crystals of the nozzles, a transverse standing wave along the length of the nozzle is produced. The ultrasonic energy that is produced by the crystals goes through a step transition and amplification as the standing wave as it traverses the length of the nozzle.

In ultrasonic generators, power is controlled by adjusting the output level on the power supply and power levels are no more than 15 watts for ultrasonic atomization [30].

5.2.3. Dispensing Robot

In this project I&J4300-LF Benchtop Dispensing Robot, which is a programmable coating system, was used to automate the manual dispensing operations. By automating the dispensing operations using the desktop dispensing robot, more uniform surface of polymer electrolyte membrane, saving costs in material waste and time can be achieved [31].

Figure 5.4 Dispenser robot and teach pendant [31]

The I&J4300-LF model 3-axis desktop dispensing robot that was used in this project is a RoHS-compliant lead-free dispensing robot having an easy to use teaching pendant that is used to control the robot. The dispenser robot and its teach pendant are shown in Figure 5.4.

Programming of the robot can be done by teach pendant, using the dispensing software that gives the user through step-by-step instructions to generate different shaped coated surfaces. It can also be programmed by a PC. This compact-sized desktop robot has a working area of 300 x 300mm (11.81" x 11.81"). 100 programs can be saved in the memory of the robot. It has a continuous path motion for precision xyz dispensing and also interpolates lines and arcs for three dimensional dispensing [31].

5.3. Membrane Fabrication

5.3.1. Programming of Dispensing Robot

In order to use the dispensing robot properly, it needs to be programmed according to the coating shape that is needed.

Fifteen programs that can make different shapes with different time durations were written. Some of the programs that were used in this project are shown below. The other programs that were written are shown in APPENDIX B.

5.3.1.1. Program 1

This program makes the dispensing robot draw a square (Figure 5.5).

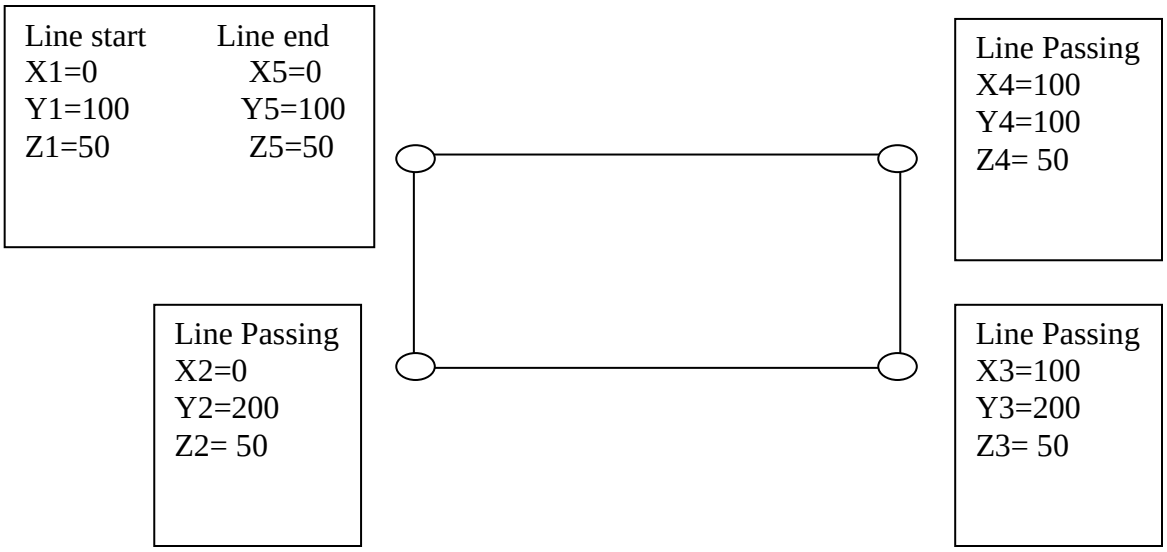

Figure 5.5 Steps of program 1

Steps of the program are as follows:

1) Set up – Line speed – Enter – 55 – Enter

   Set up – XY move speed – Enter – 5 - Enter

2) Menu 2 – Numerical move – Enter

   X1=0 Y1=100 Z1=50

3) Enter (or point) – Line start – Enter

4) Menu 2 – Numerical Move – Enter

   X2=0 Y2=200 Z2=50

5) Enter (or point) – Line passing – Enter

6) Menu 2 – Numerical move – Enter

   X3=100 Y3=200 Z3=50

7) Enter (or point) – Line passing – Enter

8) Menu 2 – Numerical move – Enter

X4=100 Y4=100 Z4=50

9) Enter (or point) – Line passing – Enter

10) Menu 2 – Numerical move – Enter

X5=0 Y5=100 Z5=50

11) Enter (or point) – Line end – Enter

12) Enter – End Program – Enter

13) Run

5.3.1.2. Program 2

This program makes the dispensing robot draw a square and then fill inside the square (Figure 5.6).

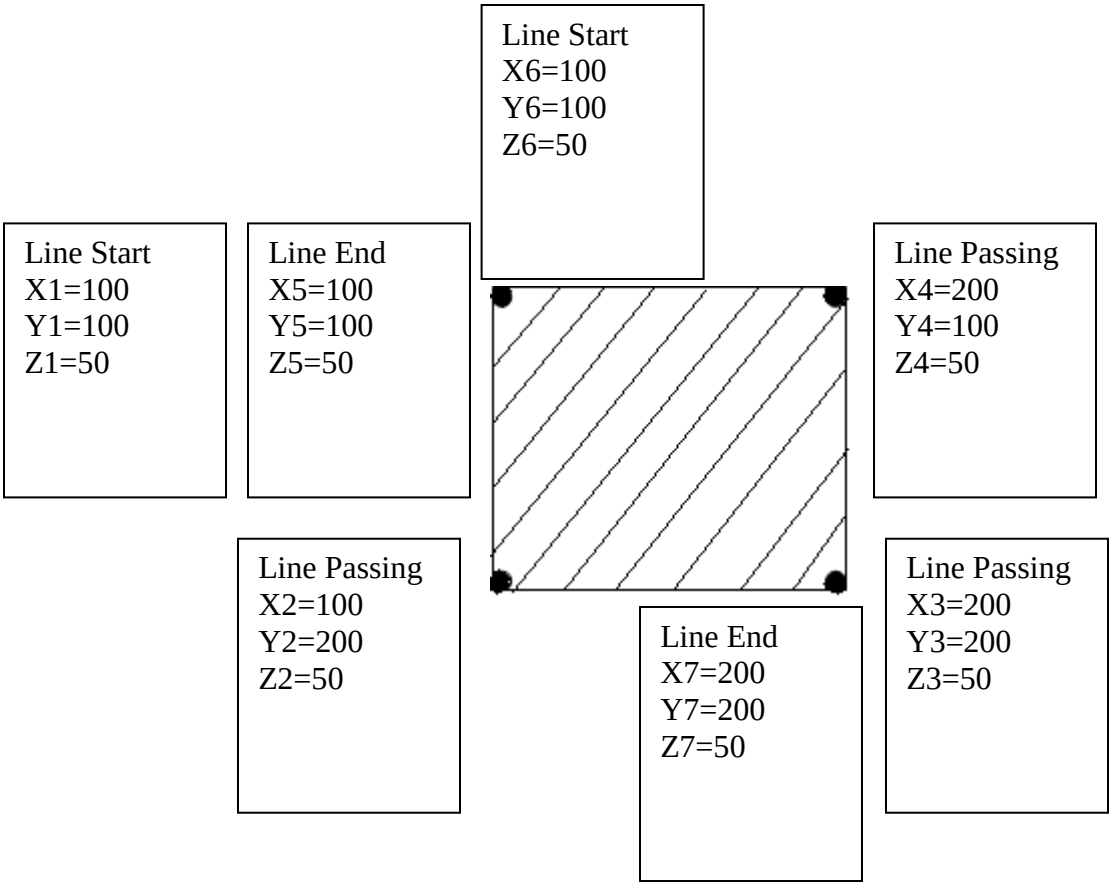

Figure 5.6 Steps of program 2

Steps of the program are as follows:

1) Set up – Line Speed – Enter – 30 – Enter

   Set up – XY Move Speed – Enter – 30 – Enter

2) Menu 2 – Numerical Move – Enter

   X1 = 100 Y1 = 100 Z1 = 50

3) Enter (or Point) – Line Start – Enter

4) Menu 2 – Numerical Move – Enter

   X2 = 100 Y2 = 200 Z2 = 50

5) Enter (or Point) – Line Passing – Enter

6) Menu 2 – Numerical Move – Enter

X3 = 200 Y3 = 200 Z3 = 50

7) Enter (or Point) – Line Passing – Enter

8) Menu 2 – Numerical Move – Enter

X4 = 200 Y4 = 100 Z4 = 50

9) Enter (or Point) – Line Passing – Enter

10) Menu 2 – Numerical Move – Enter

X5 = 100 Y5 = 100 Z5 = 50

11) Enter (or Point) – Line End - Enter

12) Enter (or Point) – Brush Area – Enter – Select (1 - Rectangle) – Width – 5 – Enter – 1.X 2.Y:1 (Rectangle) – Enter

13) Menu 2 – Numerical Move – Enter

X6= 100 Y6=100 Z6=50

14) Enter (or Point) – Line Start – Enter

15) Menu 2 – Numerical Move – Enter

X7=200 Y7=200 Z7=50

16) Enter (or Point) – Line End – Enter

17) Enter (or Point) – End Program – Enter

18) Run

5.3.2. Manufacturing Process of the Membrane

Firstly, the PBI powder obtained was dissolved in N,N-dimethylacetamide (DMAc) by heating at 160 °C under stirring [32]. The solution had 5wt% PBI with 1.5% of LiCl.

Then, 5 wt% PBI solution was put into syringe of the ultrasonic nozzle and fed to the nozzle that was mounted on the dispensing robot. The solution was sprayed on the glass plate. The glass plate was heated to 60 °C and the solvent was evaporated. The plate was immersed in deionised water in order to detach the membrane from the plate [32].

CHAPTER 6

MODEL OF MEMBRANE BEHAVIOR

6.1. Assumptions of the Model

The following assumptions are made for the model:

1) **Ideal gas properties:** All the gases in diffuser regions exhibit ideal gas behavior.
2) **Ideal gas mixtures:** Reactant gases are well mixed and behave as ideal gas mixture.
3) Incompressible flow
4) **Laminar flow:** Flow is laminar everywhere because of small gas pressure gradient and low Reynolds number.
5) **Isotropic and homogeneous membrane and electrode structures:** Both of the electrodes and membrane are made of homogeneous and isotropic materials. (Isotropic macro-homogeneous porous regions)
6) Negligible ohmic potential drop in solid components
7) **Uniform temperature distribution:** Temperature distribution across the cell is uniform.
8) **Impermeable PEM:** The PEM is impermeable to reactant gases and water.
9) **Proton and electron transport:** Protons can only transport through the electrolyte membrane and electrons through the solid phase.

10) **Species on the anode and cathode sides:** Two species (hydrogen and water) are considered on the anode side and three species (oxygen, water and nitrogen) are considered on the cathode side.
11) **Steady state:** Fuel cell is operating at the steady state.
12) **Multi domain approach:** For this model, multi domain approach is chosen by using separate governing equations in each subdomain.
13) **Only gas phases present:** Water is expected to exist only in vapor phase. At elevated temperatures no aqueous or liquid phases exist.

6.2. Model Definition

For high temperature polymer electrolyte fuel cell membrane having a PBI based membrane, a two dimensional mathematical model was developed as shown in Figure 6.1. The model has three domains:

a) An anode
b) A PEM
c) A cathode

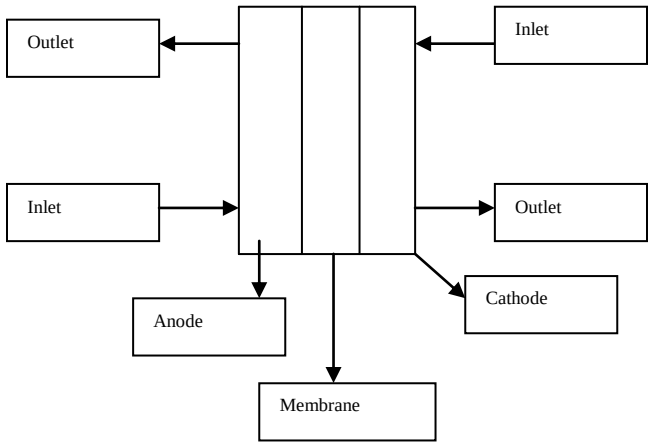

Figure 6.1 Model geometry with its subdomains and boundary labels

6.3. Governing Equations

The governing equations of all of the domains were obtained.

6.3.1. Anode

6.3.1.1. Flow Channels: Maxwell-Stefan Mass Balances (Conservation of Species)

Two species such as H_2 and H_2O are taken into consideration in the anode side flow channels. The multicomponent diffusion and convection in flow channels are described by the Maxwell-Stefan equation. This equation solves for the fluxes in terms of mass fraction. The equation for the Maxwell-Stefan multicomponent diffusion is [33, 34, 35, 36]:

$$\frac{\partial}{\partial t}\rho\omega_i + \nabla\left[-\rho\omega_i\sum_{j=1}^{N} D_{ij}\left\{\frac{M}{M_j}\left(\nabla\omega_j + \omega_j\frac{\nabla M}{M}\right) + (x_j - \omega_j)\frac{\nabla p}{p}\right\} + \omega_i\rho\boldsymbol{u} + D_i^T\frac{\nabla T}{T}\right] = R_i \quad \textbf{(6.1)}$$

where:

ω: mass fraction

p: pressure (Pa)

T: (cell) temperature (K)

u: velocity vector (m/s)

ρ: density of the mixture of the gas phase (kg/m^3)

D_{ij} : Maxwell-Stefan diffusion coefficient (m^2/s)

R_i: reaction rate ($kg/(m^3.s)$)

x: mole fraction

M: molecular (molar) mass (kg/mol)

i or j: These subscripts represent each species of hydrogen and water.

It is assumed that temperature-driven diffusion, which sets the source term R to zero, is insignificant. Therefore, the reaction rate is zero in the flow channel.

Density of the mixture of the gas phase is a function of mixture components and is described by the equation:

$$\rho = (p/RT)\sum_i M_i\ x_i \tag{6.2}$$

where:

R: universal gas constant (8.314 J/(mol.K))

On the anode side, the hydrogen transport equation is solved first. Then, mass fraction of water can be obtained by the equation:

$$\omega_{H2O} = 1 - \omega_{H2} \tag{6.3}$$

6.3.1.2. Gas Diffusion Layer and Catalyst Layer: Darcy's Law And Mass Conservation Equation (Porous Media Fluid Flow)

Continuity equation gives the gas velocity as below [33, 34, 35, 36]:

$$\nabla.(\rho \boldsymbol{u}) = 0 \tag{6.4}$$

u: gas velocity (m/s)

The pressure gradient, viscosity of the fluid and structure of the porous media determine the velocity vector according to the Darcy's Law for porous media:

$$\boldsymbol{u} = -\frac{k_p}{\eta}\nabla p \tag{6.5}$$

where:

k_p: electrode's permeability (m^2)

η: gas's viscosity (Pa.s)

The mixture density of the gas phase is given by the ideal gas law:

$$\rho = (p/RT)\sum_i M_i\ x_i \tag{6.6}$$

The pressure at the outlets and inlets are:

$$p = p_{a,in}\ (\text{at inlet}) \tag{6.7}$$

$$p = p_{ref}\ (at\ outlet) \tag{6.8}$$

The velocity of gas is determined from the total mass flow that is given by the electrochemical reaction rate at the electrode boundary:

$$-\boldsymbol{n}.\boldsymbol{u}\boldsymbol{I}_{anode} = \frac{j_{anode}}{\rho F}\left[\frac{M_{H_2}}{2} + \lambda_{H_2O}M_{H_2O}\right] \tag{6.9}$$

Gas flow velocity is determined by Darcy's Law; the total mass conservation is preserved in the anode gas backing with this given boundary condition.

6.3.2. Membrane

PBI membrane is lightweight and stable at higher temperatures (150-200°C). PBI membrane conducts the protons through the solid matrix. Its conductivity is less dependent on water content when it is compared with Nafion® membrane. Conductivity of PBI membrane can be improved by doping it with phosphoric or sulfuric acid. PBI has higher mechanical strength than Nafion®. Therefore, it leads to a reduction in membrane thickness and lower ionic resistance since the resistance is proportional to thickness of the membrane. PBI has lower permeability to hydrogen than Nafion®.

Proton conduction in PBI may be based on Grotthuss mechanism. For Nafion®, proton migration happens by the vehicle mechanism in which the translational dynamics of the electrolyte species (H_2O) is required. In vehicle mechanism, protons diffuse through the medium by the help of the solvated hydrogen ion species, H_3O^+. Therefore, the observed conductivity is directly related to the rate of the carrier diffusion. But in PBI case, the carriers show pronounced local dynamics however, reside on their sites. The H+ ions are transferred from one carrier to another by the help of hydrogen bonds (proton hoping). For PBI, there is no net transport of any carrier species across the membrane. Since the drag coefficient of water is virtually zero, it can be understood that liquid water is not carried across the membrane together with the protons. For PBI, there is no requirement for liquid water for the conduction of protons. Therefore, water management problems associated with Nafion® do not exist.

In the PBI membrane, the protons are conducted through the solid matrix. Protons diffuse in a solid state across the membrane, under the influence of an electrolyte potential gradient via migration only.

Since the protons are in a solid state, a solid-fluid "phase change" occurring during the electrochemical reactions exists. This phenomenon that only occurs in HTPEMFCs must be considered. This is achieved by considering a non-conservative form of the continuity equation [37, 38, 39, 40]:

$$\nabla.(\rho u) = S_m = \sum S_i \quad \textbf{(6.10)}$$

where:

S_i: reaction rate source term ($kg.m^{-3}.s^{-1}$)

Since the PBI membrane is assumed to be impermeable to gas flow and no fluid flow across the membrane exists, flow in the porous catalyst and diffuser regions are governed by Darcy's Law and no equations can be used for membrane region.

Because of the flow of electrical currents in both the solid and electrolyte regions, there are potential variations across each of the solid and electrolyte phases. Charge conservation is given by the equations below:

$$\nabla.i_s = \nabla.\left(-\sigma_s^{eff}\nabla\emptyset_s\right) = -j \quad \textbf{(6.11)}$$

$$\nabla.i_e = \nabla.\left(-\sigma_e^{eff}\nabla\emptyset_e\right) = +j \quad \textbf{(6.12)}$$

Charge conservation equations can be modeled by using two Conductive Media DC Modules of COMSOL Multiphysics Software Package.

The potential is specified at the gas channel/gas diffuser interfaces, while insulation conditions are specified at the catalyst layer/membrane interfaces and all other boundaries.

j= spatial rate of reaction

"j" is defined by the Butler-Volmer equation:

$$j = ai_0^{ref}\left(\frac{x_i P}{P_{ref}}\right)^{\gamma_i}\left\{exp\left[\frac{\alpha F}{RT}(\emptyset_s - \emptyset_e)\right] - exp\left[-\frac{\alpha F}{RT}(\emptyset_s - \emptyset_e)\right]\right\} \quad \textbf{(6.13)}$$

where:

$\mathbf{i_0}$= exchange current density ($A.m^{-2}$)

$\mathbf{a_i}$= specific surface area ($m^2.m^{-3}$)

R= gas constant ($J.mol^{-1}.K^{-1}$)

F= Faraday constant ($A.s.mol^{-1}$)

The quantity given by equation (6.13) provides the coupling between all the variables since the source terms are given in terms of reaction rate.

$$S_{H_2} = j\frac{M_{H_2}}{2F} \quad \textbf{(6.14)}$$

$$S_{O_2} = j\frac{M_{O_2}}{4F} \quad \textbf{(6.15)}$$

$$S_{H_2O} = -j\frac{M_{H_2O}}{2F} \quad \textbf{(6.16)}$$

$$S_{rxn} = -j\left(\emptyset_e - \emptyset_s - \frac{T\Delta S}{nF}\right) \quad \textbf{(6.17)}$$

The only source term that is not shown in terms of j is the ohmic heating term; nevertheless, it does not depend on the local current densities.

$$S_{ohm} = \frac{i_s^2}{\sigma_s^{eff}} + \frac{i_e^2}{\sigma_e^{eff}} \quad \textbf{(6.18)}$$

6.3.3. Cathode

6.3.3.1. Flow Channels: Maxwell-Stefan Mass Balances (Conservation of Species)

Three species, O_2, N_2 and H_2O, are taken into consideration in the cathode side flow channels. The multicomponent diffusion and convection in flow channels are described by the Maxwell-Stefan equation. This equation solves for the fluxes in terms of mass fraction. The equation for the Maxwell-Stefan multicomponent diffusion [2, 33-36, 41]:

$$\frac{\partial}{\partial t}\rho\omega_i + \nabla\left[-\rho\omega_i\sum_{j=1}^{N} D_{ij}\left\{\frac{M}{M_j}\left(\nabla\omega_j + \omega_j\frac{\nabla M}{M}\right) + (x_j - \omega_j)\frac{\nabla p}{p}\right\} + \omega_i\rho\boldsymbol{u} + D_i^T\frac{\nabla T}{T}\right] = R_i \quad \textbf{(6.19)}$$

where:

ω: mass fraction

p: pressure (Pa)

T: (cell) temperature (K)

u: velocity vector (m/s)

ρ: density of the mixture of the gas phase (kg/m^3)

D_{ij} : Maxwell-Stefan diffusion coefficient (m^2/s)

R_i: reaction rate ($kg/(m^3.s)$)

x: mole fraction

M: molecular (molar) mass (kg/mol)

i or j: These subscripts represent each species of oxygen, water and nitrogen.

It is assumed that temperature-driven diffusion which sets the source term R to zero is insignificant. Therefore, the reaction rate is zero in the flow channel.

Density of the mixture of the gas phase is a function of mixture components and is described by the equation:

$$\rho = (p/RT)\sum_i M_i\ x_i \tag{6.20}$$

where:

R: universal gas constant (8.314 J/(mol.K))

The mass transport is described by using Darcy's Law that describes the flow rate:

$$\nabla\left\{-\rho\omega_1\ \sum_k\left[D_{1k}\left(\nabla \mathrm{x_k} + (\mathrm{x_k} - \omega_k)\left((\nabla_\mathrm{p})/\mathrm{p}\right)\right)\right]\right\} = -(\rho \boldsymbol{u}.\nabla\omega_1) \tag{6.21}$$

$$\nabla\left\{-\rho\omega_2\ \sum_k\left[D_{2k}\left(\nabla \mathrm{x_k} + (\mathrm{x_k} - \omega_k)\left((\nabla_\mathrm{p})/\mathrm{p}\right)\right)\right]\right\} = -(\rho \boldsymbol{u}.\nabla\omega_2) \tag{6.22}$$

On the cathode side, mass transport equations are solved for two species, because the third species can always be obtained from the mass balance equation:

$$\omega_3\ = 1 - \omega_1\ - \omega_2 \tag{6.23}$$

where:

1: for oxygen,

2: for water,

3: for nitrogen

6.3.3.2. Gas Diffusion Layer And Catalyst Layer: Darcy's Law And Mass Conservation Equation (Porous Media Fluid Flow)

Continuity equation gives the gas velocity [1, 2, 33-36, 41]:

$$\nabla.(\rho \boldsymbol{u}) = 0 \tag{6.24}$$

where:

u: gas velocity (m/s)

The pressure gradient, the viscosity of the fluid and the structure of the porous media determine the velocity vector according to the Darcy's Law for porous media:

$$\boldsymbol{u} = -\frac{k_p}{\eta}\nabla p \tag{6.25}$$

where:

k_p: electrode's permeability (m^2)

η: gas's viscosity (Pa.s)

The mixture density of the gas phase is given by the ideal gas relation:

$$\rho = (p/RT)\sum_i M_i\ x_i \tag{6.26}$$

The pressure at the outlets and inlets are:

$$p = p_{c,in}\ (\text{at inlet}) \tag{6.27}$$

$$p = p_{ref} \ (at\ outlet) \tag{6.28}$$

The velocity of gas is determined from the total mass flow that is given by the electrochemical reaction rate at the electrode boundary:

$$-\boldsymbol{n}.\boldsymbol{u}\boldsymbol{I}_{\boldsymbol{cathode}} = \frac{j_{cathode}}{\rho F}\left[\frac{M_{O_2}}{4} + \left(\frac{1}{2} + \lambda_{H_2O}\right) M_{H_2O}\right] \tag{6.29}$$

Gas flow velocity is determined by the Darcy's Law. The total mass conservation is preserved in the cathode gas backing with this given boundary condition.

6.4. Solutions of the Governing Equations

COMSOL Multiphysics Software Package is used for solving the equations of the two dimensional mathematical model of the high temperature polymer electrolyte fuel cell membrane having a PBI based membrane since these governing equations are coupled equations to be solved simultaneously and contain nonlinearities that are hard to be solved analytically.

6.5. Results and Discussion

Using the computational modeling, graphs were obtained to show the behavior of the fuel cell membrane in PEMFC.

Figure 6.2 shows the gas velocity distribution. Figure 6.3 shows current density distribution. Figure 6.4 and 6.5 show mass fractions of hydrogen and oxygen, respectively. Figure 6.6 and 6.7 show mass fractions of water on the anode side and the cathode side, respectively. Figure 6.8 shows current density distribution on the membrane.

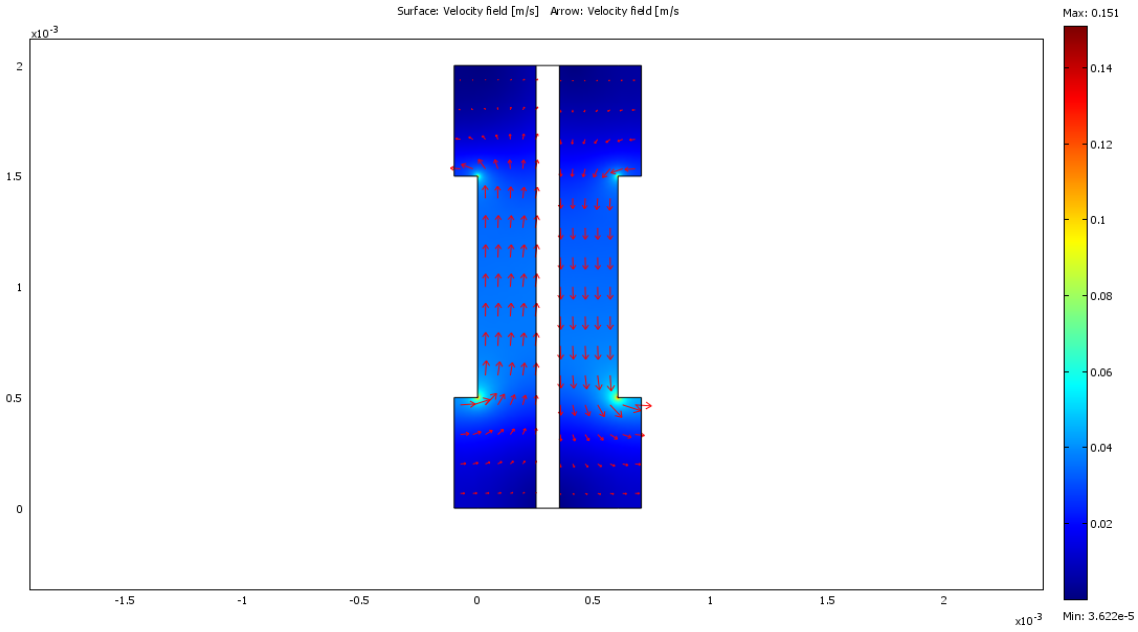

Figure 6.2 Velocity field

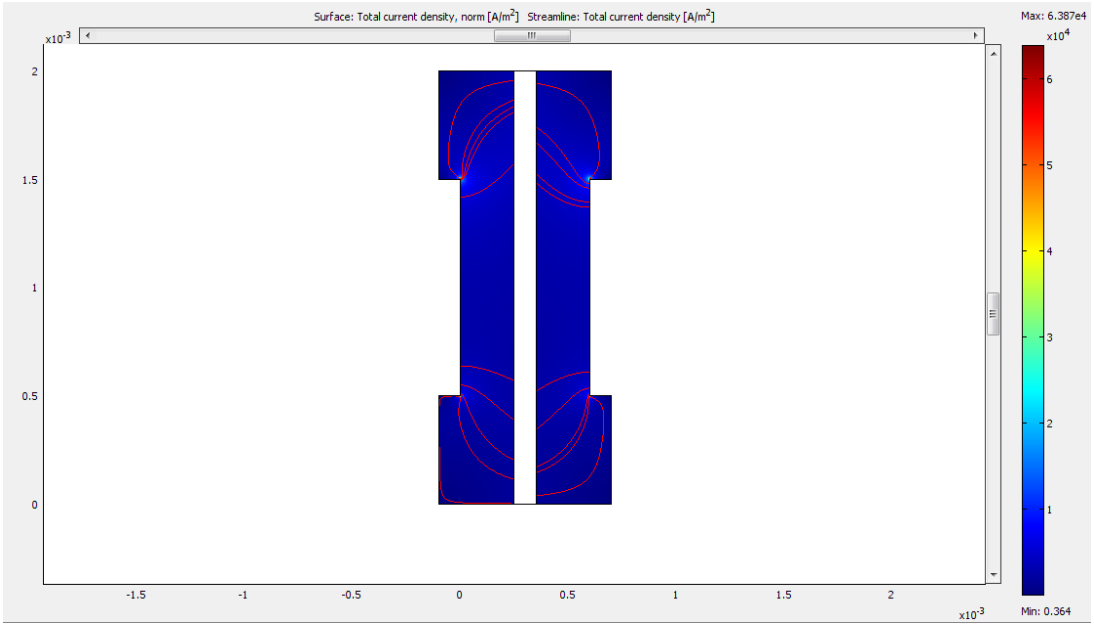

Figure 6.3 Total current density

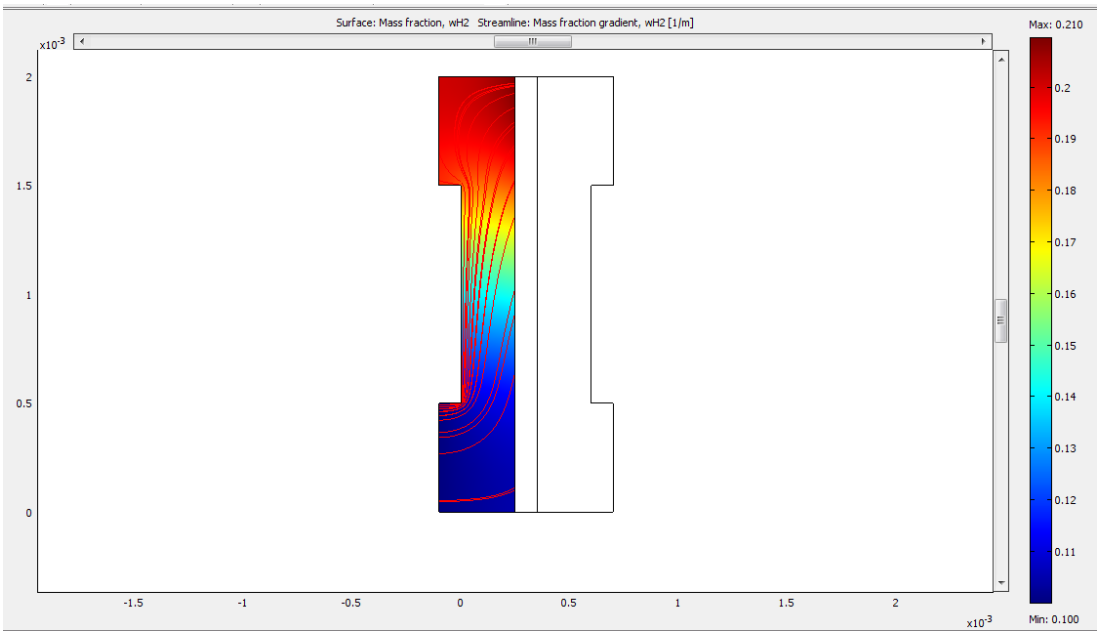

Figure 6.4 Mass fraction of hydrogen on the anode side

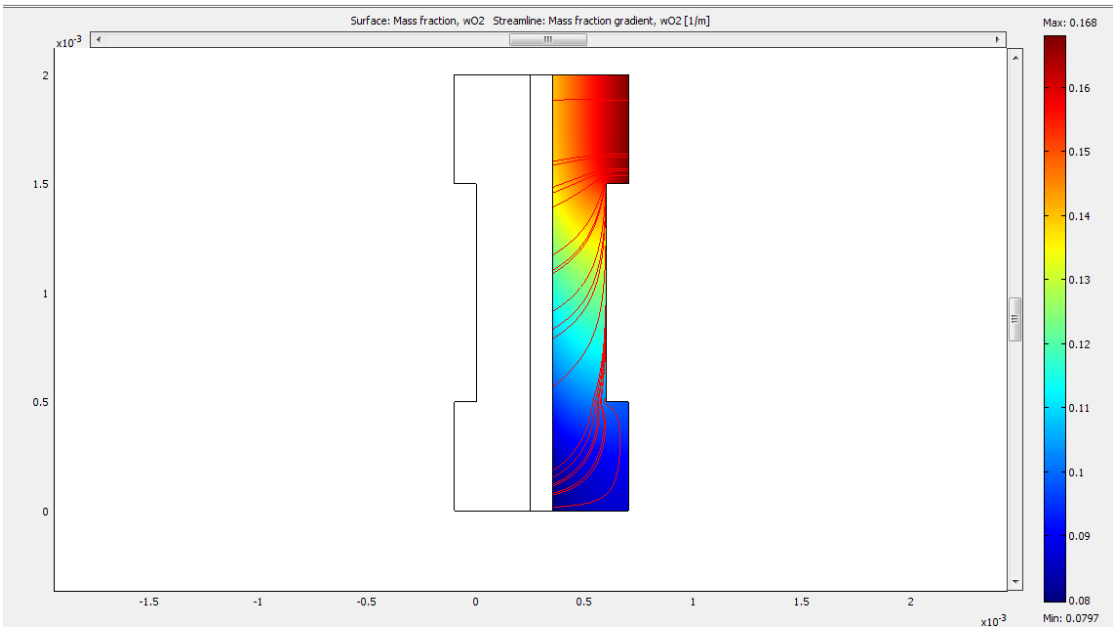

Figure 6.5 Mass fraction of oxygen on the cathode side

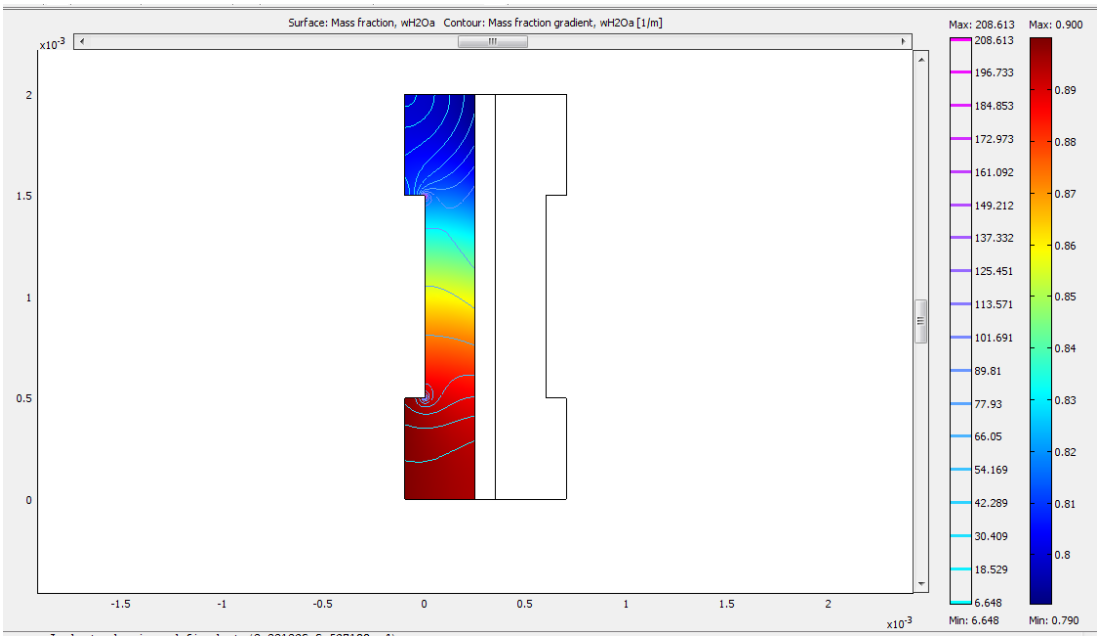

Figure 6.6 Mass fraction of water on the anode side

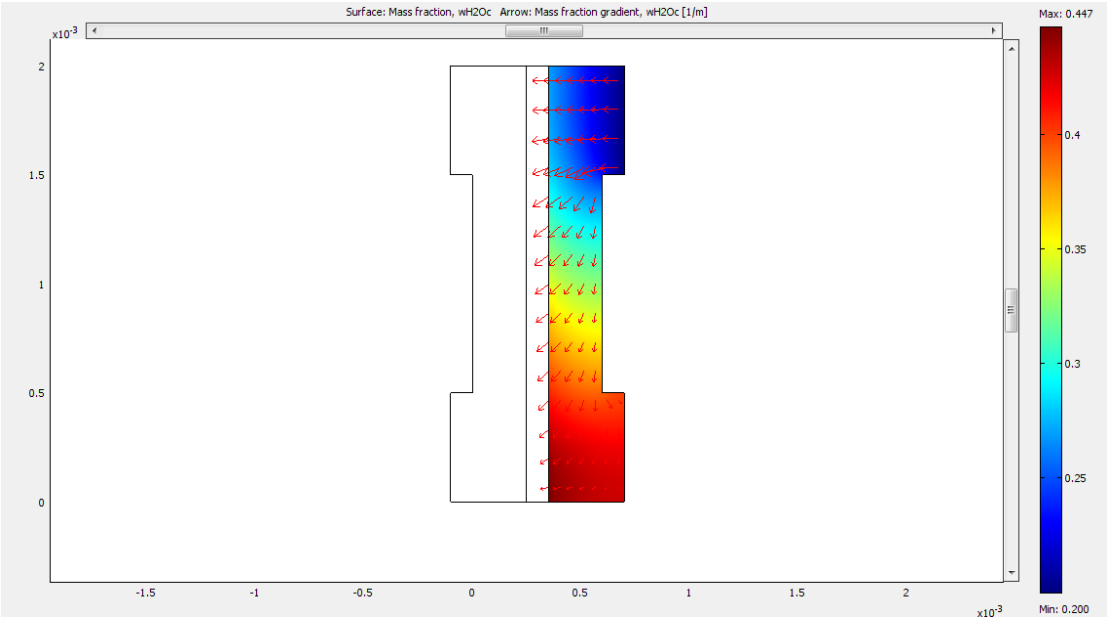

Figure 6.7 Mass fraction of water on the cathode side

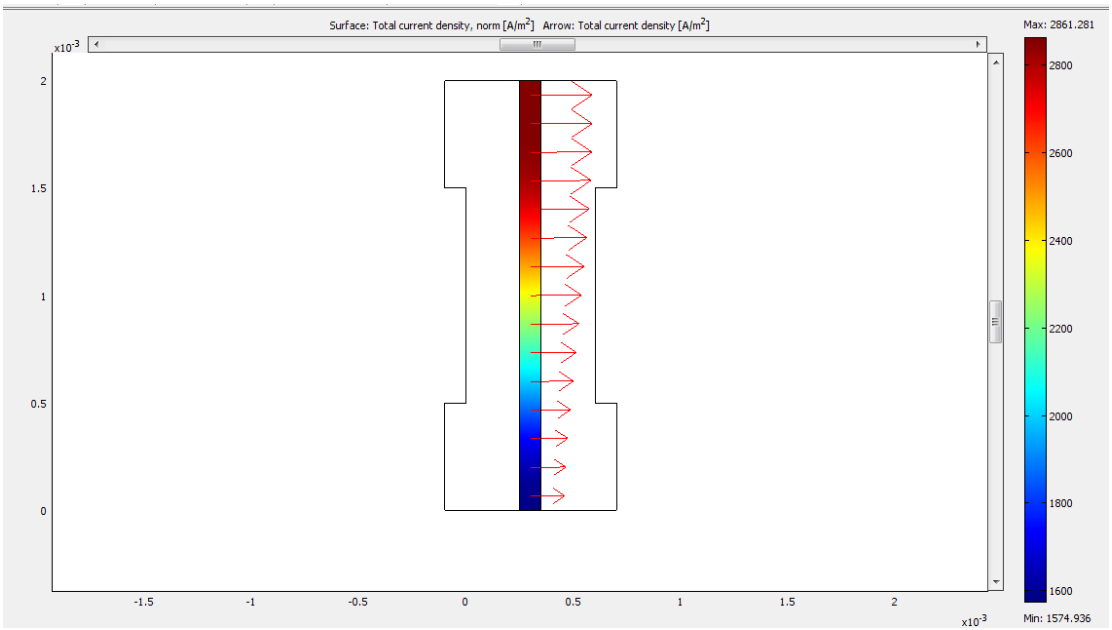

Figure 6.8 Total current density on the membrane

CHAPTER 7

CONCLUSIONS AND RECOMMENDATIONS

With the increasing temperature and winding speed, the thickness of the films decreases; however, with the increasing screw motor speed film thickness increases. With the increasing temperature tear strength becomes higher in machine direction (MD); however tear strength decreases in cross direction (CD). With the increasing screw motor speed tear strength of the films did not show any specific trend in MD; however, tear strength of the films in CD increases. With the increasing winding speed the tear strength of the films decreases in MD; however, the data did not show any specific trend in CD. As the temperature increased, tensile strength increased in MD. With increasing screw motor speed tensile strength of the films increases in MD; however, tensile strength of the films decreases in CD. With increasing winding speed the tensile strength of the films increases in MD; however, tensile strength of the films decreases in CD.

Nanoclay reinforced films having only 1% nanoclay content have more homogeneous nanoclay dispersion than the films having 3% nanoclay content. Screw speed was increased for the films having 5% nanoclay content in order to obtain a film structure since for 5% nanoclay content, the films could not be drawn with the same screw speed that was used for the films having 1% and 3% nanoclay content. Therefore, since the screw speed was increased, shear stress increased. This caused the polymer and the nanoclay mix more homogeneously by making the morphological structure of the films having 5% nanoclay content more homogeneous.

According to the differential scanning calorimetry (DSC) results the melting points of the nanoclay reinforced films slightly increase as their nanoclay contents increase from 1% to 5%. Tensile tests showed that as the nanoclay contents of the nanoclay reinforced films increase, the extension of the films decreases. No specific result could be obtained about the effect of the compatibilizer content on tensile strength of the nanoclay reinforced films. Nanoclay reinforced films having only 1% nanoclay content have higher tear strength than the films having 3% nanoclay content. Since the screw speed was increased for the films having 5% nanoclay content in order to obtain a film structure, the films, having 5% nanoclay content, gained higher tear strength. Burst strength results show that as the nanoclay content of the nanoclay reinforced films increases from 1% to 5%, the extension of the films decreases. Nanoclay reinforced films having only 1% nanoclay content have higher burst strength than the films having 3% nanoclay content.

The following is recommended for any future work on this subject**:**

Composite membranes for fuel cell applications can be manufactured by adding some materials to the structure of the polymer electrolyte membrane such as:

- Titanya

Titanya is a metal oxide and an inorganic material having hygroscopic properties. By adding titanya into the structure of polymer electrolytes, water retention ability of the membranes can be enhanced. Titanium oxide is a good hydrophilic filler candidate to polymer electrolytes since it maintains the membrane hydration. Addition of titanium dioxide to the composite membrane structures will enhance water uptake, ion exchange capacity (IEC), conductivity and

electrochemical performance of membranes [41]. Therefore, it is possible to produce a self humidifying membrane by adding titanium dioxide nanoparticles to the membrane structure.

- Phosphotungstic Acid

Phosphotungstic acid, which has a molecular formula of $H_3PW_{12}O_{40,}$ is a heteropoly acid (HPA). It has different names, one of the other names is tungstophosphoric acid (TPA). Tungstophosphoric acid is thermally stable up to 400°C. It is the strongest of heteropolyacids which can be qualified as super acid. Phosphotungstic acid (PWA) is a very conductive material in the crystalline form having 29 water molecules per molecule. Because of the high number of water molecules in their reticular structure they exhibit very high proton conductivity.

Since it is obvious that the perfluorinated membranes cannot be used at severe fuel cell operating conditions, novel membranes, having composite or sandwich structures that can withstand high temperature conditions without losing any of their properties, can be designed and manufactured.

REFERENCES

1. O'Hayre, R.P., Cha, S.W., Colella, W., and Prinz, F.B., *"Fuel Cell Fundamentals"*, John Wiley & Sons, Inc., New York, USA, 2006.

2. Barbir, F., *"PEM Fuel Cells Theory And Practice"*, Elsevier Science And Technology Books, 2005.

3. Ramani, V., Kunz, H.R., and Fenton, J.M., *"Effect of particle size reduction on the conductivity of Nafion®/phosphotungstic acid composite membranes"*, Journal of Membrane Science 2005, 266, 110-114.

4. Devanathan, R., "Recent developments in proton exchange membranes for fuel cells", Energy and Environmental Science 2008, 1, 101-119.

5. Souzy, R., and Ameduri, B., "*Functional fluoropolymers for fuel cell membranes"*, Progress in Polymer Science 2005, 30, 644–687.

6. Hu, J., Zhang, H., Zhai, Y., Liu, G., and Yi, B., *"500 h Continuous aging life test on PBI/H_3PO_4 high-temperature PEMFC"*, International Journal of Hydrogen Energy, 2006, 31, 1855-1862.

7. Kim, H.J., and Lim, T.H., *"PBI derivatives: polymer electrolyte fuel cell membrane for high temperature operation",* Journal of Ind. Eng. Chem., 2004, 10, 7, 1081-1085.

8. Li, M.Q., Shao, Z.G., and Scott,K., *"A high conductivity $Cs_{2.5}H_{0.5}PMo_{12}O_{40}$ / polybenzimidazole (PBI) / H_3PO_4 composite membrane for proton-exchange membrane fuel cells operating at high temperature",* Journal of Power Sources, 2008, 183, 69–75.

9. Zhai, Y., Zhang, H., Zhang, Y., and Xing, D., *"A novel H_3PO_4/Nafion®-PBI composite membrane for enhanced durability of high temperature PEM fuel cells",* Journal of Power Sources 2007, 169, 259–264.

10. Aparicio, M., Mosa, J., Etienne, M., and Duran, A., *"Proton conducting methacrylate-silica sol-gel membranes containing tungstophosphoric acid",* Journal of Power Sources 2005, 145, 231–236.

11. en.wikipedia.org/wiki/Plastics_extrusion, (access date: 06/01/2009)

12. Christie, A., *"Polypropylene crystallization effects on film forming",* www.optexprocesssolutions.com, (access date: 09/ 01/ 2009).

13. Chung, C.I., *Extrusion of polymers, theory and practice*, Hanser Verlag, (2000).

14. ASTM, Standard Test Method for Tensile Properties of Thin Plastic Sheeting, Designation D 882-02, vol. 8.01. American Society for Testing and Materials, Philadelphia, PA (2002).

15. ASTM, Standard Test Method for Tear-Propagation Resistance (Trouser Tear) of Plastic Film and Thin Sheeting by a Single-Tear Method, Designation D 1938-06, vol. 8.01. American Society for Testing and Materials, Philadelphia, PA (2006).

16. ASTM, Standard Test Method for Bursting Strength of Fabrics Constant-Rate-of-Extension (CRE) Ball Burst Test, Designation D 6797-02, vol. 7.01. American Society for Testing and Materials, Philadelphia, PA (2002).

17. Sadeghi, F., Ajji, A. and Carreau, P.J., *"Analysis of microporous membranes obtained from polypropylene films by stretching",* Journal of Membrane Science, 2007, 292, 62-71.

18. Tang, X., Alavi, S. and Herald T.J., "*Efects of plasticizers on the structure and properties of starch-clay nanocomposite films*", Carbohydrate Polymers, 2008, 74, 552-558.

19. Thostenson, E.T., Li, C. and Chou, T.W., "Nanocomposites in context", Composites Science and Technology, 2005, 65, 491-516.

20. http://www.scprod.com/ (access date: 02/01/2010)

21. www2.dupont.com (access date: 02/01/2010)

22. www.leistritz.com (access date: 02/01/2010)

23. http://www.instron.us/wa/products/universal_material/5560.aspx (access date: 02/01/2010)

24. http://www.testingmachines.com/pdf/49-70-series-micrometers.pdf (access date: 02/01/2010)

25. http://www.speciation.net/Appl/Techniques/technique.html?id=663 (access date: 02/01/2010)

26. http://www.emsdiasum.com/microscopy/products/equipment/carbon_coater.aspx (access date: 02/01/2010)

27. Leikin, A.Y., Bulycheva, E.G., Rusanov, A.L., and Likhachev, D.Y., *"High-temperature proton-exchange membranes based on polymer-acid complexes",* Polymer Science Ser., 2006, B 48 , 5–6.

28. Seland,F., Berning,T., Borresen, B., and Tunold, R., *"Improving the performance of high-temperature PEM fuel cells based on PBI electrolyte"*, Journal of Power Sources, 2006, 160, 27–36.

29. Lobato, J., Canizares, P., Rodrigo, M.A., Linares, J.J., and Manjavacas, G., *"Synthesis and characterization of poly[2,2-(m-phenylene)-5,5-bibenzimidazole] as polymer electrolyte membrane for high temperature PEMFCs",* Journal of Membrane Science, 2006, 280, 351-362.

30. http://www.sono-tek.com/ (access date: 02/01/2010)

31. http://www.ijfisnar.com (access date: 02/01/2010)

32. He, R., Li, Q., Xiao, G., and Bjerrum, N.J., *"Proton conductivity of phosphoric acid doped polybenzimidazole and its composites with inorganic proton conductors",* Journal of Membrane Science, 2003, 226, 169-184.

33. Shi, Z., and Wang, X., "*Two-dimensional PEM fuel cells modeling using COMSOL multiphysics*", COMSOL conference 2007, Boston, USA.

34. Yesilyurt, S., "*Three-dimensional simulations of transient response of PEM fuel cells*", ASME international mechanical engineering congress and exhibition, November 11-15 2007, Seattle, Washington, USA.

35. Siegel, C., "*Review of computational heat and mass transfer modeling in polymer electrolyte membrane (PEM) fuel cells*", Energy, 2008, 33, 1331-1352.

36. Cheddie, D., and Munroe, N., "*Modelling of high temperature PEM fuel cells using FEMLAB*", COMSOL conference 2005, Boston, USA.

37. Siegel, C., Bandlamudi, G. and Heinzel, A., "*Modelling polybenzimidazole/phosphoric acid membrane behavior in a HTPEM fuel cell*", COMSOL conference, 2008, Hannover.

38. Siegel, C., Bandlamudi, G. and Heinzel, A., "*Numerical simulation of a high-temperature PEM (HTPEM) fuel cell*", COMSOL conference, 2007, Grenoble.

39. Cheddie, D., and Munroe, N., "*Mathematical model of a PEMFC using a PBI membrane*", Energy Conversion and Management, 2006, 47, 1490-1504.

40. Grujicic, M., and Chittajallu, K.M., "*Design and optimization of polymer electrolyte membrane (PEM) fuel cells*", Applied Surface Science, 2004, 227, 56-72.

41. Sacca, A., Carbone, A., Passalacqua,E., D'Epifanio,A., Licoccia,S., Traversa,E., Sala,E., Traini,F., and Ornelas,R., "*Nafion-TiO_2 hybrid membranes for medium temperature polymer electrolyte fuel cells (PEFCs)"*, Journal of Power Sources, 2005, 152, 16–21.

APPENDICES

APPENDIX A: SEM Micrographs of Nanoclay Reinforced Films

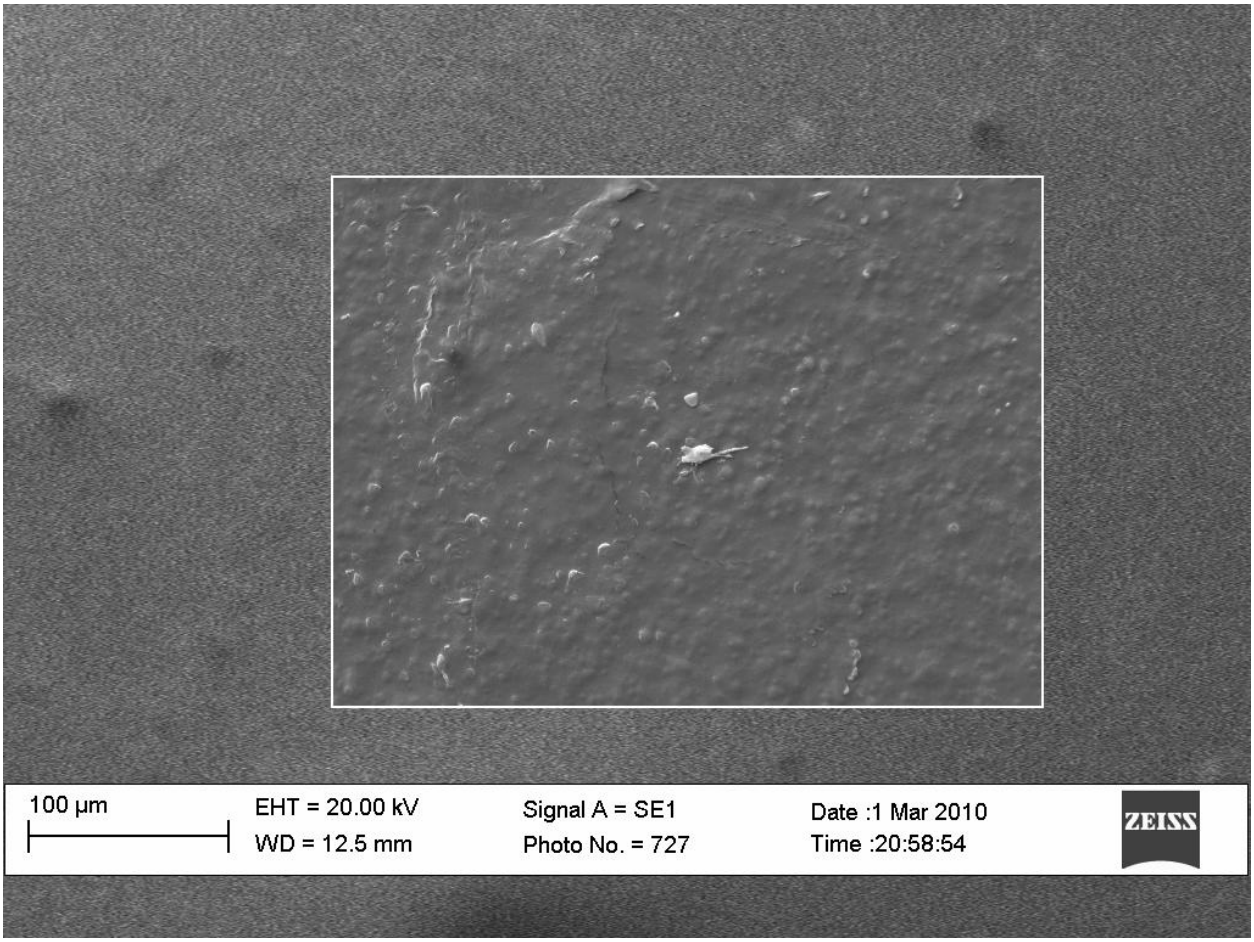

Figure A-1 Nanoclay dispersion in Film 1

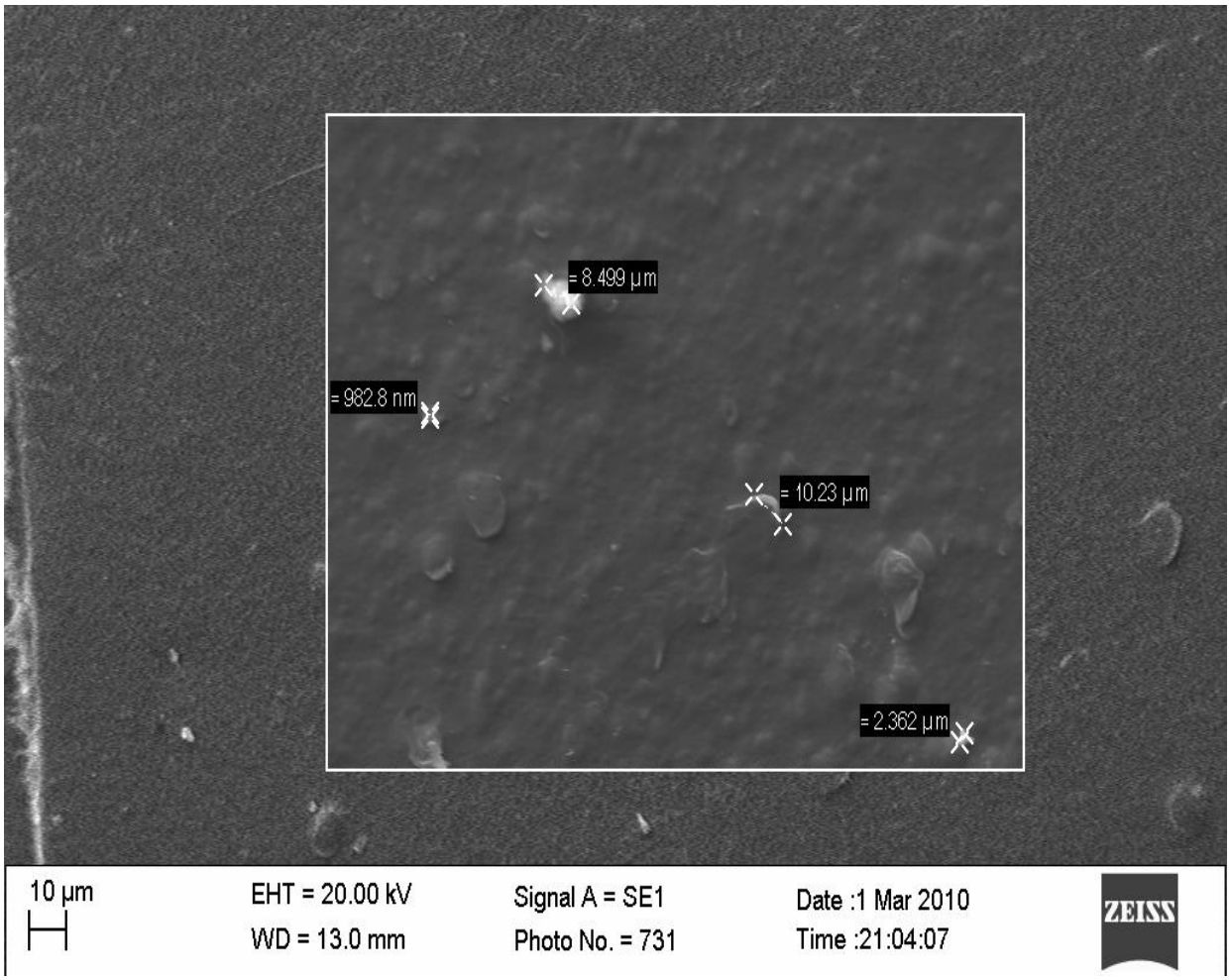

Figure A-2 Nanoclay dispersion in Film 2

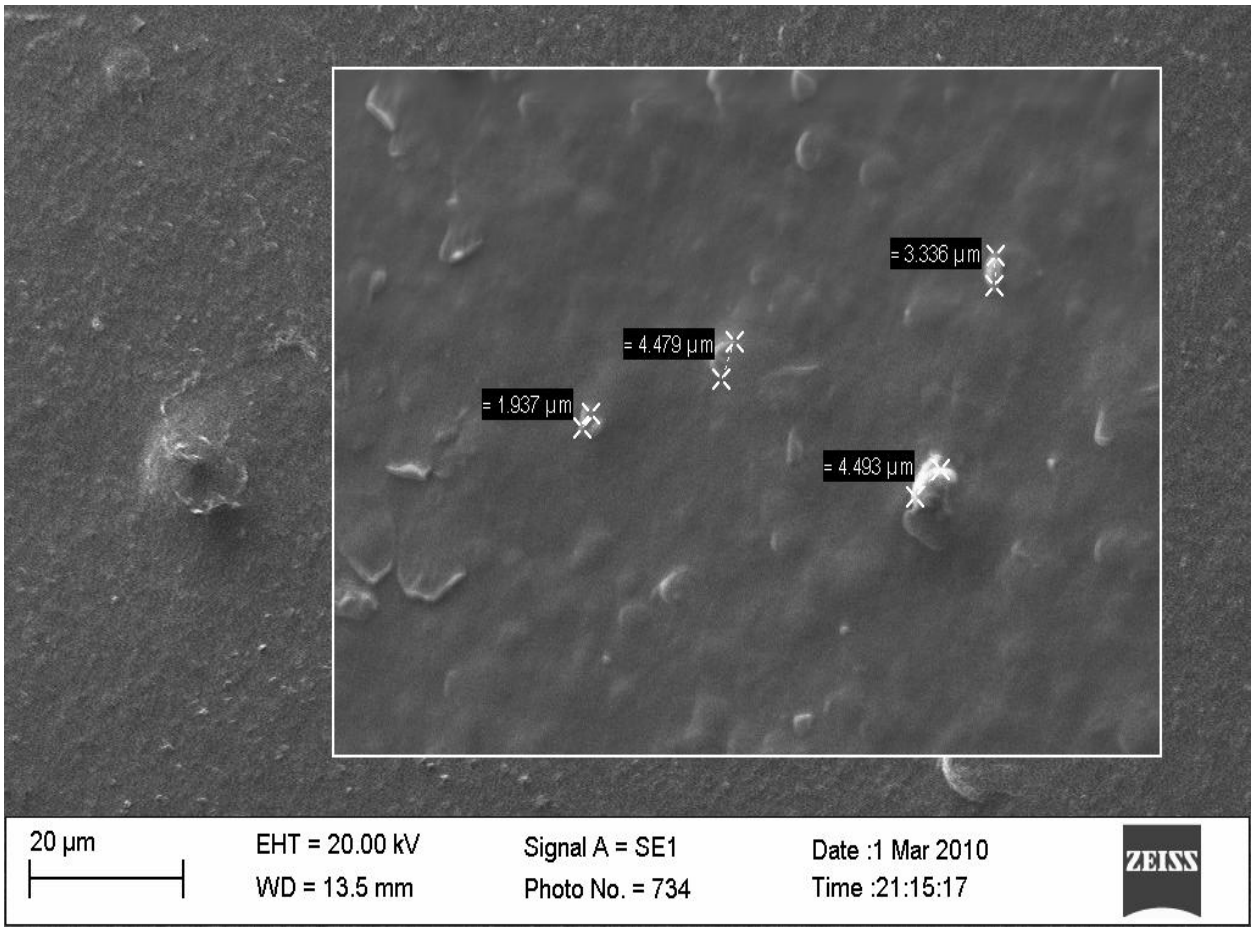

Figure A-3 Nanoclay dispersion in Film 3

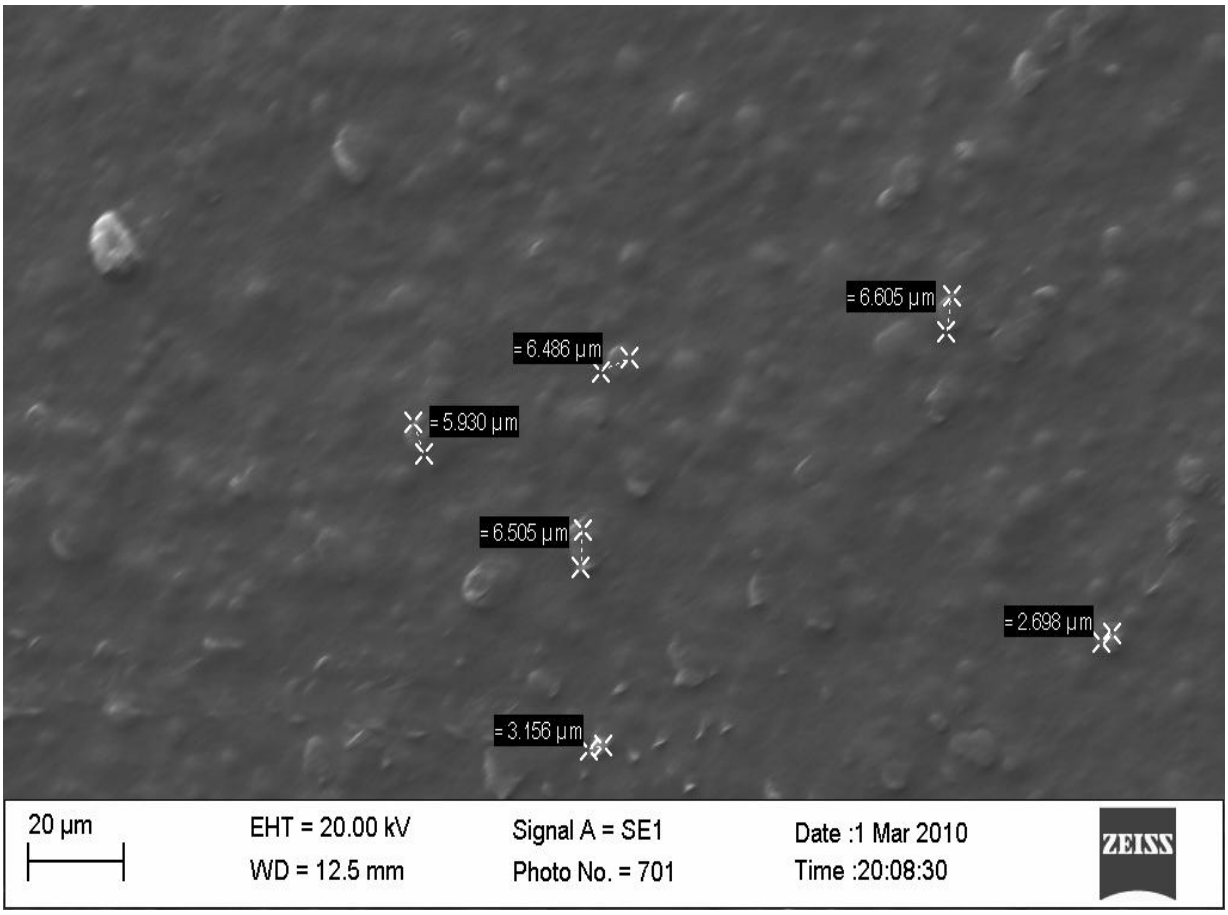

Figure A-4 Nanoclay dispersion in Film 4

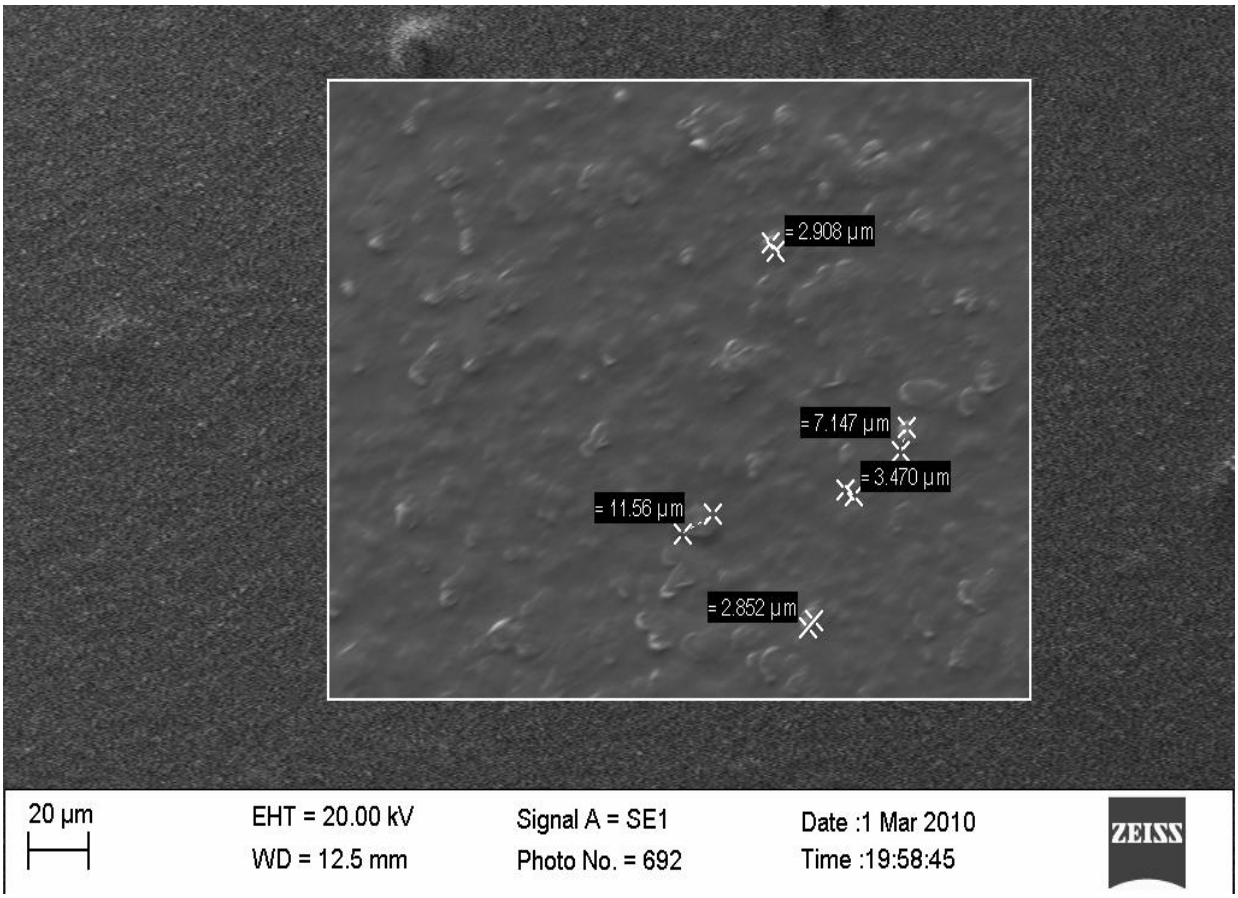

Figure A-5 Nanoclay dispersion in Film 5

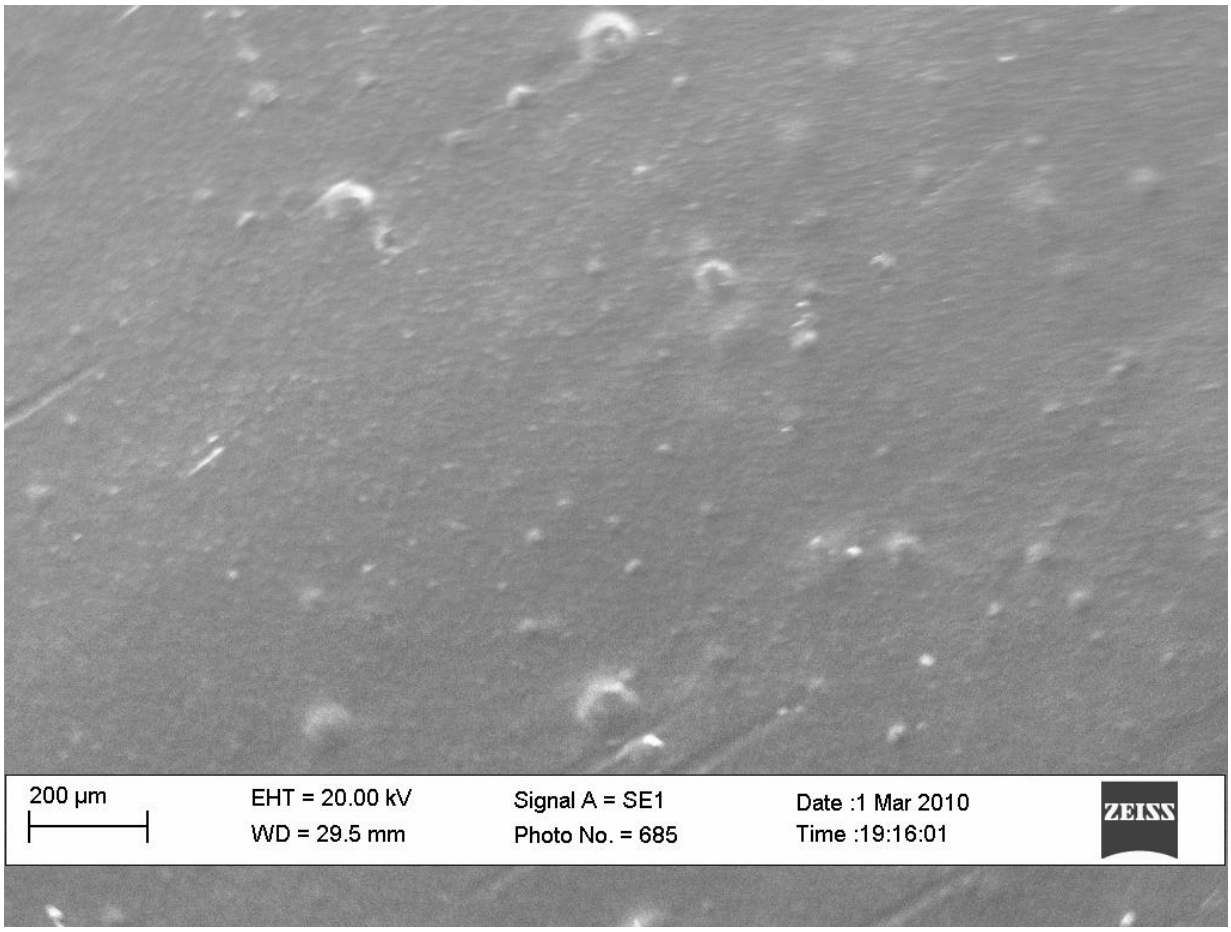

Figure A-6 Nanoclay dispersion in Film 6

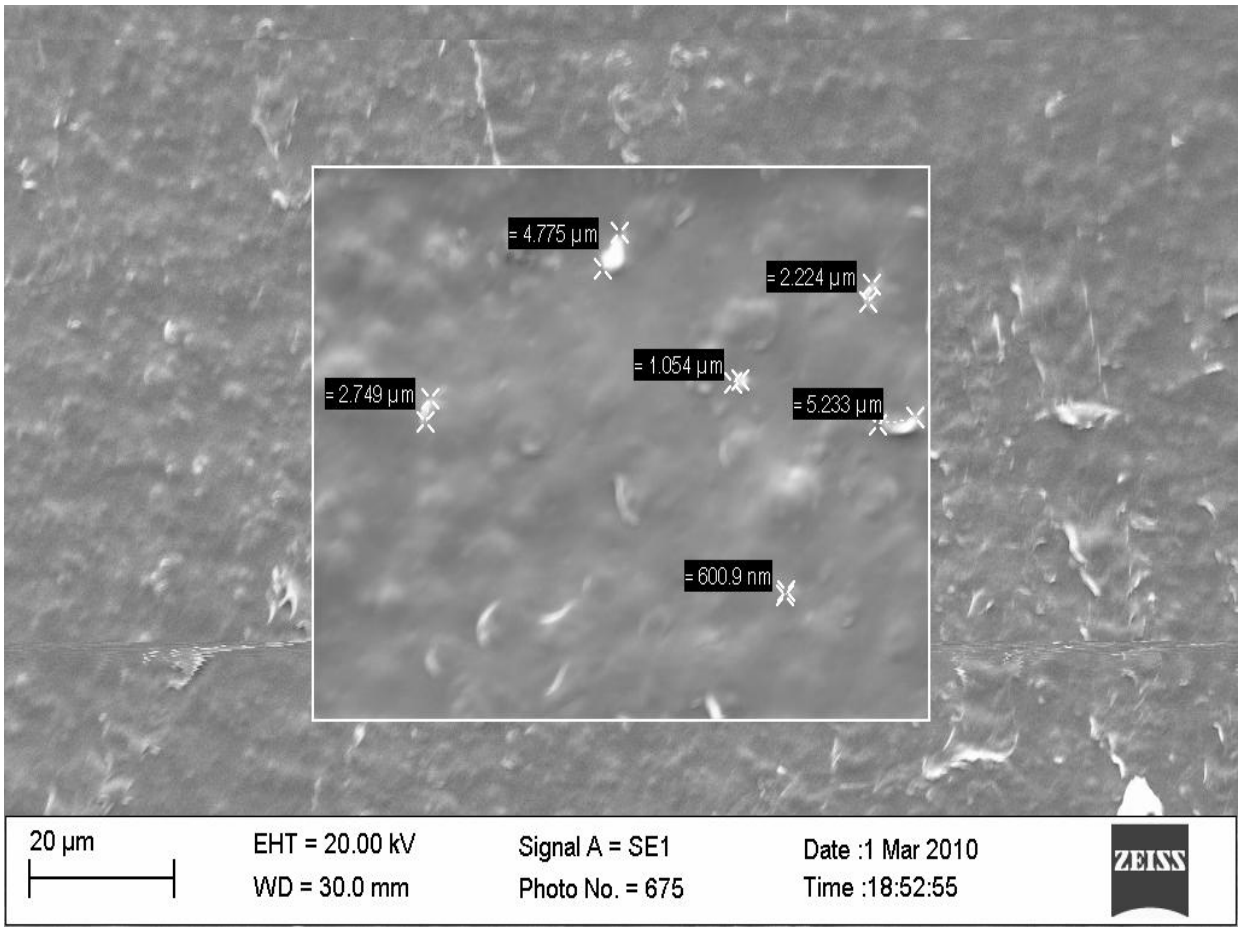

Figure A-7 Nanoclay dispersion in Film 7

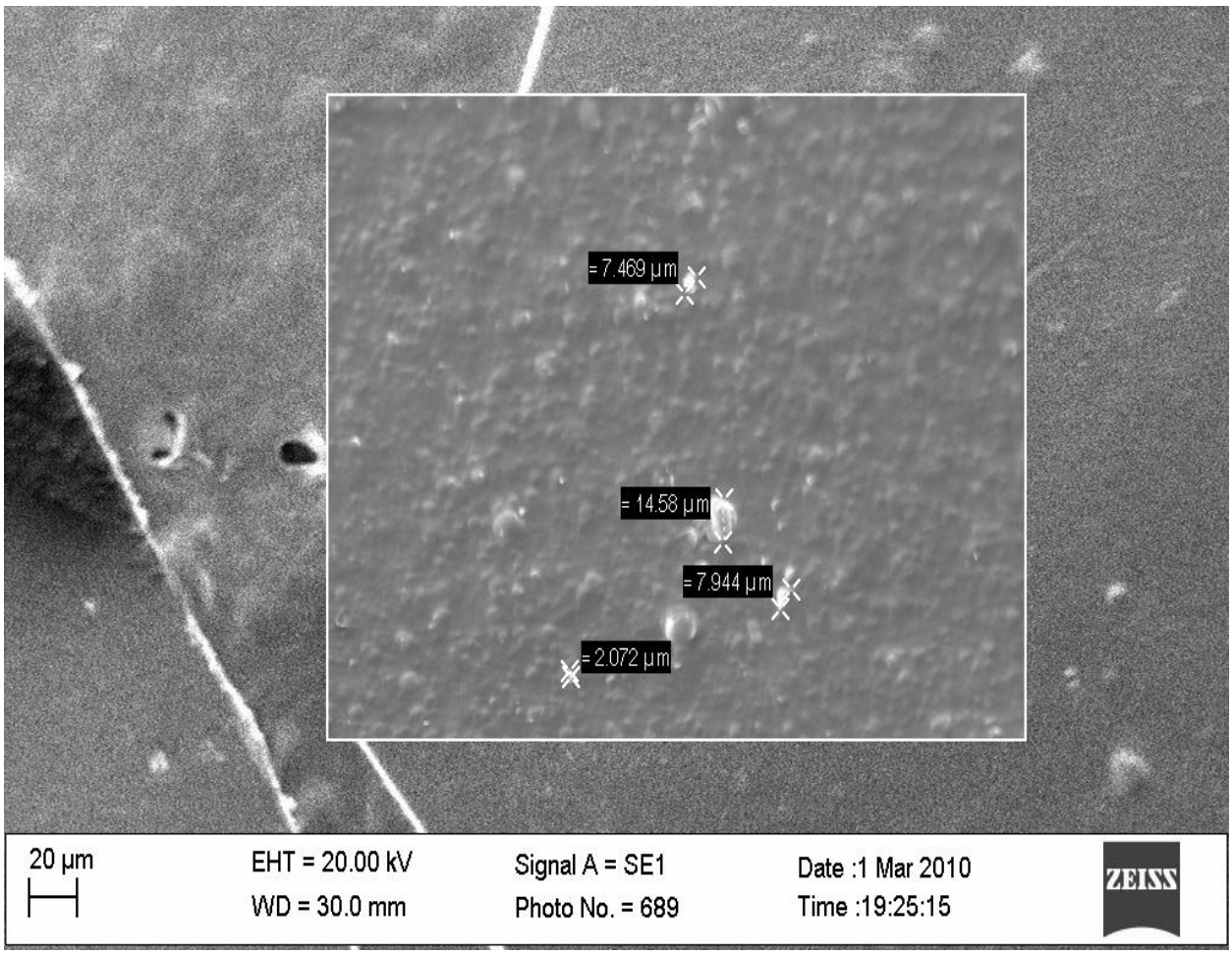

Figure A-8 Nanoclay dispersion in Film 8

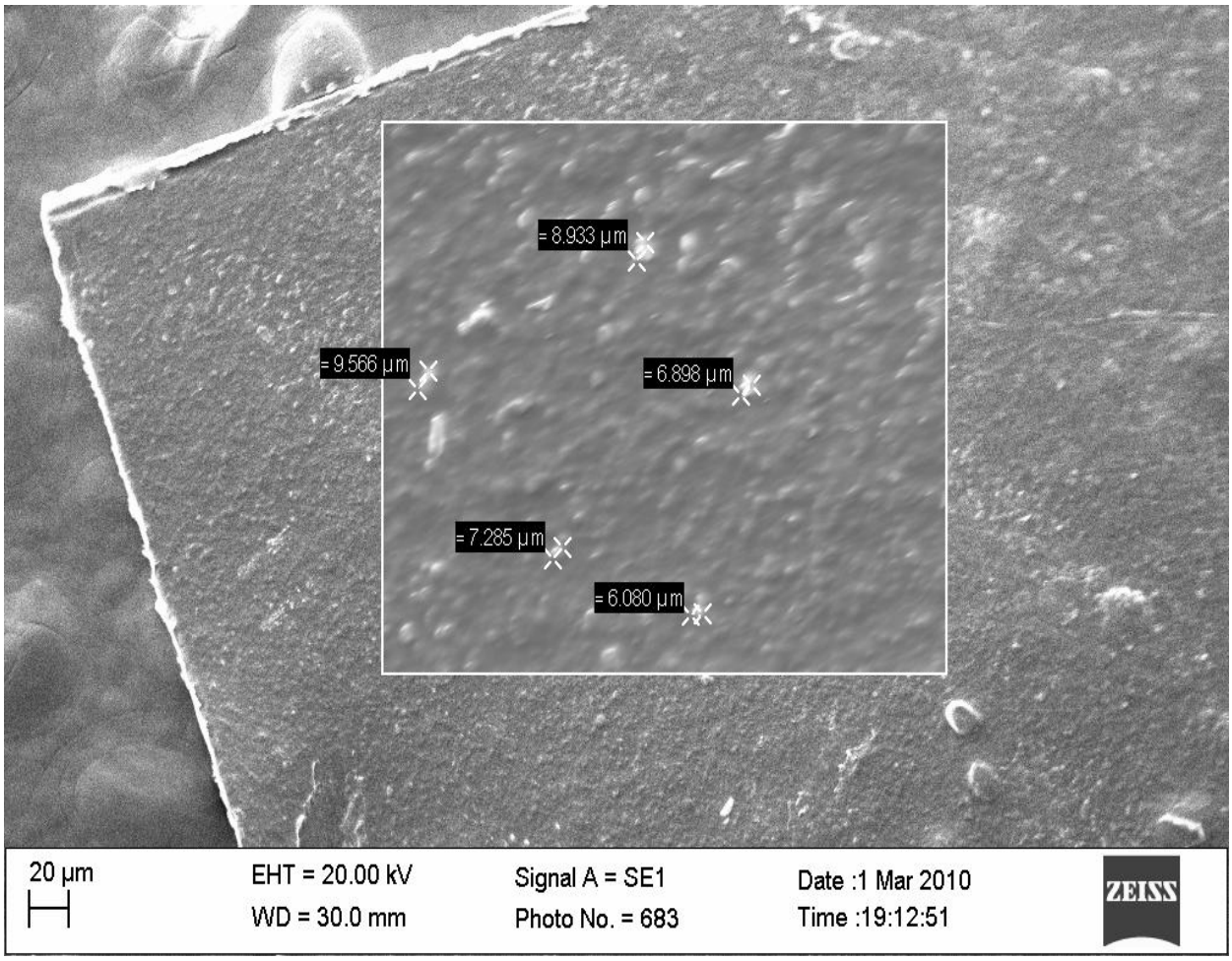

Figure A-9 Nanoclay dispersion in Film 9

APPENDIX B: Programs Written for the Dispensing Robot

Program 3

This program makes the dispensing robot draw a square by filling inside the square (Figure B-1).

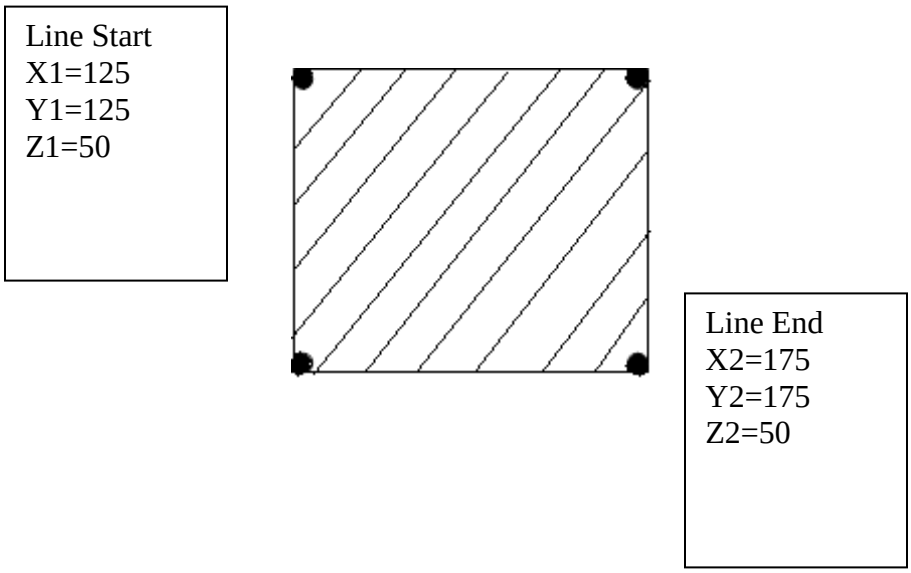

Figure B-1 Steps of program 3

Steps of the program are as follows:

1) Set up – Line Speed – Enter – 10 – Enter

   Set up – XY Move Speed – Enter – 10 – Enter

2) Enter (or Point) – Brush Area – Enter – Select (1 - Rectangle) – Width – 1 – Enter – 1.X 2.Y:1 (Rectangle) – Enter

3) Menu 2 – Numerical Move – Enter

X1= 125 Y1=125 Z1=50

4) Enter (or Point) – Line Start – Enter
5) Menu 2 – Numerical Move – Enter

   X2=175 Y2=175 Z2=50

6) Enter (or Point) – Line End – Enter
7) Enter (or Point) – End Program – Enter
8) Run

Program 4

This program makes the dispensing robot draw a square by filling inside the square two times calling the program 3 from its memory (Figure B-2).

Steps of the program are as follows:

1) Enter (or Point) – Call Program – Enter – Program 3 – Enter
2) Enter (or Point) – Call Program – Enter – Program 3 – Enter
3) Enter (or Point) – End Program – Enter
4) Run

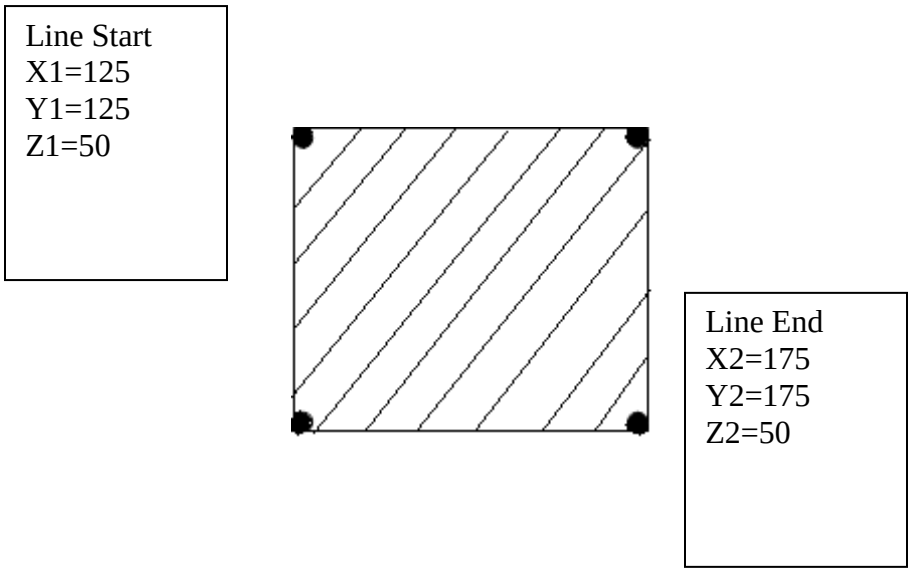

Figure B-2 Steps of program 4

Program 5

This program makes the dispensing robot draw a square by filling inside the square three times calling the program 3 from its memory (Figure B-3).

Steps of the program are as follows:

1) Enter (or Point) – Call Program – Enter – Program 3 – Enter
2) Enter (or Point) – Call Program – Enter – Program 3 – Enter
3) Enter (or Point) – Call Program – Enter – Program 3 – Enter
4) Enter (or Point) – End Program – Enter
5) Run

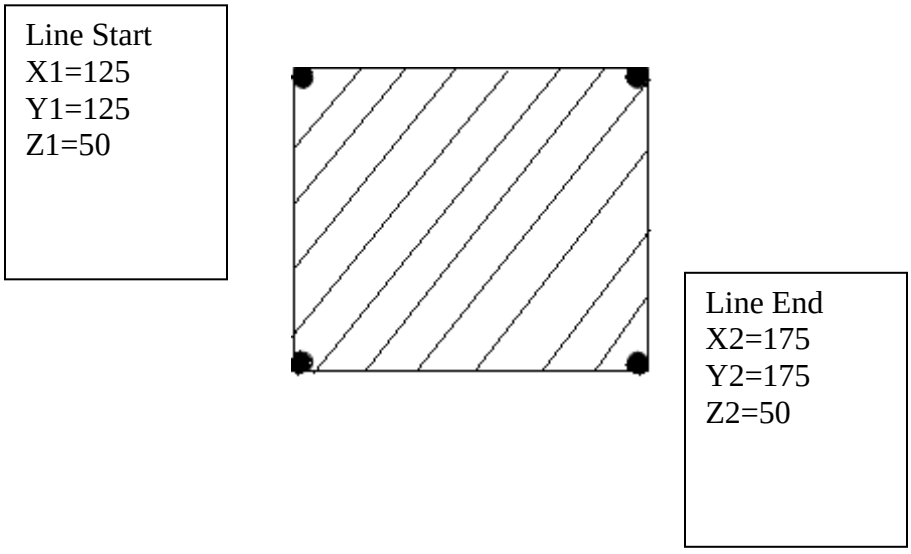

Figure B-3 Steps of program 5

Program 6

This program makes the dispensing robot draw a square by filling inside the square four times calling the program 3 from its memory (Figure B-4).

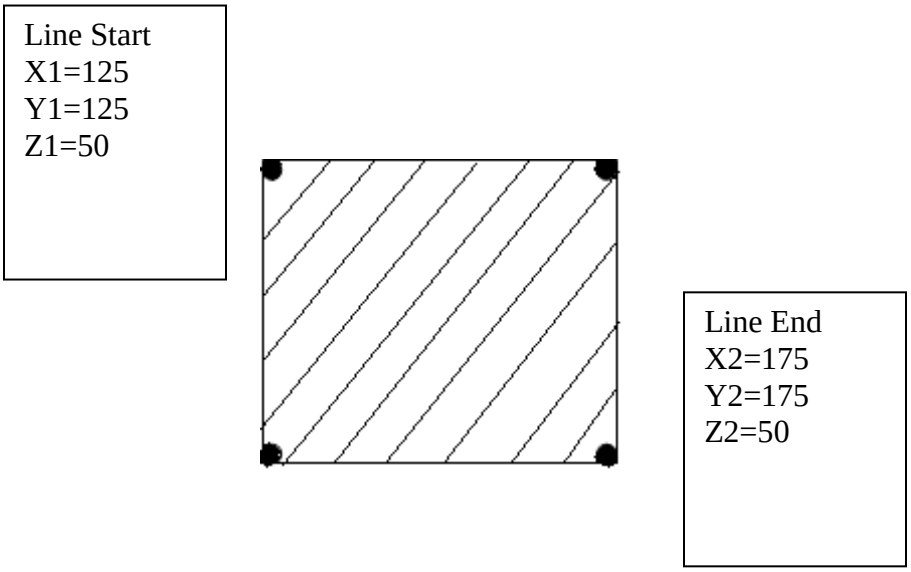

Figure B-4 Steps of program 6

Steps of the program can be seen below:

1) Enter (or Point) – Call Program – Enter – Program 3 – Enter
2) Enter (or Point) – Call Program – Enter – Program 3 – Enter
3) Enter (or Point) – Call Program – Enter – Program 3 – Enter
4) Enter (or Point) – Call Program – Enter – Program 3 – Enter
5) Enter (or Point) – End Program – Enter
6) Run

Program 7

This program makes the dispensing robot draw a square by filling inside the square five times calling the program 3 from its memory (Figure B-5).

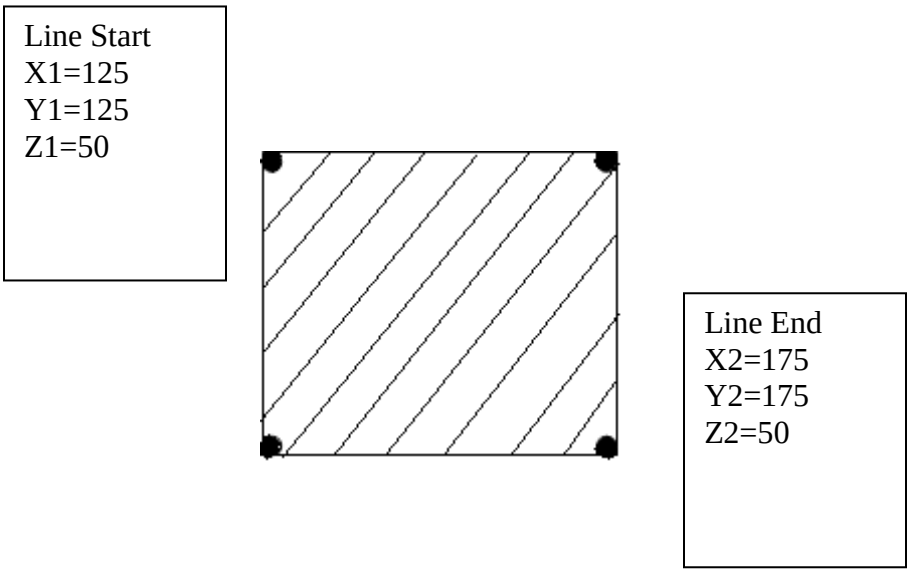

Figure B-5 Steps of program 7

Steps of the program can be seen below:

1) Enter (or Point) – Call Program – Enter – Program 3 – Enter
2) Enter (or Point) – Call Program – Enter – Program 3 – Enter
3) Enter (or Point) – Call Program – Enter – Program 3 – Enter
4) Enter (or Point) – Call Program – Enter – Program 3 – Enter
5) Enter (or Point) – Call Program – Enter – Program 3 – Enter
6) Enter (or Point) – End Program – Enter
7) Run

Program 8

This program makes the dispensing robot move by drawing a circle.

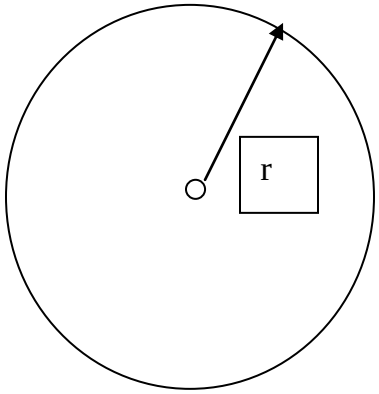

Figure B-6 Steps of program 8

Steps of the program:

1) Set up – Line speed – Enter – 30 – Enter

   Set up – XY move speed – Enter – 50 – Enter

2) Menu 2 – Numerical move – Enter

   X1=150 Y1=150 Z1=50

3) Enter (or point) – Circle – Enter

   Diameter – 200 – Enter

   Over angle – 0 – Enter

   Z lift select – (2 no) – Enter

4) Enter (or point) – End Program – Enter

5) Run

Program 9

This program makes the dispensing robot move by drawing two circles attached to each other.

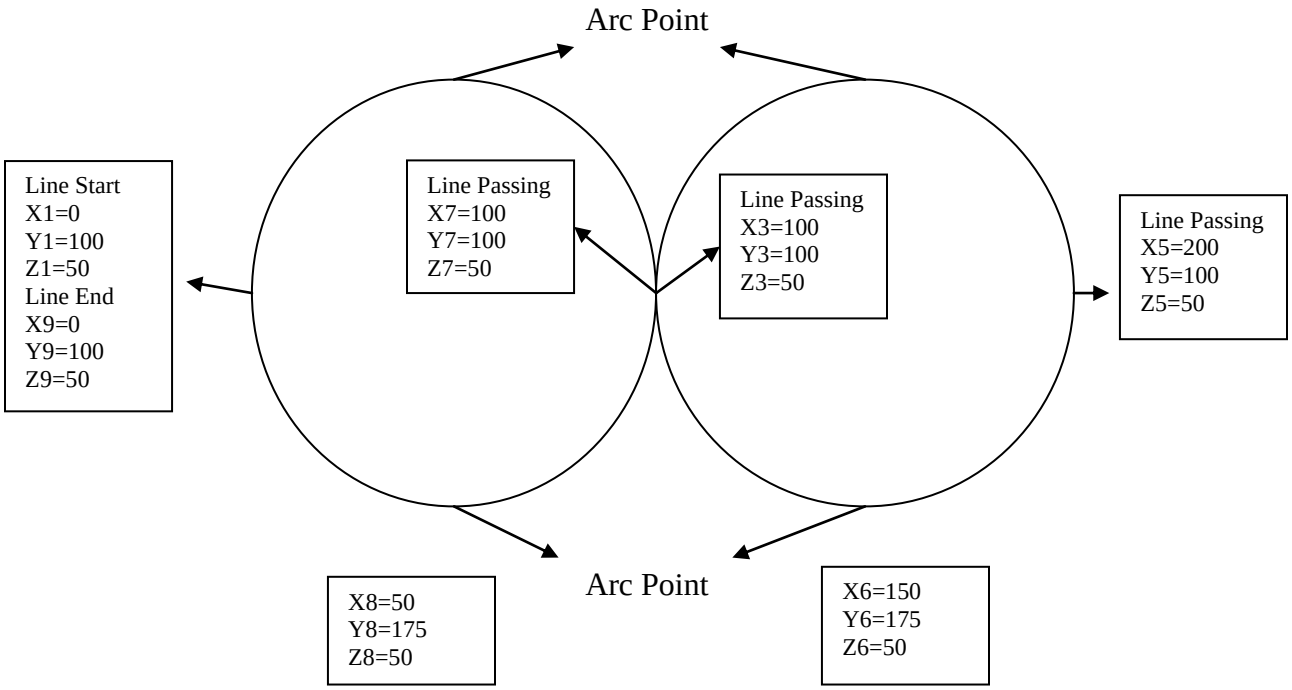

Figure B-7 Steps of program 9

Steps of the program:

1) Set up – Line speed – Enter – 5 – Enter

   Set up – XY move speed – Enter – 100 - Enter

2) Menu 2 – Numerical move – Enter

   X1=0 Y1=100 Z1=50

3) Enter (or point) – Line start – Enter

4) Menu 2 – Numerical Move – Enter

   X2=50 Y2=25 Z2=50

5) Enter (or point) – Arc point – Enter

6) Menu 2 – Numerical move – Enter

   X3=100 Y3=100 Z3=50

7) Enter (or point) – Line passing – Enter

8) Menu 2 – Numerical move – Enter

   X4=150 Y4=25 Z4=50

9) Enter (or point) – Arc point – Enter

10) Menu 2 – Numerical move – Enter

    X5=200 Y5=100 Z5=50

11) Enter (or point) – Line passing – Enter

12) Menu 2 – Numerical move – Enter

    X6=150 Y6=175 Z6=50

13) Enter (or point) – Arc point – Enter

14) Menu 2 – Numerical move – Enter

    X7=100 Y7=100 Z7=50

15) Enter (or point) – Line passing – Enter

16) Menu 2 – Numerical move – Enter

    X8=50 Y8=175 Z8=50

17) Enter (or point) – Arc point – Enter

18) Menu 2 – Numerical move – Enter

    X9=0 Y9=100 Z9=50

19) Enter (or point) – Line end – Enter

20) Enter – End Program – Enter

Program 10

This program makes the dispensing robot move by drawing a triangle.

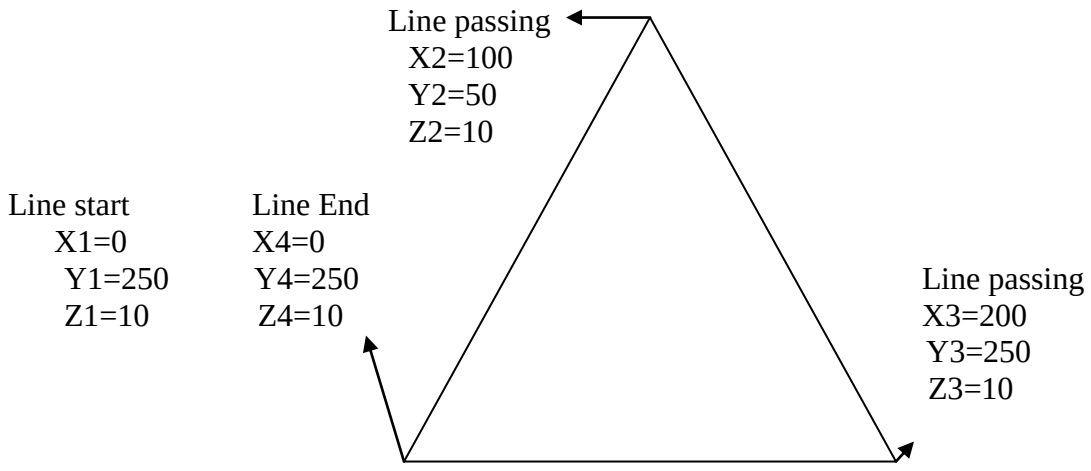

Figure B-8 Steps of program 10

Steps of the program:

1) Set up – Line speed – Enter – 5 – Enter

   Set up – XY move speed – Enter – 500 - Enter

2) Menu 2 – Numerical move – Enter

   X1=0 Y1=250 Z1=10

3) Enter (or point) – Line start – Enter

4) Menu 2 – Numerical Move – Enter

   X2=100 Y2=50 Z2=10

5) Enter (or point) – Line passing – Enter

6) Menu 2 – Numerical move – Enter

   X3=200 Y3=250 Z3=10

7) Enter (or point) – Line passing – Enter

8) Menu 2 – Numerical move – Enter

   X4=0 Y4=250 Z4=10

9) Enter (or point) – Line end – Enter

10) Enter – End Program – Enter

11) Run

Program 11

This program makes the dispensing robot move by drawing a free style shape.

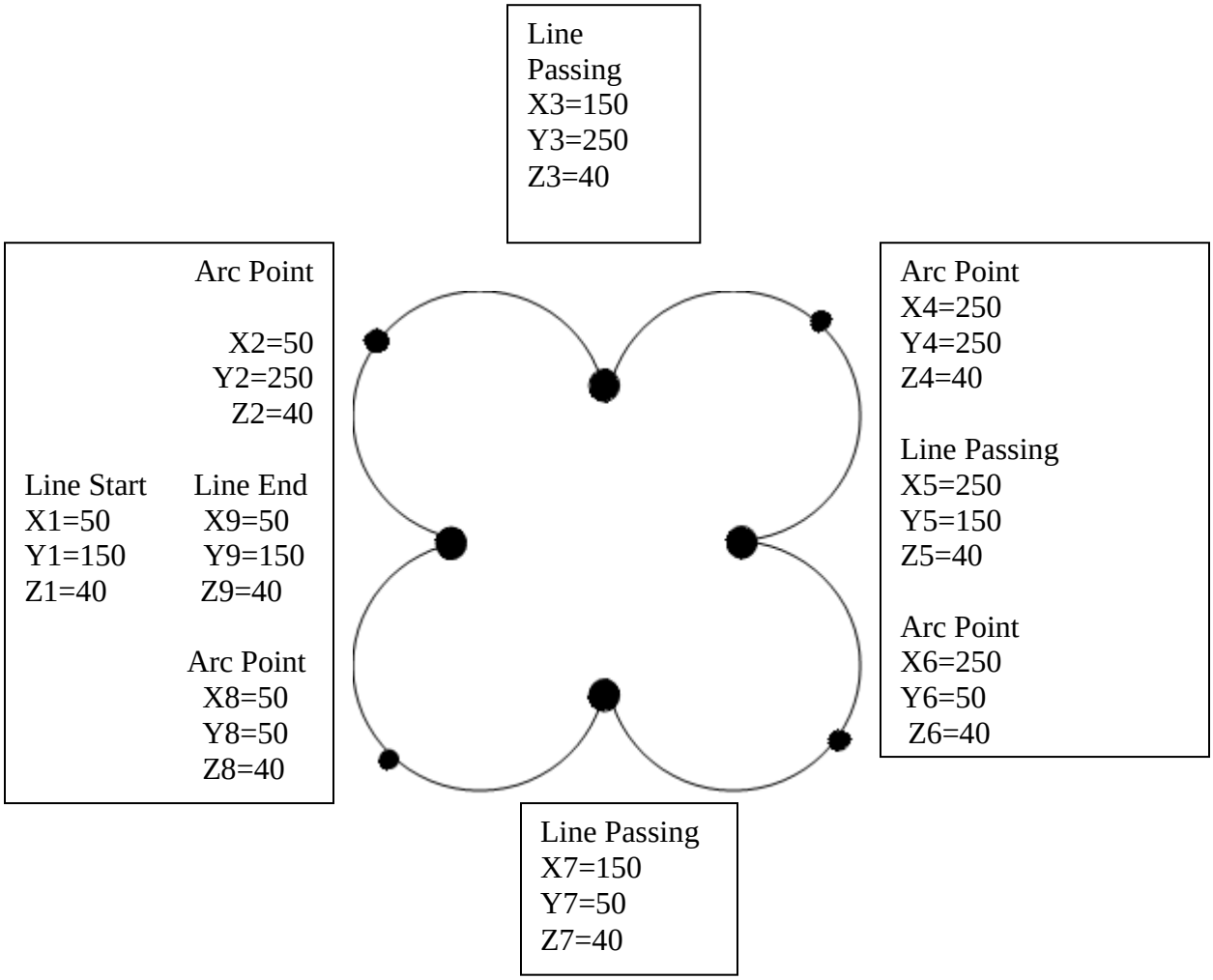

Figure B-9 Steps of program 11

Steps of the program:

1) Set up – Line Speed – Enter – 25 – Enter

   Set up – XY Move Speed – Enter – 20 - Enter

2) Menu 2 – Numerical move – Enter

X1=50 Y1=150 Z1=40

3) Enter (or point) – Line start – Enter
4) Menu 2 – Numerical move – Enter

X2=50 Y2=250 Z2=40

5) Enter (or point) – Arc Point – Enter
6) Menu 2 – Numerical move – Enter

X3=150 Y3=250 Z3=40

7) Enter (or Point) – Line Passing – Enter
8) Menu 2 – Numerical move – Enter

X4=250 Y4=250 Z4=40

9) Enter (or Point) – Arc Point – Enter
10) Menu 2 – Numerical move – Enter

X5=250 Y5=150 Z5=40

11) Enter (or Point) – Line Passing – Enter
12) Menu 2 – Numerical move – Enter

X6=250 Y6=50 Z6=40

13) Enter (or Point) – Arc Point – Enter
14) Menu 2 – Numerical move – Enter

X7=150 Y7=50 Z7=40

15) Enter (or Point) – Line Passing – Enter
16) Menu 2 – Numerical move – Enter

X8=50 Y8=50 Z8=40

17) Enter (or Point) – Arc Point – Enter

18) Menu 2 – Numerical move – Enter

    X9=50 Y9=150 Z9=40

19) Enter (or Point) – Line End - Enter

20) Enter (or point) – End Program – Enter

21) Run

Program 12

This program makes the dispensing robot move by drawing a free style shape.

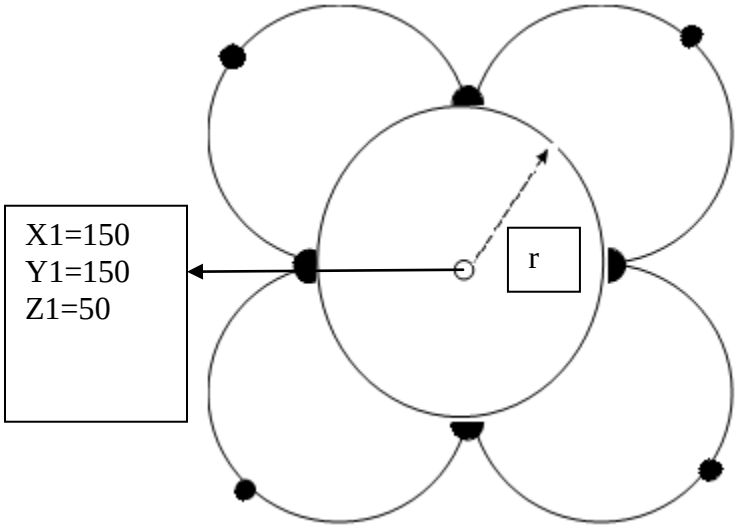

Figure B-10 Steps of program 12

Steps of the program:

1) Set up – Line speed – Enter – 30 – Enter

   Set up – XY move speed – Enter – 50 – Enter

2) Menu 2 – Numerical move – Enter

   X1=150 Y1=150 Z1=50

3) Enter (or point) – Circle – Enter

   Diameter – 200 – Enter

   Over angle – 0 – Enter

   Z lift select – (2 No) – Enter

4) Enter (or point) – Call program – Enter – Program 5 – Enter

5) Enter (or point) – End Program – Enter

6) Run

Program 13

This program makes the dispensing robot move by drawing a free style shape and filling circular part of the shape.

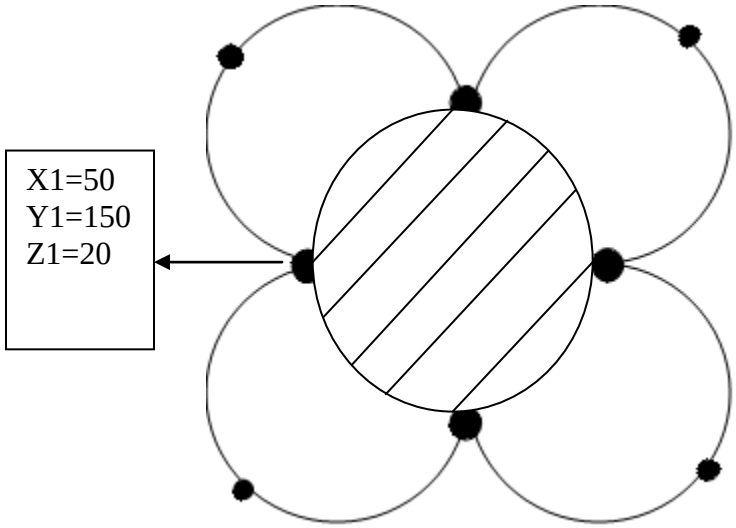

Figure B-11 Steps of program 13

Steps of the program:

1) Enter (or point) – Call program – Enter – Program 6 – Enter
2) Enter (or point) – Brush area – Enter – Select (2 - Circle) – Enter – Width – 5 – Enter
3) Menu 2 – Numerical move – Enter

   X1=50 Y1=150 Z1=20
4) Enter (or point) – Line start – Enter
5) Menu 2 – Numerical move – Enter

   X2=150 Y2=150 Z2=20
6) Enter (or point) – Line end – Enter
7) Enter (or point) – End Program – Enter

Program 14

This program makes the dispensing robot move by drawing a free style shape and filling a part of the circular part and a part of the rectangular part of the shape.

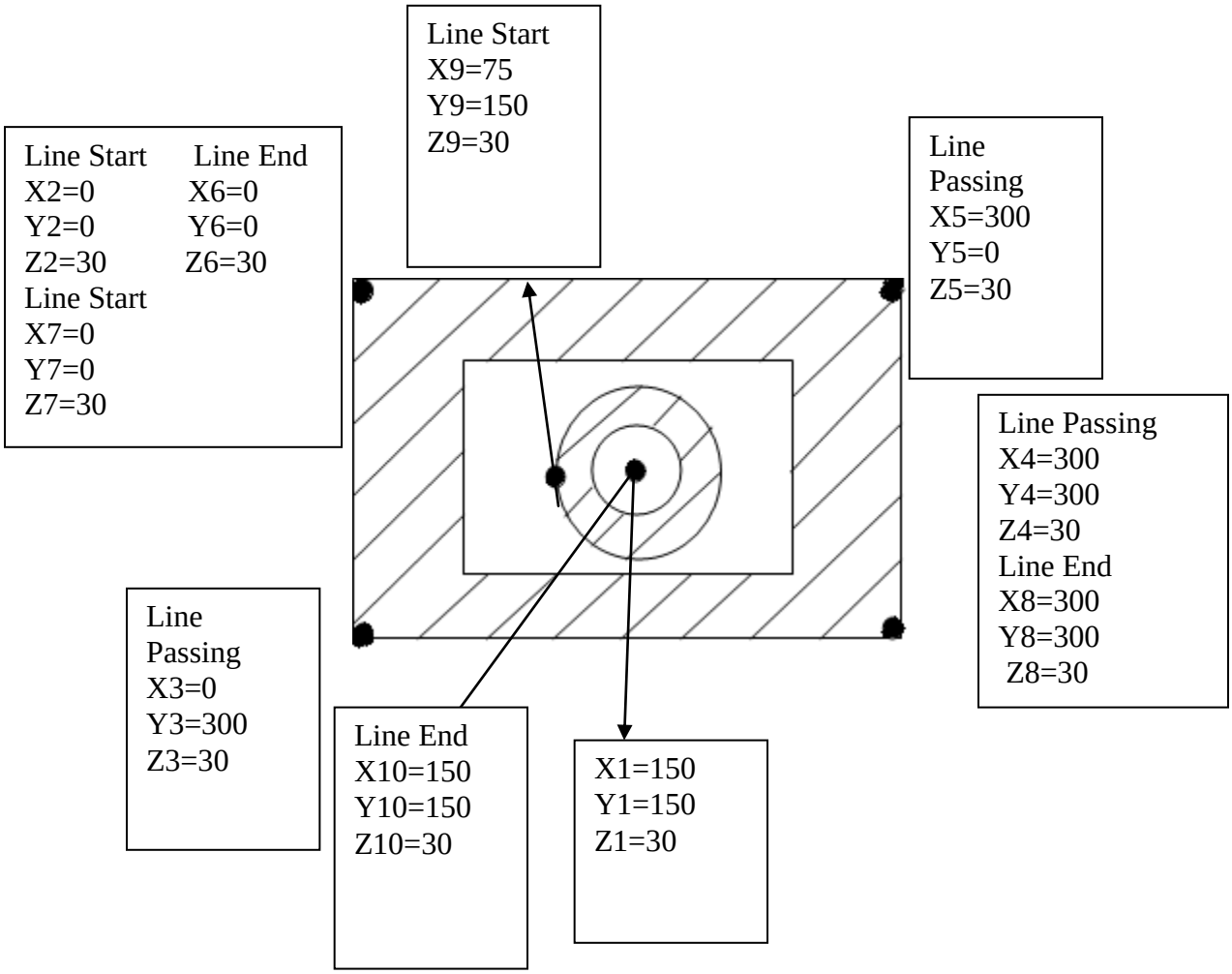

Figure B-12 Steps of program 14

Steps of the program:

1) Set up – Line Speed – Enter – 50 – Enter

   Set up – XY Move Speed – Enter – 10 - Enter

2) Menu 2 – Numerical move – Enter

X1=150 Y1=150 Z1=30

3) Enter (or point) – Circle – Enter

   Diameter – 150 – Enter

   Over Angle – 0 – Enter

   Z lift select – (2 - No) - Enter

4) Menu 2 – Numerical move – Enter

   X2=0 Y2=0 Z2=30

5) Enter (or point) – Line Start – Enter

6) Menu 2 – Numerical move – Enter

   X3=0 Y3=300 Z3=30

7) Enter (or Point) – Line Passing – Enter

8) Menu 2 – Numerical move – Enter

   X4=300 Y4=300 Z4=30

9) Enter (or Point) – Line Passing – Enter

10) Menu 2 – Numerical move – Enter

    X5=300 Y5=0 Z5=30

11) Enter (or Point) – Line Passing – Enter

12) Menu 2 – Numerical move – Enter

    X6=0 Y6=0 Z6=30

13) Enter (or Point) – Line End – Enter

14) Enter (or Point) – Brush Area – Enter – Select – (4 – Rect Band) – Enter – Width – 5-Enter – Band – 50 – Enter

15) Menu 2 – Numerical move – Enter

X7=0 Y7=0 Z7=30

16) Enter (or Point) – Line Start – Enter

17) Menu 2 – Numerical move – Enter

X8=300 Y8=300 Z8=30

18) Enter (or Point) – Line End – Enter

19) Enter (or Point) – Brush Area – Enter – Select – (5 – Circle Band) – Enter – Width – 5 – Enter – Band – 50 – Enter

20) Menu 2 – Numerical move – Enter

X9=75 Y9=150 Z9=30

21) Enter (or Point) – Line Start – Enter

22) Menu 2 – Numerical move – Enter

X10=150 Y10=150 Z10=30

23) Enter (or Point) – Line End – Enter

24) Enter (or point) – End Program – Enter

25) Run

Program 15

This program makes the dispensing robot move by drawing a free style shape and filling a part of the circular part and a part of the rectangular part of the shape.

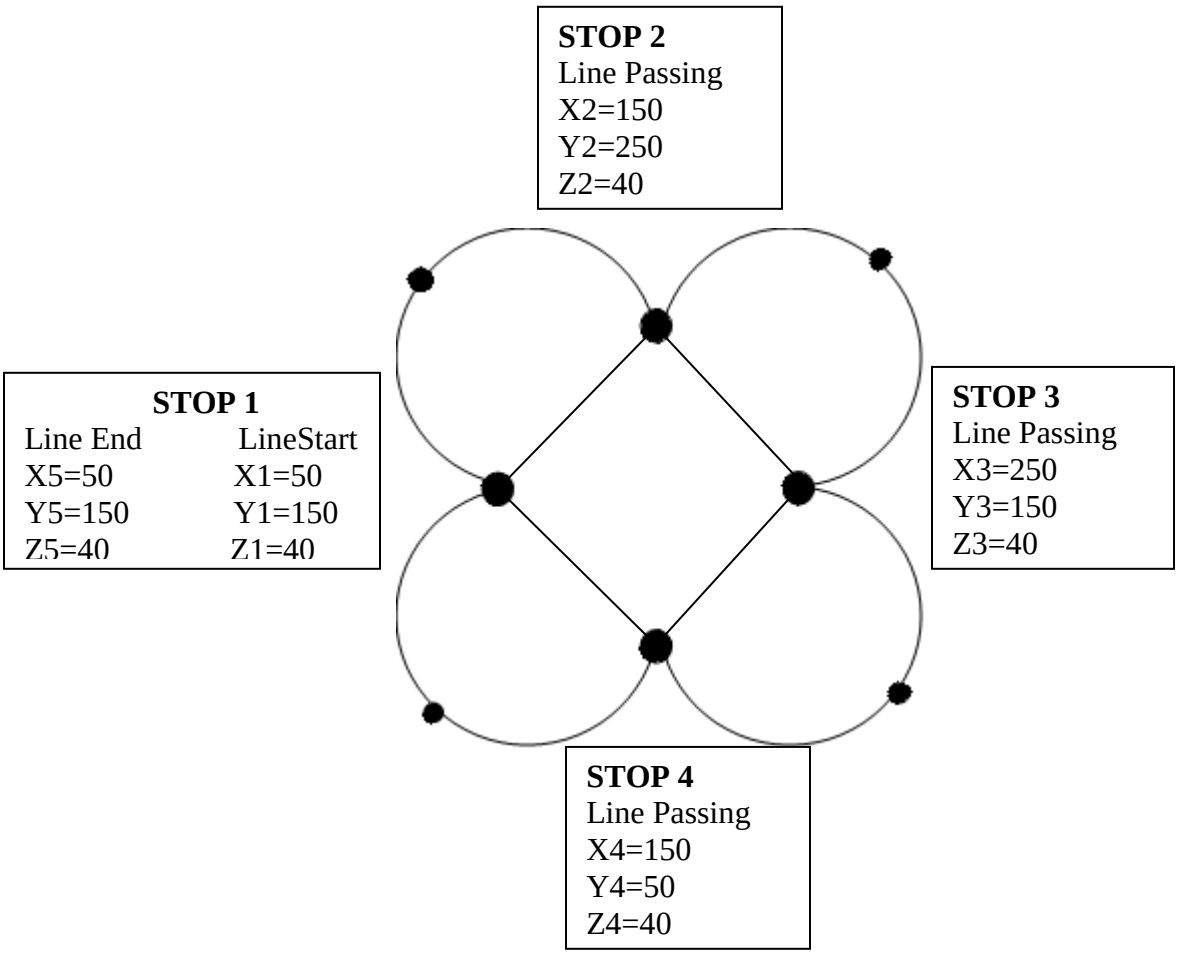

Figure B-13 Steps of program 15

Steps of the program:

1) Enter (or Point) – Call Program – Enter – Program 5 – Enter
2) Set up – Line Speed – Enter – 60 – Enter

   Set up – XY Move Speed – Enter – 40 - Enter

3) Menu 2 – Numerical move – Enter

   X1=50 Y1=150 Z1=40

4) Enter (or point) – Line start – Enter

5) Enter (or Point) – Wait Point – Enter – 30 sec – Enter

6) Menu 2 – Numerical move – Enter

   X2=150 Y2=250 Z2=40

7) Enter (or point) – Line Passing – Enter

8) Enter (or Point) – Wait Point – Enter – 30 sec – Enter

9) Menu 2 – Numerical move – Enter

   X3=250 Y3=150 Z3=40

10) Enter (or Point) – Line Passing – Enter

11) Enter (or Point) – Wait Point – Enter – 30 sec – Enter

12) Menu 2 – Numerical move – Enter

   X4=150 Y4=50 Z4=40

13) Enter (or Point) – Line Passing – Enter

14) Enter (or Point) – Wait Point – Enter – 30 sec – Enter

15) Menu 2 – Numerical move – Enter

   X5=50 Y5=150 Z5=40

16) Enter (or Point) – Line End – Enter

17) Enter (or point) – End Program – Enter

18) Run